

DOTTORATO DI RICERCA IN

Astrofisica

Ciclo XXXVII

Settore Concorsuale: 02/C1 – Astronomia, Astrofisica, Fisica della Terra e dei Pianeti Settore Scientifico Disciplinare: FIS/05 – Astronomia e Astrofisica

Observations of Fast Radio Bursts at low frequencies with the Northern Cross radio telescope

Presentata da: Davide Pelliciari

Coordinatore Dottorato

Prof. Dr. Andrea Miglio

Supervisore

Dr. Gianni Bernardi

Co-supervisore:

Dr. Maura Pilia

Esame finale anno 2025

Perché mi fisso a fare cose che non so, senza sapere neanche dove cominciare? Di certo riuscirò.

Luca, Marco Castello

Abstract

Fast Radio Bursts (FRBs) are short, energetic radio flashes, with typical durations between a few microseconds up to a few tens of milliseconds, during which they can release up to 10^{43} erg of energy. They are of cosmological origin, as was already hinted at by their large dispersion measures and later confirmed by host galaxy identifications. One of the outstanding open questions is related to the nature of the FRB progenitors, i.e. which sources they are associated with. The observation of FRB 20200428 from the Galactic magnetar SGR J1935+2154 provided strong support to the magnetar–FRB link, although which fraction of the FRB population can be linked to magnetars remains an open question.

The FRB population can be essentially classified into *one-off* (if they are observed only once) and *repeating* sources (if multiple events are observed from the same source). Although repeating FRBs are only $\sim 7\%$ of the known population, they offer a unique opportunity to study their energy distribution, their frequency and temporal properties, their environment/host galaxy and to search for counterparts at other wavelengths. Such observations are capable to shed light on the physics of the FRB mechanism and constrain the emission models.

Repeating FRBs also offer the chance to pinpoint their location with angular resolution of the order of a few tens of milliarcsecond (corresponding to pc scales for the nearby sources, up to kpc scales for the $z \sim 1$) ones. Such resolution allows one to associate the FRB to a specific environment (e.g., star forming region, nuclear region, star clusters) within its host galaxy and offers clues on the nature of the progenitor. Moreover, high resolution observations may characterise the origin of persistent radio sources, i.e. continuum sources that have been associated to a handful of repeating FRBs.

This thesis represents a contribution to each of the aforementioned topics:

- I present a search for FRBs in a sample of 7 nearby, star forming galaxies at 408 MHz with the Northern Cross telescope. Under the assumption that magnetars originating from the collapse of supernova cores are the FRB progenitors, we computed the FRB rate expected from the whole sample. Our lack of detections allowed us to place an upper limit on the event rate per magnetar λ_{mag} to be λ_{mag} < 0.25 magnetar⁻¹ yr ⁻¹ for bursts with energies larger than 10³⁴ erg, a factor of ~ 2 improvement on earlier constraints. This indicates that burst from magnetars like SGR J1935+2154 are rare and cannot alone account for the observed rate of extragalactic FRBs, providing further evidence for an additional population of progenitors;
- I characterise the burst rate and energy distribution of the very active repeating source FRB 20220912A, using observations at 408 MHz and 1.4 GHz. The source was monitored for 122 hours at 408 MHz and 177 hours at 1.4 GHz, over a time scale of one year and we found a prominent frequency-dependent burst rate, changing from $0.19 \pm 0.03 \text{ hr}^{-1}$ for bursts with fluences $\mathcal{F} \geq 17$ Jy ms at 408 MHz to less than 0.017 hr⁻¹ (at 95% confidence level) for bursts with fluences $\mathcal{F} \geq 20$ Jy ms at 1.4 GHz. Given the sixteen bursts detected at 408 MHz, it was possible to constrain the 0.408 1.4 GHz burst spectral index β to be $\beta < -2.3$, consistent with an intrinsic narrow-band burst nature. The burst rate at 1.4 GHz declines by about four orders of magnitude over one year and the spectral

index of the cumulative spectral energy distribution to be $\alpha_E = -1.3 \pm 0.2$: those two characteristics are similar to another hyperactive repeater, FRB 20201124A, indicating a possibly similar emission mechanism for both sources. This study represents a first step into the systematic characterization of a sample of active repeaters;

• I characterise the impact that calibration errors have on the accuracy of FRB localisation. In particular I used high angular resolution (~ 20 mas) observations of the repeating FRB 121102 taken with a subset of the EVN array. I investigate how the localisation accuracy of the associated persistent radio source changes if fewer antennas are included in the calibration. I also simulate the impact that phase calibration errors have on the localisation of the burst itself. In both cases, I found that localisation errors are smaller than a few milli-arcseconds, of the same orer of magnitude of the error budget already reported in published observations. The magnitude of these systematic errors is sufficiently small not to impact the association of the FRB with its local environment, e.g. globular clusters or star forming regions.

Contents

1	The	tast radio burst phenomenon			
	1.1	A brief historical background			
	1.2	Properties and derived constraints			
		1.2.1 Dispersion			
		1.2.2 Burst duration			
		1.2.3 Flux density, fluence and energetics			
		1.2.4 Spectral properties			
	1.3	One off vs. Repeaters			
		1.3.1 Hyperactive repeaters			
		1.3.2 Periodic FRBs and quasi-periodicities			
	1.4	Host galaxies and precise localisations			
		1.4.1 Persistent radio sources associated with FRBs			
	1.5	FRB progenitors and emission models			
	1.6	FRBs as an independent cosmological probe			
		1.6.1 Constraints on cosmological parameters			
		1.6.2 Other relevant constraints			
2	Observing FRBs with the Northern Cross radio telescope 31				
	2.1	The Northern Cross			
		2.1.1 The NC-FRB project			
	2.2	FRB observations			
		2.2.1 Data acquisition			
		2.2.2 Calibrations			
		2.2.3 Scheduling observations			
		2.2.4 Data reduction and FRB searching			
	2.3	Conclusions			
3	\mathbf{FR}	B-magnetar connection in a sample of nearby galaxies 43			
	3.1	Abstract			
	3.2	Introduction			
	3.3	An FRB search in a sample of nearby galaxies			
		3.3.1 Sample description and observations			
		3.3.2 FRB detection from the direction of M101			
	3.4	Upper limits on the FRB repetition rate from our observations			
		3.4.1 SGR1935-like magnetars			
		3.4.2 Ultra-luminous X-ray sources			
	3.5	Discussion and conclusions			

4	Mu	Itiwavelength study of the actively repeating FRB 20220912A	55	
	4.1	Abstract	55	
	4.2	Introduction	56	
	4.3	Observations	57	
		4.3.1 Northern Cross radio telescope	57	
		4.3.2 Medicina "Grueff" radio telescope	57	
		4.3.3 uGMRT	58	
		4.3.4 Swift and AGILE monitoring	60	
	4.4	Results and discussion	60	
		4.4.1 Constraints on broad-band spectral index	63	
		4.4.2 Continuum radio emission from FRB 20220912A host galaxy	65	
		4.4.3 Results from the high energy monitoring of FRB 20220912A	67	
	4.5	Summary and conclusions	68	
	App	bendix A. Multi-wavelength follow up of new CHIME repeaters	69	
5	The impact of calibration errors on the FRB localisation using VLBI observa-			
	tion		73	
	5.1	Introduction	73	
	5.2	Elements of interferometry and VLBI	74	
		5.2.1 The European VLBI Network	77	
	5.3	Very long baseline observations of the R1 FRB	78	
	5.4	Impact of calibration errors on VLBI localisations	80	
		5.4.1 The FRB case	81	
	5.5	Conclusions	82	
	App	endix A. joanne: a pipeline for transient simulation into VLBI visibilities	83	
6	Conclusions			
J	6.1	Future prospects	87 89	
7		cnowledgements	91	
	7.1	Ringraziamenti	93	

Chapter 1

The fast radio burst phenomenon

Astrophysical transients, i.e. events that appear and disappear on human observable timescales, represent a fascinating aspect of the cosmic realm, unveiling fleeting yet powerful phenomena that punctuate the otherwise steady nature of the Universe. Of the known transients populating the sky, short-duration transients (also known as fast transients), with temporal duration ≤ 1 s, represent a new and prolific field in astrophysics, since their properties are usually related to the most extreme phenomena existing in the Universe. Within short-duration transients, fast radio bursts (FRBs, hereafter), with their ms duration and Jy-level flux densities, are the shortest and brightest radio pulses ever detected. Notable is their extragalactic and even cosmological origin, which makes them a novel probe to study the large-scale properties of our Universe such as, e.g., its matter-content and the cosmological magnetic field permeating it. Various aspects of FRBs are still under investigation, including their engine, radiation mechanism, distribution, classification, and propagation effects, as these are key to understanding their origins (see, e.g., Cordes & Chatterjee, 2019; Petroff et al., 2019, 2022; Pilia, 2021; Zhang et al., 2023a, for reviews on the topic).

This chapter serves as an introduction to the phenomenon of FRBs. The first section provides a brief historical review of radio transients, starting with the discovery of radio pulsars and setting the stage for understanding the emergence of FRBs. The second section delineates the key properties of FRBs, highlighting their enigmatic observed characteristics. In the third Section, we briefly overview the primary models proposed to explain the origin of FRBs. Finally, in the last Section we describe the importance of FRBs in probing the large-scale properties of our Universe.

1.1 A brief historical background

In 1967 Jocelyn Bell, a PhD student at the University of Cambridge, was analysing radio observations taken with an array consisting of 500 dipoles. The outcome of these observations revealed the presence of a periodic radio signal that resembled a radio frequency interference (RFI), which "however" was appearing only when the telescope was observing a specific part of the sky (Hewish et al., 1968). It did not take long to realize that this particular type of signal could be linked to an extreme type of star, i.e. a neutron star (NS), which was predicted to emit pulsed radio emission observable (Gold, 1968). Since the discovery of the first pulsar, the number of currently known pulsars has grown to ~ 3500 , according to the Australian Telescope National Facility (ATNF) catalogue (Manchester et al., 2005). The radio pulses emitted by pulsars are dispersed as they travel through the ionized interstellar medium (ISM). This delay is characterized by a dispersion measure (DM),

$$DM = \int_0^d n_e dl , \qquad (1.1)$$

with d being the pulsar distance and n_e the number density of free electrons along the line of sight (LOS) to the pulsar (see Section 1.2.1 for a detailed description of this phenomenon). The DMs of pulsars increase at low galactic latitudes, given the higher ISM density in the Galactic plane, while they are smaller ($\sim 10 \text{ pc cm}^{-3}$) (see, e.g. Cordes & Chatterjee, 2019) for high galactic latitudes, highlighting a nearby, galactic origin of known pulsars. Nowadays, pulsars are used to construct models of the ISM electron density (Cordes & Lazio, 2002; Yao et al., 2017).

The emission from pulsars covers a wide range of periods, going from few milliseconds to tens of seconds. However, PSR B0531+21 (aka the Crab pulsar), identified as the core of the supernova remnant resulted from SN 1054 (Staelin & Reifenstein, 1968), has been discovered not for its pulsed emission, but rather for its anomalously intense pulses, known as qiant radio pulses (GRPs) (see, e.g. Johnston & Romani, 2004, for a review on GRPs), which can reach flux densities hundreds or even thousands of times the mean flux density of regular, periodic pulses. In the early 70's, Ginzburg (1973) suggested that one could use energetic flares from distant sources as a probe for the intergalactic gas density. In the same years, Rees (1977) proposed that annihilating black holes (BHs) of small mass could end in an energetic radio burst observable from remote distances. Following these hypotheses, Huguenin & Moore (1974) and Phinney & Taylor (1979) conducted early transient searches for single pulses having duration as short as 16 ms. These were unsuccessful, but placed the first upper limits on the rate of both primordial BH explosions and bright bursts from distant galaxies. Interestingly, Linscott & Erkes (1980) reported the detection of multiple, highly-dispersed radio bursts from the giant elliptical M87 galaxy. These bursts, however, were not found by other observers and in follow-up observations (McCulloch et al., 1981; Taylor et al., 1981; Suresh et al., 2021).

Several years later, Cordes & McLaughlin (2003) implemented a new algorithm optimized for single pulse search, and used it to carry out a systematic search for fast radio transients. Although the latter gave no detection, a follow-up search allowed them to discover 11 new sources, called rotating radio transients (RRATs; McLaughlin et al., 2006), that were not found initially during periodicity searches. These sources emitted single radio pulses, similar to those from pulsars, but with strong amplitude variations over long timescales. Further monitoring revealed underlying periods of 1-7 s, consistent with the rotation periods of NSs, hence the term "rotating" in RRATs. This new discovery implied that a large population of bright single pulses might be hiding in existing radio survey data (Keane et al., 2011).

During a single-pulse analysis of archival radio data taken with the Parkes 64-m single dish in 2001, David Narkevic, Duncan Lorimer and Maura McLaughlin found an exceptionally bright single burst having a flux density of ~ 30 Jy (see Figure 1.1), which came from $\sim 3^{\circ}$ south of the Small Magellanic Cloud (SMC) (Lorimer et al., 2007). The burst, later cataloged as FRB 20010724A¹, is widely referred to in the literature as the *Lorimer burst*. FRB 20010724A had DM = 375 pc cm⁻³, which is ~ 8 times higher than the expected DM contribution from our Galaxy, implying a maximum distance of ~ 1 Gpc. After this discovery, seven years passed before the detection of four other highly dispersed bursts (Thornton et al., 2013), that provided evidence for a cosmological population of extragalactic sources capable of emitting bright, detectable bursts, having an all-sky rate of 10^4 sky⁻¹ day⁻¹, which they termed as "Fast Radio Bursts" (Thornton et al., 2013).

The first FRBs were discovered with the Parkes radio telescope in Australia, and it took approximately 7 years, since the Lorimer burst discovery, before another telescope observed

¹In this Thesis, we'll use the Transient Name Server (TNS) convention to label FRB sources as FRB YYYYMMDDxxx. Here, YYYY, MM and DD stand for the year, month, and day of source discovery, while xxx are letters from A to Z to differentiate FRB events on the same day

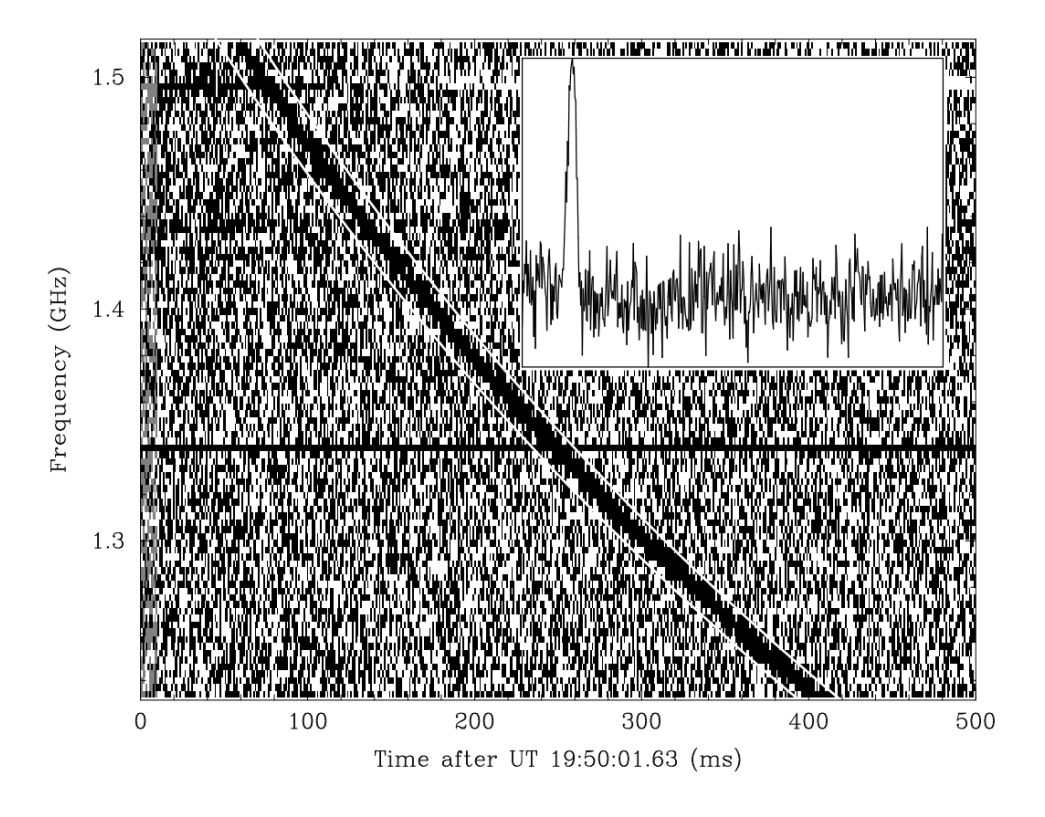


Figure 1.1: Time-frequency plot (also known as dynamical spectrum or waterfall plot) of FRB 20010724A, the first FRB ever discovered. The burst clearly sweeps across frequency, as expected from the propagation of the radio waves in a plasma (see Section 1.2.1 for details). The horizontal black line is a persistent RFI at frequency ~ 1.34 GHz. The inset plot represents the frequency averaged time series corrected by the delay due to the dispersion effect (considering DM = 375 pc cm⁻³). Credits to Lorimer et al. (2007).

an FRB. Initially, the fact that FRBs were detected only in Parkes observations increased the scepticism around the true astrophysical nature of these sources. Indeed, searches through the Parkes archival data in 2011 revealed a peculiar class of artificial signals, with \sim ms duration, which showed the characteristic sweep in radio frequency channels of a genuine astrophysical signal. Those were dubbed as 'perytons'. Further investigations of the Peryton phenomenon with a larger population of events and upgraded RFI monitoring at the Parkes telescope subsequently pinpointed their source to microwave ovens being used at site (Petroff et al., 2015).

The first FRB discovered with a telescope other than Parkes came in 2014 (Spitler et al., 2014), from the Arecibo 305-m single-dish, which also happened to be the first repeating FRB source ever discovered (Spitler et al., 2016). Indeed, until then, FRBs were all one-off events, i.e. that happened just once in hours of monitoring towards the same sky direction. In this case, instead, Arecibo detected multiple bursts from the same diretion of the sky having consistent DM with each other, suggesting a common origin. The discovery of the repeating nature opened new observational opportunities, e.g. multi-wavelength follow ups. Still, nowadays their physical mechanism, as well as their progenitors are still a matter of debate. Regarding their origin, tens of models were proposed (see, e.g. Platts et al., 2019, for a review of FRB models) but the fact that some of them show repetitions ruled out catastrophic models where progenitors do not survive the burst event. Currently, it is not clear whether one-off events represent a distinct population of sources than repeating sources, but surely, for the latter, catastrophic models can be ruled out.

1.2 Properties and derived constraints

Some important physical inferences can be made by looking at the principal observational FRB parameters, such as their temporal duration, DM, flux density and polarisation state. All these properties are closely related both to the FRB physical properties and to the propagation effects in the intervening material between the FRB source and the observer. This material can be ionized, magnetized, and clumpy on a range of different scales and radio waves can be diffracted, refracted, absorbed and undergo Faraday rotation. Such propagation effects play an important role in our understanding of FRBs.

1.2.1 Dispersion

The ISM of the Milkw Way (MW) has a mean volumetric electron density of $n_e \sim 0.03$ cm⁻³, while the intergalactic medium (IGM) has $\sim 10^{-6}$ cm⁻³ particles. The interaction of radio waves with ionised particles, i.e. electrons and protons, results in a different propagation velocity for the different wavelengths. In particular, longer wavelengths propagate with lower velocity with respect to shorter ones. This phenomenon is known as the *dispersion* of the radio waves.

An electromagnetic wave (EM) can be described by oscillations in space and time of the electric and magnetic fields. Considering for simplicity only electric field \vec{E} oscillations, the latter can be described at each coordinates (\vec{x},t) by:

$$\vec{E}(\vec{x},t) = \vec{E}_0 e^{i(\vec{k}\cdot\vec{r}-\omega t)} , \qquad (1.2)$$

where $\vec{k} = 2\pi/\lambda$ is the wavenumber vector, directed along the propagation axis and ω is the angular frequency. In the former, \vec{k} is related to space oscillations, while ω to time oscillations.

The dispersion relation $\omega = \omega(k)$ of EMs traveling through a non-magnetized, globally neutral plasma can be readily obtained by incorporating spatial and temporal variations of all

quantities in the form of $\exp i(\vec{k} \cdot \vec{r} - \omega t)$ into Maxwell's equations and Newton's second law equation. One finds (Rybicki & Lightman, 1979):

$$ck = n_r \omega, \tag{1.3}$$

where c = 299.792.458 m/s is the speed of light in vacuum, and

$$n_r = \left(1 - \frac{\omega_p^2}{\omega^2}\right)^{1/2} \tag{1.4}$$

is the refraction index, which in turns depends on the plasma frequency ω_p , defined as (Draine, 2011)

$$\omega_p = \left(\frac{4\pi n_e e^2}{m_e}\right)^{1/2} \simeq (5.63 \times 10^4 \text{ Hz}) n_e^{1/2} .$$
 (1.5)

Here n_e is the electron density of the plasma while $m_e \simeq 9.11 \times 10^{-31}$ kg and $e \simeq 1.6 \times 10^{-19}$ C are the mass and the electric charge of the electron, respectively.

From the dispersion relation (1.3) we can get the group velocity of the wave packet:

$$v_{\rm g}(\omega) = c \left(1 - \frac{\omega_p^2}{\omega^2}\right)^{1/2} . \tag{1.6}$$

Here one can cleary see that for $\omega > \omega_p$ the wave packet can propagate and that the group velocity depends on the frequency $\nu = \omega/2\pi$ of the wave. Considering then $\omega \gg \omega_p$, which is a realistic assumption for astrophysical observations, we obtain a frequency-dependent arrival times of the radio waves that travel a distance D from the observer:

$$t(\nu) = \int_0^D \frac{\mathrm{d}l}{v_{\mathrm{g}}(\nu)} \simeq \int_0^D \frac{\mathrm{d}l}{c} \left(1 + \frac{\omega_p^2}{2\omega} \right). \tag{1.7}$$

In this way, the difference in arrival time between two frequencies ν_2 and ν_1 with $\nu_2 > \nu_1$ is:

$$\Delta t = t(\nu_2) - t(\nu_1) = \frac{e^2}{2\pi m_e c} \left(\frac{1}{\nu_2^2} - \frac{1}{\nu_1^2}\right) \int_0^D n_e \, dl$$

$$= \mathcal{D} \times DM \left(\frac{1}{\nu_2^2} - \frac{1}{\nu_1^2}\right),$$
(1.8)

where $\mathcal{D} \equiv \frac{e^2}{2\pi m_e c} \simeq 4.15 \times 10^3 \text{ MHz}^2 \text{ pc}^{-1} \text{ cm}^3 \text{ s is known as the dispersion constant, and the dispersion measure (DM) is defined as in equation 1.1, and it is usually expressed in pc cm⁻³. As one can see from this relation, the observed DM encodes the content of free electrons along the line of sight. Considering <math>\nu_1$ and ν_2 both in MHz, then the arrival time delay of equation (1.8) becomes:

$$\Delta t \simeq 4.15 \times 10^6 \text{ ms} \times \text{DM} \left(\frac{1}{\nu_2^2} - \frac{1}{\nu_1^2} \right).$$
 (1.9)

Here it is evident the ν^{-2} dependence of the burst arrival times that one can see also for the Lorimer burst in Figure 1.1 and for FRB 20110220 in Figure 1.2.

DM measurements can be used to estimate the distance D to the source by numerically integrating Equation (1.1), assuming a model for the Galactic electron density distribution, n_e . Over the years, these models have been derived from independent measurements of pulsar distances², paired with their DM estimates. In particular, the prevailing ones are the NE2001

²Indeed, all the known pulsars are located in the MW or in the Small and Large Magellanic Clouds (Manchester et al., 2005).

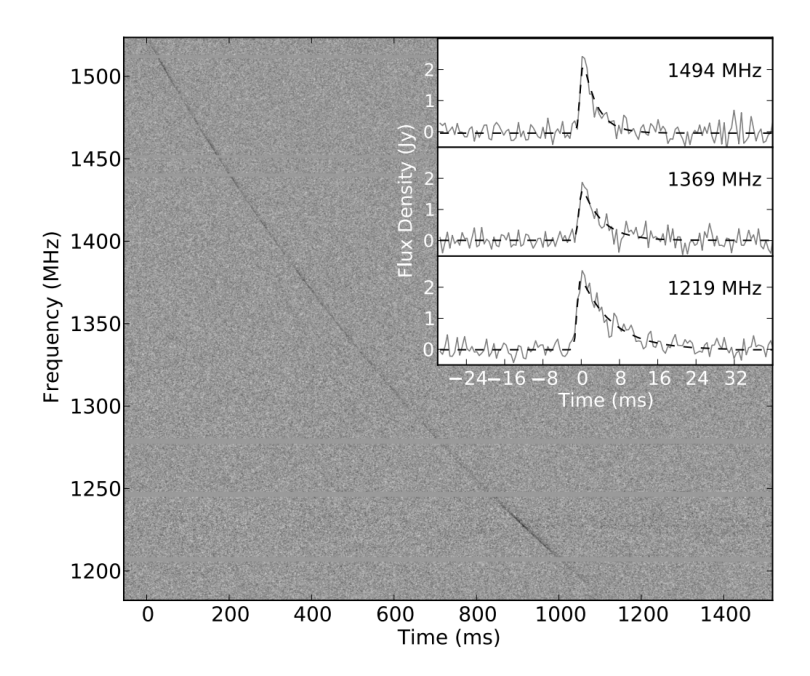


Figure 1.2: Dynamical plot of a burst from FRB 20110220. In the principal panel it is evident the ν^{-2} delay between the burst arrival times at different frequencies, while the inset shows the temporal broadening of the burst at lower frequencies caused by the scattering phenomenon. Credits to Thornton et al. (2013).

(Cordes & Lazio, 2002, 2003) and the YMW16 (Yao et al., 2017) models. Although the latter resulted in improved pulsar distance estimates (Yao et al., 2017) and benefits from more recent data, the former is still widely used. The prediction for n_e by the YM16 model is plotted in Figure 1.3 in galactocentric coordinates. NE2001 and YMW16 model only the DM contribution from ISM electrons, but do not consider other contributions, such as the MW halo component. The latter usually is estimated from hydrodynamical simulations (Dolag et al., 2015), considering spherical models for the distribution of baryonic gas in the MW halo, or using DM estimates of high-latitude pulsars and FRBs (see Price et al., 2021, for a review on the different methods). Usually, a conservative value of 50 pc cm⁻³ is used for the halo contribution, which is consistent with the majority of literature works that try to estimate it.

The high values of DM recorded for the first FRBs suggested that these sources are coming from large distances, way beyond our Galaxy. Following this hypothesis, which turned out to be true (see Section 1.4), the measured DM of an FRB can be expressed as the sum of different contributions (e.g. Deng & Zhang, 2014):

$$DM_{obs} = DM_{MW,ISM} + DM_{MW,halo} + DM_{IGM}(z) + \frac{DM_{host}}{1+z}, \qquad (1.10)$$

where $DM_{MW,ISM}$ is the DM contribution from MW ISM electrons, $DM_{MW,halo}$ is the MW halo contribution, $DM_{IGM}(z)$ is the IGM contribution along the line-of-sight for a source placed at redshift z and DM_{host} is the contribution from the FRB host galaxy and local environment around the FRB source. The $(1+z)^{-1}$ factor in the last term takes into account the Hubble expansion of the Universe. Interestingly, the third term has a dependence on the assummed cosmology (e.g. Macquart et al., 2020a), and can be used to constrain cosmological parameters and to investigate Universe properties on large scales (see Section 1.6, for further details).

One can estimate an upper limit for the likely redshift z of the FRB source by making assumptions on the different DM contributions. To this purpose, a general rule of thumb is $z < \frac{\rm DM_{IGM}}{1000}$ pc cm⁻³ (e.g. Ioka, 2003; Inoue, 2004). Considering the case of the Lorimer burst, its measured DM is 375 pc cm⁻³, which is ~ 350 pc cm⁻³ in excess with respect to $\rm DM_{MW,ISM} \simeq 25$

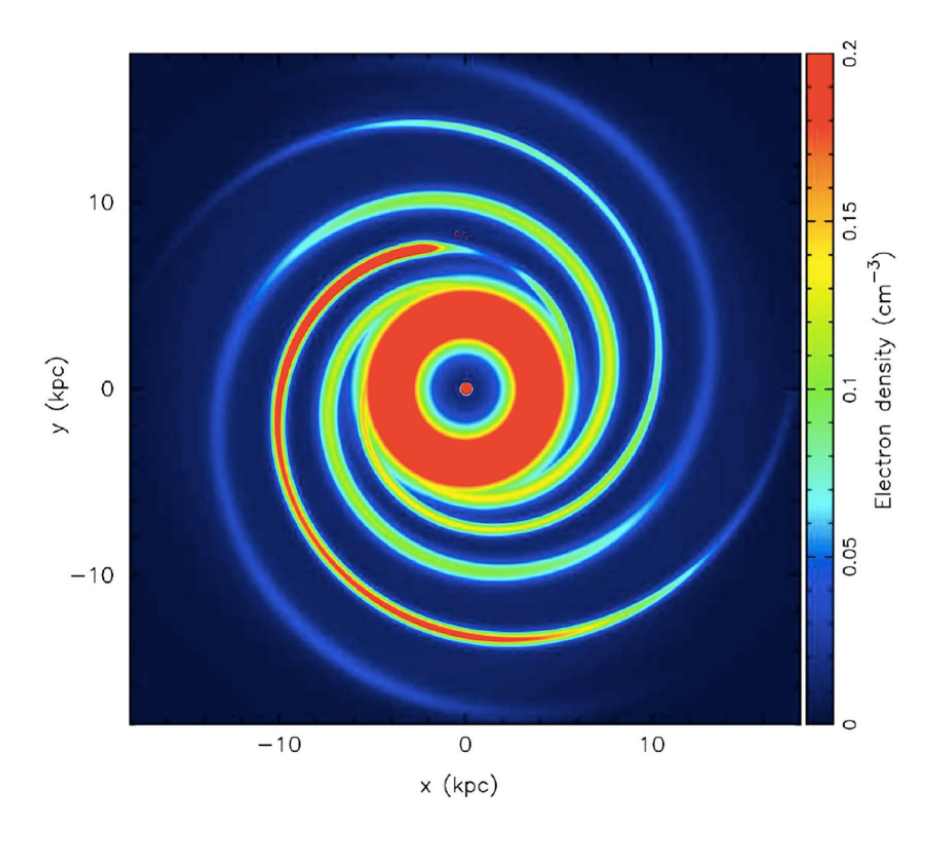


Figure 1.3: Electron density distribution in the Galactic plane from the YMW16 model (Yao et al., 2017). The Galactic Center is at x = 0, y = 0. Credits to Yao et al. (2017).

pc cm⁻³ towards its direction in the sky, as estimated from electron density models. Assuming a conservative DM halo contribution of ~ 100 pc cm⁻³ (Prochaska et al., 2019), and a total of ~ 200 pc cm⁻³ from the Lorimer burst host galaxy, one obtains DM_{IGM} ~ 50 pc cm⁻³, which translates into z < 0.05. This resdhift finally converts into an upper bound for the luminosity distance of the source of $d_L < 220$ Mpc, when considering a flat Λ Cold Dark Matter (Λ CDM) cosmological model. The same upper limit changes to z < 0.25, i.e. $d_L < 1$ Gpc, if the host DM contribution is instead considered negligible, strengthening the hypothesis of a cosmological origin for the source that has emitted the Lorimer burst. Nowadays, the extragalactic nature of FRBs has been confirmed by their precise localisation in host galaxies (see Section 1.4), with the furthest (up to now) having redshift $z \simeq 1$ (Ryder et al., 2023).

1.2.2 Burst duration

The intervening media in which an FRB signal travels can exhibit anisotropies and irregularities, inducing additional propagation effects other than dispersion. In particular, a turbulent medium results in the multi-path propagation of the signal, with certain parts of the latter arriving later due to longer path lengths. In general, the result is a non gaussian burst profile which can be described instead by a convolution of a gaussian function with a one-sided exponential tail of the form $\exp(-t/\tau_s)$, where τ_s represents the scattering time and determines the extent to which the FRB signal experiences broadening through exponential decay. This model is known as the thin-screen model (Scheuer, 1968). Following this model, irregularities in the medium follow a Kolmogorov spectrum and are confined to a thin layer between the source and the observer. In such a model, the scattering time is expected to depend strongly on the observing frequency, in particular as (Bhat et al., 2004):

$$\tau_s \propto \nu^{-4} \ . \tag{1.11}$$

Such behaviour has been observed for many FRBs (e.g. Thornton et al., 2013; Qiu et al., 2020), and an example of the frequency dependence of τ_s can be seen in the inset of Figure 1.2.

Moreover, the same in-homogeneities responsible for scattering can also cause intensity fluctuations of the FRB signal, a phenomenon called *scintillation*. Scintillation arises due to refractive and diffractive effects as the signal traverses turbulent material with varying electron densities across different length scales. These variations induce delays in the signal, leading to either amplification or attenuation upon the wave recombination, depending on interference effects. This results in a complex frequency structure that evolves over time from the observer's perspective. The characteristic scintillation bandwidth ($\Delta\nu_{\rm scint}$) over which an intensity modulation is observed scales strongly with the frequency as $\Delta\nu_{\rm scint} \propto \nu^4$ (Cordes & Lazio, 2002; Spitler et al., 2018).

Overall, the observed burst width W_{obs} of an FRB is the sum of different broadening contributions. In particular we can write (e.g. Amiri et al., 2017):

$$W_{\rm obs} = \sqrt{W_{\rm int}^2 + t_{\rm samp}^2 + \Delta t_{\rm DM}^2 + \Delta t_{\rm DM_{err}}^2 + \tau_s^2} , \qquad (1.12)$$

where W_{int} is the intrinsic burst width, t_{samp} is the sampling time at which the data have been temporally binned,

$$\Delta t_{\rm DM} = (8.3 \ \mu \text{s}) \ \text{DM} \ \Delta \nu_{\rm MHz} \nu_{\rm GHz}^{-3} \tag{1.13}$$

is the frequency-dependent smearing delay due to dispersion across a single frequency channel, $\Delta t_{\rm DM_{err}}$ is the pulse broadening due to a de-dispersion at a slightly wrong DM and τ_s is the scattering time. From an estimate of the intrinsic burst duration W_i , one can set an upper limit, via causality arguments, to the length scale R_0 related to the FRB central engine:

$$R_0 \le cW_i (1.14)$$

which gives $R_0 \leq 300$ km for $W_i = 1$ ms. This upper limit suggests compact, stellar-mass objects such as a NS or a BH as likely progenitors for FRBs (see Section 1.5 for details on progenitor models). Nowadays, we know that FRBs can have durations as short as a micro-second (e.g. Snelders et al., 2023). This value further pushes down the size limit for the FRB emitting region to some kilometers, suggesting an emission close to the surface of the celestial object. Finally, it is possible to show that even in the case in which the central engine is moving towards the observer with a relativistic speed, the upper limit of equation (1.14) it is still valid to constrain its size (Zhang, 2022).

1.2.3 Flux density, fluence and energetics

When an FRB is detected by a radio telescope, what is actually measured is the amplitude of its raw signal, which can then be converted into units of Jansky (Jy) (1 Jy = 10^{-26} W m⁻² Hz⁻¹) by calibrating the instrument response to an extragalactic source with known flux density. To convert the voltage amplitudes measured by a radio telescope into physical units, the radiometer equation is commonly employed, the latter used to estimate the root-mean-square (rms) σ of the de-dispersed time series, computed on a timescale W and bandwidth B (Lorimer & Kramer, 2004):

$$\sigma \simeq \frac{T_{\rm sys}}{G\sqrt{N_p BW}} \ . \tag{1.15}$$

Here T_{sys} is the system temperature, representing the noise of the system, in which many contributions enter such as, e.g. the noise contribution from the sky in the direction of the source, from atmospheric emission and from the receiver noise. In equation (1.15) G represents the antenna gain and N_p is the number of recorded polarisations. To charachterise the radio

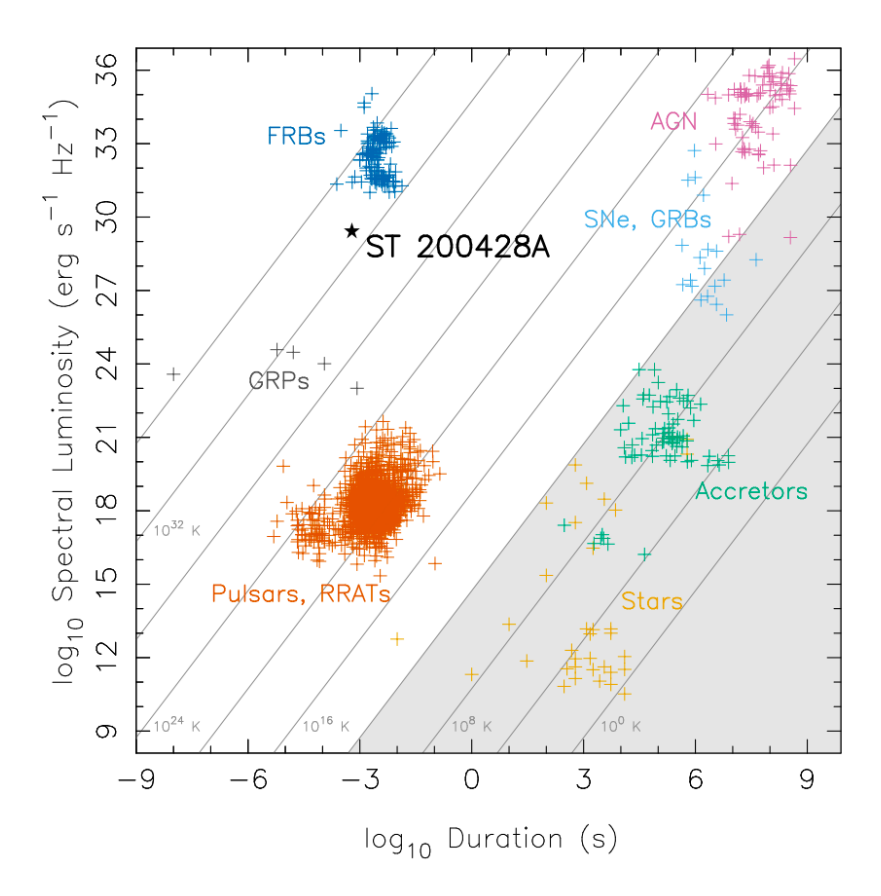


Figure 1.4: Spectral luminosities as a function of the burst duration for the zoo of astrophysical transients. In particular, one can find a subset of localised FRBs (i.e. for which the redshift is known), GRPs and single pulses from pulsars, RRATs, active galactic nuclei (AGN), supernovae (SNe), gamma ray bursts (GRBs), accreting binary systems ("accretors" in the Figure) and transient phenomena of stars. The star symbol refers to FRB 20200428, i.e. the FRB-like signal coincident with an X-ray outburst from a known Galactic magnetar detected from STARE-2, in this case. Diagonal lines represent constant brightness temperatures at a reference frequency of 1.4 GHz. The shaded region includes sources with brightness temperatures below 10¹² K, which are likely incoherent emitters not subject to relativistic boosting. Credits to Bochenek et al. (2020).

telescope sensitivity one usually defines the so-called system equivalent flux density (SEFD) as SEFD = $T_{\rm sys}/G$. Having an estimate for the telescope rms noise at timescales of milliseconds one can recover the peak flux density of the burst, $S_{\rm peak}$, detected at a given S/N as $S = S/N \times \sigma$. The integral of the flux density S(t) over the burst profile:

$$\mathcal{F} = \int_{\text{on burst}} S(t) \, dt \,, \tag{1.16}$$

is known as the fluence \mathcal{F} of the burst. It is expressed in units of Jy s, but typically one prefers Jy ms, as FRBs have durations on millisecond timescales. Known FRBs have shown fluences ranging from tens of mJy ms to kJy ms, spanning more than 6 orders of magnitude.

Knowing the distance, or equivalently the redshift, of the FRB source that emitted a given burst, one can get an estimate of its energetics. Indeed, the flux density of the burst, which is given in the observer reference frame, is related to the burst spectral luminosity L_{ν} (in units of erg s⁻¹ Hz⁻¹) in the FRB source rest frame, as (Marani & Nemiroff, 1996; Macquart & Ekers, 2018a):

$$S = (1+z)\frac{L'_{\nu}}{L_{\nu}}\frac{L_{\nu}}{4\pi D_L^2} , \qquad (1.17)$$

where D_L is the luminosity distance of the source, $L'_{\nu} \equiv L_{\nu}(1+z)$ and the ratio $\frac{L'_{\nu}}{L_{\nu}}$ is the so-called k-correction, which takes into account the fact that the radiation is emitted in another frequency band with respect to the observed one, as a result of the expansion of the Universe. Moreover, one has to consider the spectrum (i.e. the variation of the flux density or fluence as a function of the frequency) of the source, which usually is modelled as a power law:

$$S(\nu) \propto \nu^{-\beta} \,, \tag{1.18}$$

with β , known as the spectral index, being the slope of the spectrum. The latter can be related to the intrinsic, underlying emission mechanism of the FRB powering source (e.g. Yang, 2023) and it is still highly unconstrained by current observations (see Section 1.2.4 for further details). Taking into account the k-correction and the spectrum of equation (1.18) one can obtain the spectral luminosity:

$$L_{\nu} = \frac{4\pi D_L^2}{(1+z)^{1-\beta}} S \ . \tag{1.19}$$

Consequently, the spectral luminosity can be related to the burst fluence by making use of equation 1.16, or approximating the burst profile to a top-hat function having equivalent width W_e , and then computing the fluence as $\mathcal{F} = S \times W_e$. One has to remember that the duration of the burst is measured at the observer rest frame, and one should multiply the equivalent width by an extra (1+z) factor. In this way the spectral luminosity can be related to the fluence as

$$L_{\nu} = \frac{4\pi D_L^2}{W_e (1+z)^{2-\beta}} \mathcal{F} . \tag{1.20}$$

The typical FRB spectral luminosities are shown in Figure 1.4, compared to spectral luminosities of different astrophysical transient phenomena. As one can note, an FRB has a spectral luminosity exceeding by approximately 7 orders of magnitude those of GRPs, and are 10^{11-12} times more luminous than single pulses from known pulsars.

It is possible to compute the spectral energy of the burst (expressed in units of erg Hz⁻¹) from its spectral luminosity, by multiplying L_{ν} of equation 1.20 for W_e . Finally, one can recover the total energy budget as the spectral energy times the observed bandwidth $\Delta\nu$. This is true only in some cases, since some FRBs show very narrow spectra, with finite extents (~ 100 MHz, see e.g. Yang, 2023) within the observed bandwidths. Otherwise, if the FRB emission extends beyond the telescope bandwidth then one should multiply instead by the central frequency of observation (e.g. Zhang, 2022). This total energy is often referred to as the "isotropic" energy, because one usually assumes that the burst emission is distributed isotropically, i.e. over a solid angle of $\Omega = 4\pi$ sr. If, instead, the emission is beamed in a solid angle $\Delta\Omega$ in the direction of the observer, than the total emitted energy is lower by a factor of $f_b \equiv \max(\Delta\Omega/4\pi, 1/4\gamma^2) \le 1$, where $\gamma \equiv (1 - \frac{v}{c})^{-1/2}$ is the Lorentz factor of the FRB emitter, travelling at a velocity v.

Another physical quantity which is useful to characterise the magnitude of an astrophysical signal is the brightness temperature T_B . This is defined as the equivalent temperature of black-body radiation having brightness $B(\nu)$, emitted by a celestial body which is in a physical state of thermal equilibrium. The latter is defined as the flux density divided by the solid angle $d\Omega$ subtended by the source:

$$B(\nu) = \frac{S(\nu)}{d\Omega} , \qquad (1.21)$$

usually expressed in units of erg s⁻¹ Hz^{-1} m⁻² sr⁻¹.

The Rayleigh-Jeans approximation, $h\nu \ll kT_B^3$, holds for wavelengths typical of radio

³here $h \simeq 6.626 \times 10^{-34} \text{ J Hz}^{-1}$ is the Planck constant and $k \simeq 1.38 \times 10^{-23} \text{ J K}^{-1}$ is the Boltzmann constant.

observations, and one can show that the brightness temperature is related to $B(\nu)$ via the following expression:

$$T_B(\nu) = \frac{c^2}{2k\nu^2}B(\nu)$$
 (1.22)

Finally, one can relate $T_B(\nu)$ of a burst to its flux density, duration and frequency of emission (e.g. Luo et al., 2023) as:

$$T_B(\nu) \simeq (1.2 \times 10^{36} \text{ K}) \left(\frac{S}{\text{Jy}}\right) \left(\frac{\nu}{\text{GHz}}\right)^{-2} \left(\frac{W}{\text{ms}}\right)^{-2}$$
 (1.23)

The remarkable brightness temperatures derived for FRBs (i.e. $> 10^{32}$ K, as can be noted in Figure 1.4) far exceed any T_B permissible if electrons radiate independently (or incoherently). Figure 1.4 shows the $W-L_{\nu}$ space separation (set to 10^{12} K, Kellermann & Pauliny-Toth, 1969) between an incoherent and a coherent emission. Consequently, any mechanism must explain FRBs through a model based on coherent emission.

1.2.4 Spectral properties

Nowadays, the spectra of FRBs is one of their less well-characterised properties. Indeed, only the first repeater, R1, has been detected up to 8 GHz (Gajjar et al., 2018), while discovered at L-band. Initially, FRB spectra were thought to be flat, with emission extended over a wide range of frequencies, consistently with spectra of radio pulsations from magnetars (e.g. Karuppusamy et al., 2010). Instead, individual bursts from repeaters have been observed with extremely narrow spectra (Kumar et al., 2021; Pastor-Marazuela et al., 2021; Pleunis et al., 2021b; Zhou et al., 2022; Zhang et al., 2023a; Sheikh et al., 2023), sometimes extending over $\sim 10\%$ of the telescope bandwidth (Kumar et al., 2021), as for the extremely band-limited emission observed for repeating FRB 20190711 (see Fig. 1.5), which shows a Gaussian-like spectrum of only 65 MHz of bandwidth (corresponding to $\Delta\nu/\nu \sim 0.03$). On the contrary, one-off FRBs are statistically broader in bandwidth than repeaters, as resulting from the analysis of the Canadian Hydrogen Intensity Mapping Experiment (CHIME) bursts (Pleunis et al., 2021b; Chime/Frb Collaboration et al., 2023).

Remarkably, a single burst from FRB 20121102A (R1, hereafter, being the first repeater discovered) has been simultaneously detected at 1.4 GHz and 3 GHz, respectively (Law et al., 2017). Assuming a power law spectrum $F(\nu) \propto \nu^{\beta}$, the authors obtained a spectral index of $\beta = 2.1$. However, the latter result was inconsistent with the non-detection at 4.8 GHz conducted simultaneously with the Effelsberg radio telescope (Law et al., 2017). Therefore, the authors concluded that a single power-law function was not a good description for the broadband spectrum of the source. Furthermore, Chawla et al. (2020) reported a coincident detection of FRB 20180916B (R3) in adjacent frequency bands, i.e. 300-400 MHz and 400-600MHz. In this case, the burst in the CHIME band is downward drifting into the GBT band. This effect, known as "sad trombone", is commonly observed in the morphology of repeater bursts (e.g. Hessels et al., 2019). In the same work, no bursts have been detected in the Low Frequency Array (LOFAR) 110 - 190 MHz band, implying a lower limit on the broadband spectral index $\beta > -1.0$. Finally, the simultaneous detection of FRB 200428 at 600 MHz (CHIME/FRB Collaboration et al., 2020) and 1.4 GHz (Bochenek et al., 2020) gives a rough power law broadband spectrum of $\beta \sim 1$. However, in this case the flux density measured by CHIME is poorly constrained, given that this was a sidelobe detection.

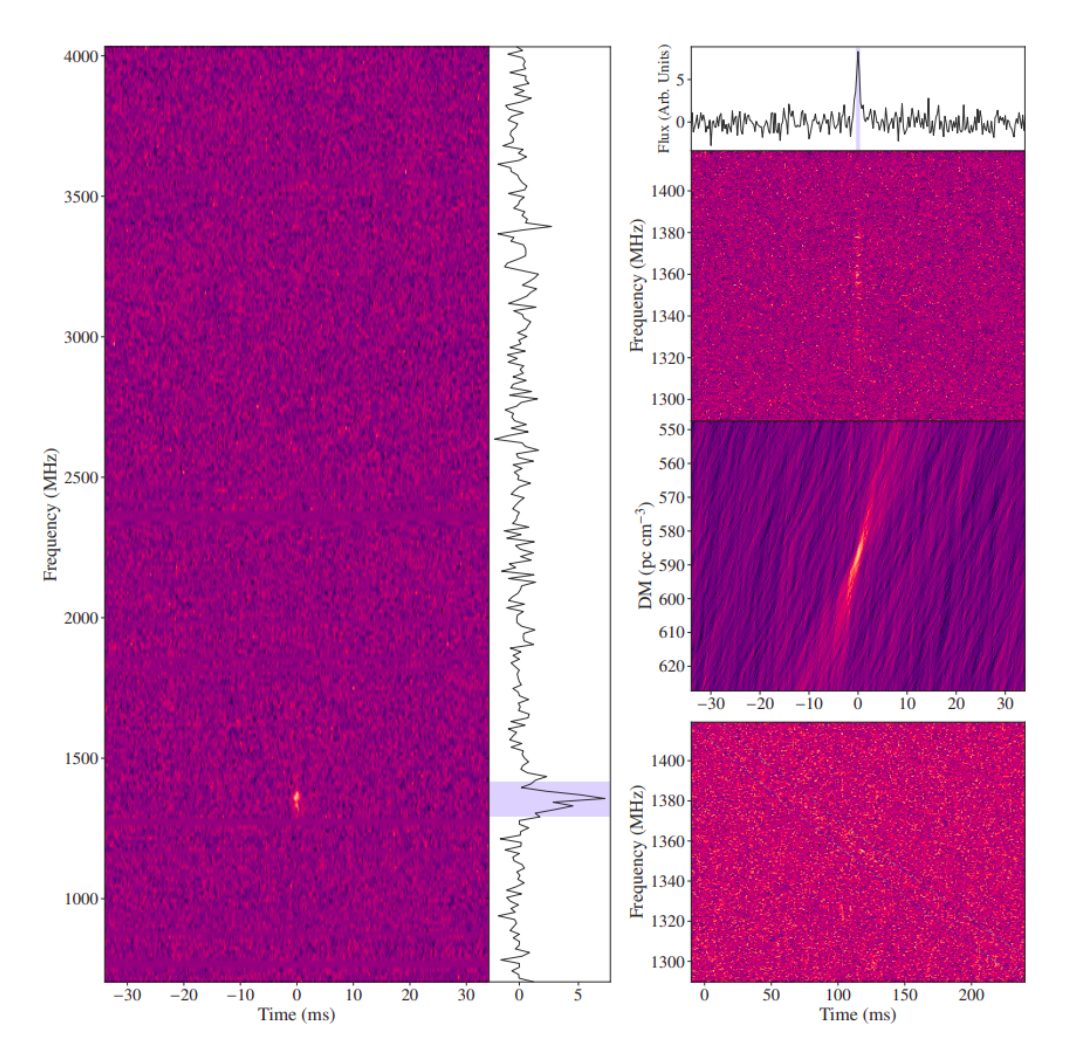


Figure 1.5: Left subplot: de-dispersed, dynamic spectrum of the extremely narrow-banded FRB 20190711. The time-averaged on-pulse spectrum is reported on the right-hand panel, with the on-pulse region highlighted as a blue shaded area. Right subplot: the top panel shows the de-dispersed waterafall plot, considering only the data around on-pulse emission. In particular, the top row of this panel shows the frequency averaged time series of the burst, the second row reports the time-frequency dynamic spectrum, and the third row shows the butterfly plot (time vs. DM) of the burst. The bottom panel shows the dispersed dynamic spectrum of the FRB signal. Credits to Kumar et al. (2021).

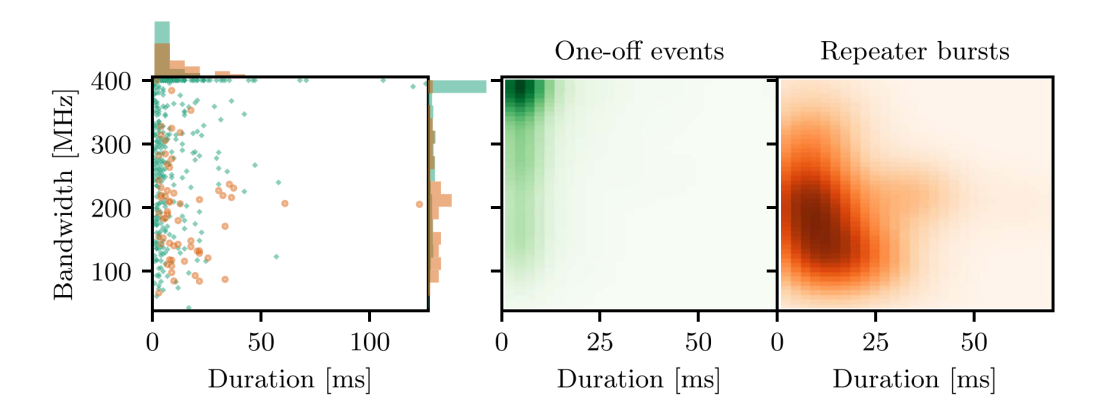


Figure 1.6: Bandwidth of activity vs. burst duration for FRBs present in the CHIME/FRB Catalog 1 (CHIME/FRB Collaboration et al., 2021) (474 one-off and 62 bursts from 18 repeating sources). The different colors represent the distinction between one-off events (green) and repeater bursts (orange). The panel on the right shows the distributions of all one-off events and repeater bursts. Credits to Pleunis et al. (2021b).

1.3 One off vs. Repeaters

Nowadays ~ 800 distinct FRB sources are known (CHIME/FRB Collaboration et al., 2021), the most of them classified as one-off events. However, a small fraction of FRBs (up to now 56 sources) exhibits repetitions in their emission, the so-called *repeaters*. It is worth noticing the remarkable contribution provided by CHIME (CHIME Collaboration et al., 2022) telescope: after it started its operations in 2018, the number of known FRBs has increased by more than an order of magnitude, from a few dozen to several hundreds. It is unclear whether repeaters represent a distinct population among all FRBs, though some statistical and observational differences between them and one-off bursts have been reported (Pleunis et al., 2021b; Chime/Frb Collaboration et al., 2023). In particular, Figure 1.6 shows that CHIME/FRB bursts from repeating sources appear statistically longer in duration and less extended in frequency. Some apparently non-repeating FRBs were found to be repeaters in the follow-up observations and some population studies suggest that a large fraction of one-off FRBs may eventually repeat (James et al., 2022a; James, 2023; Chime/Frb Collaboration et al., 2023). Various differences are found even within the repeater population, especially in their level of activity. Indeed, the burst rate of repeaters spans a wide range of values, ranging from less active sources, which exhibit a burst rate as low as $\sim 10^{-3} \text{ hr}^{-1}$ (Chime/Frb Collaboration et al., 2023) to the most active ones showing sporadic burst storms with hundreds of events per hour (Li et al., 2021b; Nimmo et al., 2022a; Xu et al., 2022; Zhang et al., 2022, 2023a; Feng et al., 2023).

Repeating and non-repeating sources are expected to exhibit different DM distributions (Gardenier et al., 2021). Indeed, FRBs can be detected only if their fluence is higher than a given threhsold, which in turn increases for more distant sources. Repeating sources require at least two bright bursts to be identified, while one-off bursts need only a single bright event. As a result, repeaters become less observable with distance compared to one-off bursts, and this should have an impact on the DM distribution of these two FRB classes. Interestingly, it is found that repeaters show a lower average DM than the corresponding value for one-off sources. For example, considering bursts from 305 one-off sources and 40 repeaters from the CHIME/FRB Catalog 1, it has been found a difference between the two average DM values of $\Delta \langle \mathrm{DM} \rangle \equiv \langle \mathrm{DM}_{\mathrm{one-off}} \rangle - \langle \mathrm{DM}_{\mathrm{rep}} \rangle = 162 \pm 55 \; \mathrm{pc} \; \mathrm{cm}^{-3} \; (\mathrm{Chime/Frb} \; \mathrm{Collaboration} \; \mathrm{et} \; \mathrm{al.}, \; 2023).$ Moreover, the DM distributions are consistent, although with still slightly low significance, with being drawn from two different underlying distributions. This difference, if confirmed as real (i.e. not only due to only to observational selection biases), could in principle represent a

strong evidence for one-off and repeaters being two different physical classes of sources. The origin of this difference could be due to different distribution in redshift space, host galaxy type or local environment (Chime/Frb Collaboration et al., 2023). However, a selection bias has to be taken into account, given that repeaters would be detected preferentially in the Local Universe (Gardenier et al., 2021; James, 2023). This is because, if all FRB sources emit with a given luminosity function, the further away, the higher and more limiting the corresponding luminosity threshold will be. Therefore, distant sources must be way brighter to be observed than nearby ones. For repeaters, this effect is even stronger, since, in order to classify a source as a repeater, one needs to detect at least two different bursts. Henceforth, one expects the repeater population to drop off faster with distance than the observed one-off population.

1.3.1 Hyperactive repeaters

As already mentioned, not all repeaters are equally active. Up to now, 6 repeaters, i.e. R1, R1-twin, FRB 20201124A, FRB 20200120E, FRB 20220912A and FRB 20240114A, showed active states of bursting activity, lasting for days (Nimmo et al., 2022a) or months (Kirsten et al., 2024), with a high cadence and usually also with bright bursts. R1 is the first FRB that showed an enhanced period of bursting activity, usually referred to as a burst storm. FRB 20200120E, which is also the nearest FRB source known (Bhardwaj et al., 2021a) (see Section 1.4 for details), produced a storm of 53 bursts within a time span of 40 minutes (Nimmo et al., 2022a) with a peak burst rate of 252 hr⁻¹ for $\mathcal{F} \geq 40$ mJy ms. Moreover, this FRB source revelead extremely short sub-bursts, but also single, isolated bursts, characterized by durations of tens of nanoseconds (Majid et al., 2021; Nimmo et al., 2022b), resembling nano-shots of the Crab pulsar (e.g. Hankins & Eilek, 2007; Jessner et al., 2010). Still, these bursts are ~ 500 times more luminous than GRPs (Majid et al., 2021), yet filling the gap between the latter and the bulk of extragalactic FRBs.

Another well-studied repeater, FRB 20201124A, had a very active phase between March and May 2021 (e.g. Lanman et al., 2022; Marthi et al., 2022; Zhang et al., 2022) and shows sparse bursts afterwards (Kirsten et al., 2024). No high frequency bursts (with $\nu > 3$ GHz, nor periodic activity were conclusively observed for this source, despite the current abundance of events. Among the most active repeaters known, FRB 20220912A (McKinven & Chime/Frb Collaboration, 2022) stands out, with an exceptionally high burst rate (as high as $\sim 400 \text{ hr}^{-1}$) reported at 1.4 GHz (Zhang et al., 2023a). Despite many hours of monitoring, no bursts have been detected at frequencies higher than 2.3 GHz (e.g. Kirsten et al., 2022b). FRB 20220912A has proven to be particularly active at frequencies $\nu < 1$ GHz as well, with multiple detected bursts reported by CHIME/FRB⁴. Also the Northern Cross detected activity at 408 MHz, soon after its discovery (e.g. Pelliciari et al., 2022) and during a dedicated long monitoring campaign (Pelliciari et al., 2024a, but see Chapter 4). Finally, one of the latest repeater discovered by CHIME, FRB 20240114A (Shin & CHIME/FRB Collaboration, 2024), has shown exceptionally high fluence bursts, reaching even a ~ kJy ms level (Shin & CHIME/FRB Collaboration, 2024; Ould-Boukattine et al., 2024), and a $\sim 500 \text{ hr}^{-1}$ repetition rate for bursts having fluence $\mathcal{F} > 15$ mJy ms (Zhang et al., 2024). The extremely high burst rate revealed by dedicated deep monitoring campaigns can be used to constrain coherent radiation models. For instance, the popular synchrotron maser models (see Section 1.5) need well-ordered magnetic field lines in the upstream regions of the shock. Clustered FRBs imply successive shocks moving into an already shocked, hot medium with likely distorted magnetic field lines. The short waiting times, i.e. the difference between the arrival times of consecutive bursts, challenge these models in terms of whether coherent emission can occur with such brief intervals.

⁴All the CHIME/FRB bursts detected from the source, as well as from FRBs in general, are reported in the CHIME/FRB Catalog 1, available at the following link: https://www.chime-frb.ca/catalog

Statistically robust studies allowed by the collection of an high number of bursts, revealed some interesting peculiar properties of the bursts emitted. Remarkably, the waiting-time distribution of R1, FRB 20201124A and FRB 20220912A show a characteristic double peak (Zhang et al., 2021; Hewitt et al., 2022; Zhang et al., 2023a), with the left peak (i.e. the one at lower waiting time values) always being lower than the right one (see Figure 1.7). Interestingly, a similar waiting-time distribution is observed for some soft gamma-ray repeaters (SGRs) (Göğüş et al., 2000; Wang & Yu, 2017), which are a type of neutron star emitting strong X- and γ -ray bursts at irregular intervals (see Kaspi & Beloborodov, 2017, for a review on SGRs), nowadays definitively recognised as magnetars. Fitting this distribution with two lognormal functions, Zhang et al. (2023a) find the two peaks at 18 s and 50 ms for FRB 20220912A. Similar values are found for FRB 20201124A, with the left peak observed at 39 ms (Xu et al., 2022) and 53 ms (Zhang et al., 2022), as observed in two different burst storm episodes. In Xu et al. (2022) the observed right (long-term) peak is ~ 135 s, i.e. approximately 10 times larger than 10.05 s as measured in Zhang et al. (2022). This observed difference suggests that the waiting-time distribution is not a universal property for a given source, but rather may depend or even correlate with its activity level (Zhang et al., 2022). For R1, the bimodal distribution is still evident but with a left peak at 3 ms (e.g. Hewitt et al., 2022). Overall, the origin of this bimodality is still unknown, although it is plausible that it arises from absorption processes during the FRB path into the magnetosphere of a magnetar, as well as in the IGM (see, e.g. Xiao et al., 2024, for further details).

Another interesting feature relies in the energy distribution of repeating sources. Firstly, during a burst storm from R1 observed with FAST, a bimodal energy distribution has been reported (Li et al., 2021b). In particular, the latter can be well fitted at the low and high energetic ends by a log-normal and a generalized Cauchy function, respectively, although for high energies, i.e. $E_{\rm iso} \geq 10^{34}$ erg, also a simple power law with index $\alpha = 1.85 \pm 0.30$ well approximates the distribution. Afterwards, the same bimodality has been reported from a burst storm of FRB 20201124A (Zhang et al., 2022). The fact that these distributions show different components could represent the hint for different emission mechanisms, emission sites or beam shapes between low and high energetic bursts (Li et al., 2021b). Finally, for the same two hyperactive repeaters, a flattening in the cumulative burst energy rate is observed (Hewitt et al., 2022; Kirsten et al., 2024), resembling the cumulative luminosity distribution of the population of one-off sources. We investigate better this phenomenon in Chapter 4, where we show that also FRB 20220912A presents this type of flattening in its burst energy distribution.

Hyperactive repeaters represent the best candidates to study deeply the physical properties of FRBs, given their high observed burst rates. Further high-cadence monitoring and statistical analysis will be crucial in unraveling the complex physical processes at play and in refining theoretical models of FRB progenitors.

1.3.2 Periodic FRBs and quasi-periodicities

The majority of repeaters known up to now have shown sporadic periods of higher bursting activity. However long follow-up observations revealed that two repeating FRB sources, R1 and R3, show remarkable periodicity in their emission. The latter manifests itself in the form of periodic activity windows, when the source cyclically turns active for a certain time window W_a of time, and the onset has period P_a . During the active state, no strict (e.g. pulsar-like) periodicity is observed. The first FRB showing this behaviour is R3 (Pleunis et al., 2021a), for which the source stays active for $W_a = 5.4$ days, every $P_a = 16.3 \pm 0.12$ days (Pleunis et al., 2021a). Overall, the burst activity of the source remained approximately constant over ~ 4 years, with a burst rate well described by a Poisson distribution (Sand et al., 2023). Soon afterwards, periodicity was also claimed for R1 with an activity cycle of $P_a = 161 \pm 5$ days (Rajwade et al.,

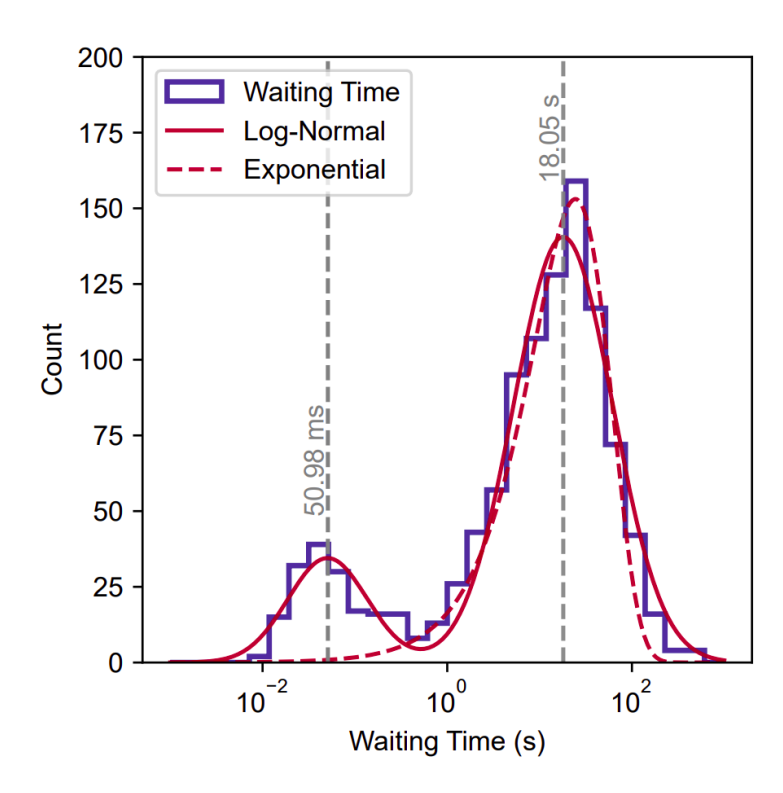


Figure 1.7: Waiting-time distribution of bursts detected with FAST at 1.4 GHz from the hyperactive repeater FRB 20220912A. The grey dashed lines highlight the two peaks of the distribution of the waiting times, which is clearly bimodal. The same feature is found for other two hyperactive repeaters, i.e. R1 (Zhang et al., 2021) and FRB 20201124A (Hewitt et al., 2022). Credits to Zhang et al. (2023a).

2020; Cruces et al., 2021) in which the source stays active for approximately $W_a \sim 90$ days. Recently, another, shorter, 4.6 days periodicity has been found from the analysis of 1145 radio bursts from R1, detected with multiple radio telescopes (Li et al., 2024). R1 showed several burst storm episodes (e.g. Jahns et al., 2023). Up to now, such a periodicity has not been found for other repeating sources (see e.g. Lanman et al., 2022, for the case of FRB 20201124A).

The rotation of a magnetar characterised by an ultra-long period has been suggested to explain the 16-day periodicity of R3 (Beniamini et al., 2020). Such a magnetar is supposed to have an age comparable to Galactic magnetars (i.e. $\sim 1-10$ kyr). Interestingly, this age is consistent with the time it would take the magnetar to travel the observed spatial offset between the R3 localisation region and a star-formation region (Tendulkar et al., 2017) (see Section 1.4 for details on R3 localisation). However, magnetars in our Galaxy have shown sporadic bursts of activity, which is slightly in contrast with the Poissonian nature of the R3 burst rate. Other models explain the observed periodicity in the form of a precessing flaring magnetar/radio pulsar (Levin et al., 2020; Zanazzi & Lai, 2020) or a binary system, such as a pulsar in orbit with a O/B type star (Lyutikov et al., 2020) or with a Be companion (e.g. Li et al., 2021c).

FRB periodicity has favoured multi-wavelength observations, permitting to plan multi-telescope and multi-wavelength observations. Indeed, multi-wavelength observations conducted between ~ 150 MHz (Pastor-Marazuela et al., 2021) and 6 GHz (Bethapudi et al., 2023) revealed a chromatic pattern for the periodic emission of R3. In particular, within the R3 activity window, high frequency bursts arrive systematically earlier than low frequency ones (Pastor-Marazuela et al., 2021; Pleunis et al., 2021a). This behaviour is shown in Figure 1.8, where activity phases from telescopes observing at different observing frequencies are reported. For example, bursts detected by Apertif (Pastor-Marazuela et al., 2021) at 1.4 GHz occur ~ 0.7 days earlier than CHIME/FRB bursts. The same chromatic property has not been observed in R1. Rather, the

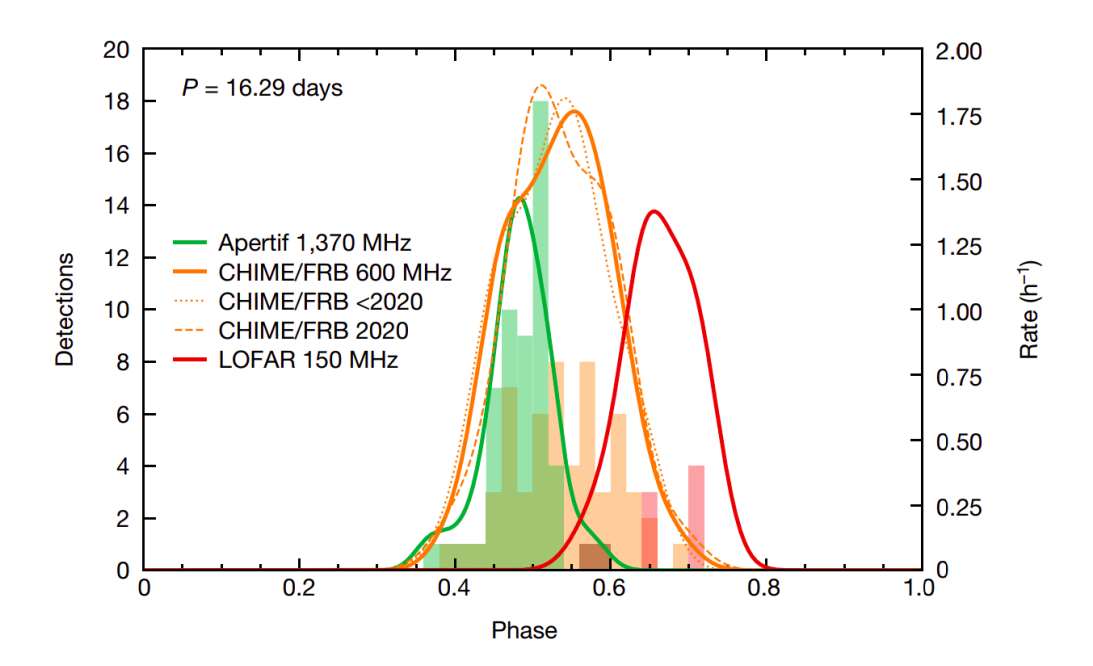


Figure 1.8: Frequency dependent activity windows versus phase for R3, obtained considering a period of 16.3 days. The histograms represent the number of burst detections for different observing stations, while solid lines represent the associated smoothed distributions. Credits to Pastor-Marazuela et al. (2021).

phases seem to be randomly distributed as a function of the frequency ⁵.

In addition to the long-term periodicities we have discussed so far, short-term quasi-periodicities have also been observed. Here the "quasi" term means that there is not a strict periodicity but rather a regular time separation between different sub-bursts. FRB 20191221A, discovered by CHIME/FRB, showed a very long, $W \sim 3$ s, burst showing sub-burst structures regularly separated in time (Chime/Frb Collaboration et al., 2022). The reported period of the sub-bursts is 216.8 ± 0.1 ms, having a high 6.5σ significance. Another interesting case is FRB 20201020A, which emitted a ms-long burst with sub-bursts separated with a ~ 0.4 ms quasi-periodicity, however at low significance (2.4 σ) (Pastor-Marazuela et al., 2023). It is worth noticing that these FRBs are (seemingly) one-off sources. The only repeater, at least up to now, who showed quasi-periodic separations between sub-bursts is FRB 20200120E (Majid et al., 2021). On the countrary, the hyperactive sources R1 and FRB 20201124A have not shown any sub-burst periodicities, over thousands of bursts and long monitoring (Li et al., 2021b; Cruces et al., 2021; Kirsten et al., 2024). The properties of quasi-periodic substructures observed in FRBs could be used to infer the underlying rotation period of the magnetar (Kramer et al., 2024), assuming it is confirmed that magnetars are responsible for FRB emission.

1.4 Host galaxies and precise localisations

The discovery of the repeating nature of R1 facilitated targeted observations on this source, finally permitting the association between the FRB source and its host galaxy. This was the first evidence that the source of FRBs indeed are at extragalactic distances, as already suggested by their high DM values. Knowing the host galaxy of an FRB source is of fundamental importance in order to shed light on FRB progenitor theories (see Section 1.5 for details). Indeed, certain progenitors like, e.g., a younger one such as a magnetars, would be associated with star-forming

⁵see M. Trudu's Ph. D. Thesis, Section 1.4, https://iris.unica.it/handle/11584/359381.

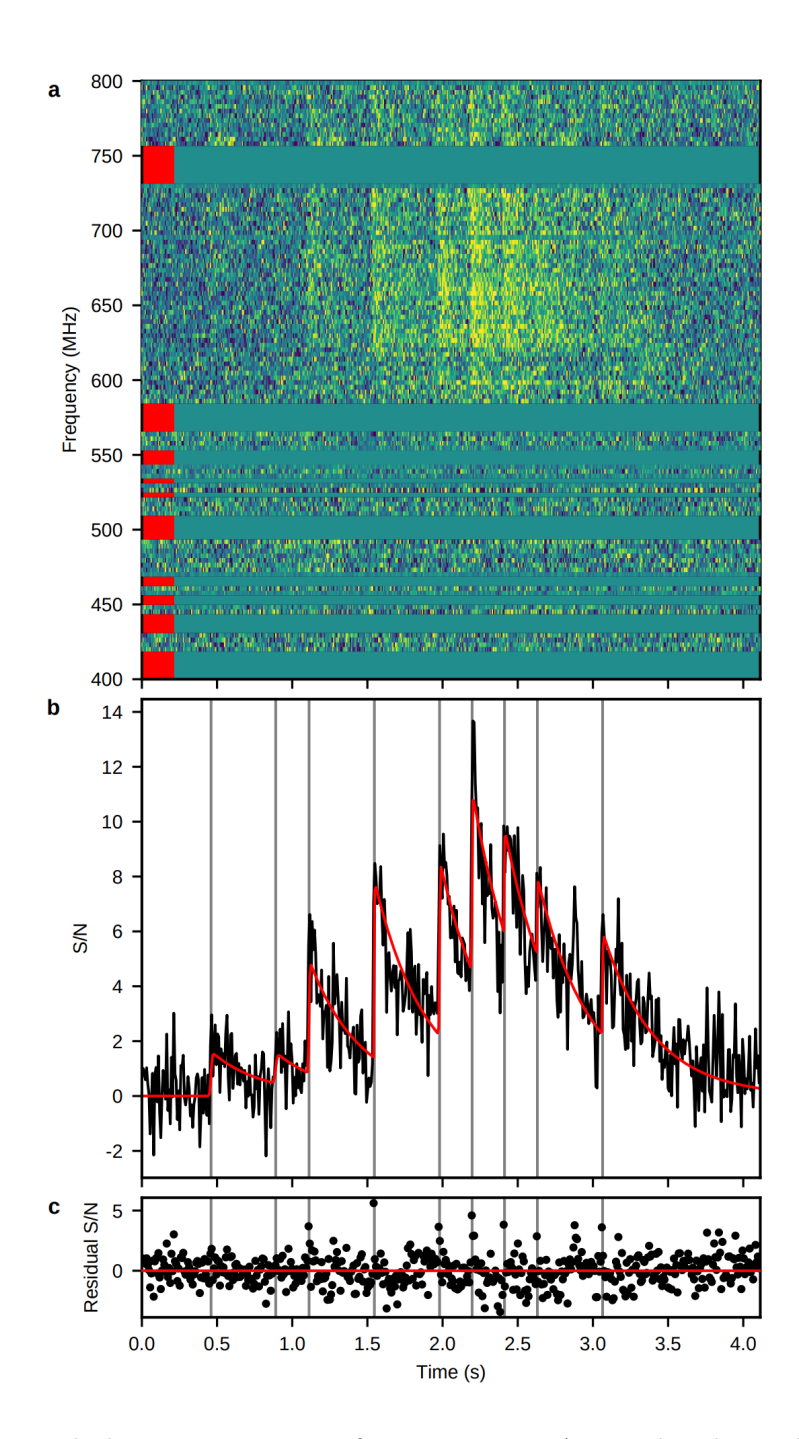


Figure 1.9: De-dispersed, dynamic spectrum of FRB 20191221A. Panel a shows the signal intensity as a function of time and frequency. Frequency channels masked due to RFI are indicated in red. Panel b represents the frequency-integrated pulse profile. An exponential model (red line) is used to model nine peaks in the profile. Peaks locations are highlited with vertical gray lines. Panel c shows the residuals of the fit. Credits to Chime/Frb Collaboration et al. (2022).

regions and so to late-type galaxies. Moreover, the FRB association to its host galaxy allows to determine its redshift, enabling the use of FRBs as probes of the intergalactic matter content, even without knowing what its actual progenitor is. The FRB-host galaxy associations were possible through radio interferometric observations (e.g. Bannister et al., 2019; Ravi et al., 2023), such as the VLA, the Australian Square Kilometre Array Pathfinder (ASKAP), the Deep Synoptic Array (DSA-10), and the European very long baseline interferometry Network (EVN). In particular, up to now only the EVN can reach milli-arcsecond spatial resolution, needed to pinpoint FRBs within their hosts, so one can study in detail the local environments around the FRB source.

R1 has been associated with an irregular, low-metallicity dwarf galaxy at redshift $z \sim 0.19273 \pm 0.00008$ (Tendulkar et al., 2017; Bassa et al., 2017) via Very Large Array (VLA) observations (Chatterjee et al., 2017), in which a 0.1 arcsecond accuracy was reached, enough for the FRB-host galaxy association. Interestingly, a persistent radio source (PRS), spatially coincident with the bursts position was also discovered (Chatterjee et al., 2017; Tendulkar et al., 2017). Follow-up observations using the EVN permitted to precisely pin-point the FRB source in the vicinity of a star-forming region inside the host galaxy, and to assess the position of the FRB and PRS to be within ~ 40 pc (transverse physical offset). In particular, the properties of the host galaxy of R1 are consistent with the hosts of superluminous supernovae (SLSNe)⁶ and long-duration γ -ray bursts (lGRBs), and therefore support the idea that the progenitor of R1 is a young NS, or a magnetar (Bassa et al., 2017).

R3 was precisely localized 250 pc away from a knot of star-formation (Marcote et al., 2017; Bassa et al., 2017; Tendulkar et al., 2021), in a relatively nearby galaxy with a redshift of z=0.0337. Given the time it would take for the progenitor of FRB 20180916B to travel such a distance, theories that involve a young magnetar (with an age of $10-10^5$ years) are problematic. For context, the thickness of our Galaxy's disk is only 20-30 pc (Olausen & Kaspi, 2014). Although this thickness is measured perpendicular to the plane of the disk, whereas the offset of FRB 20180916B relative to the star-formation knot is along the plane, comparing these distances assuming an isotropic natal kick of a neutron star is still informative. Consequently, the most widely supported model involves a magnetar with a significantly older age (greater than 50 million years) (Tendulkar et al., 2021).

Even more intriguing is the localization of FRB 20200120E, the nearest known extragalactic FRB, in the spiral galaxy M81 (Bhardwaj et al., 2021b), only 3.37 Mpc away. Indeed, very long baseline interferometry (VLBI) observations have shown that this FRB is located at a projected distance of only 2 pc from the optical center of a globular cluster (GC) in M81 (Kirsten et al., 2022a). Given that GCs host old stellar populations, the standard core-collapse magnetar formation channel is unlikely (Kirsten et al., 2022a). However, magnetars can still be formed by other formation channels, such as accretion-induced collapse of WDs or mergers of compact binaries. These scenarios could still reconcile the bursts of FRB 20200120E as produced by a relatively young magnetar in this location (Kirsten et al., 2022a; Kremer et al., 2023).

After the localisation of R1, 45 FRB sources (e.g. Gordon et al., 2023b), both one-off and repeaters, have been associated with a host galaxy. The furthest FRB known up to now is FRB 20220610A, having redshift $z \simeq 1.017$ (Ryder et al., 2023), and localised in a star forming host galaxy being part of a compact galaxy group (Gordon et al., 2023a). In general, the majority of FRBs have been associated to mildly star-forming galaxies. Indeed, other than the GC FRB, FRB 20220509G has been localised in a quiescent, early-type galaxy at z = 0.0894 that belongs to the galaxy cluster Abell 2311 (Connor et al., 2023; Sharma et al., 2023). These discoveries pose challenges towards a single progenitor scenario for FRBs, but suggest that the majority of FRBs could originate from young stellar populations, while some of them could originate

⁶A SLSN is a type of stellar explosion with a luminosity at least ten times greater than that of standard SN. SLSNe are thought to be produced by various mechanisms, including millisecond magnetars.

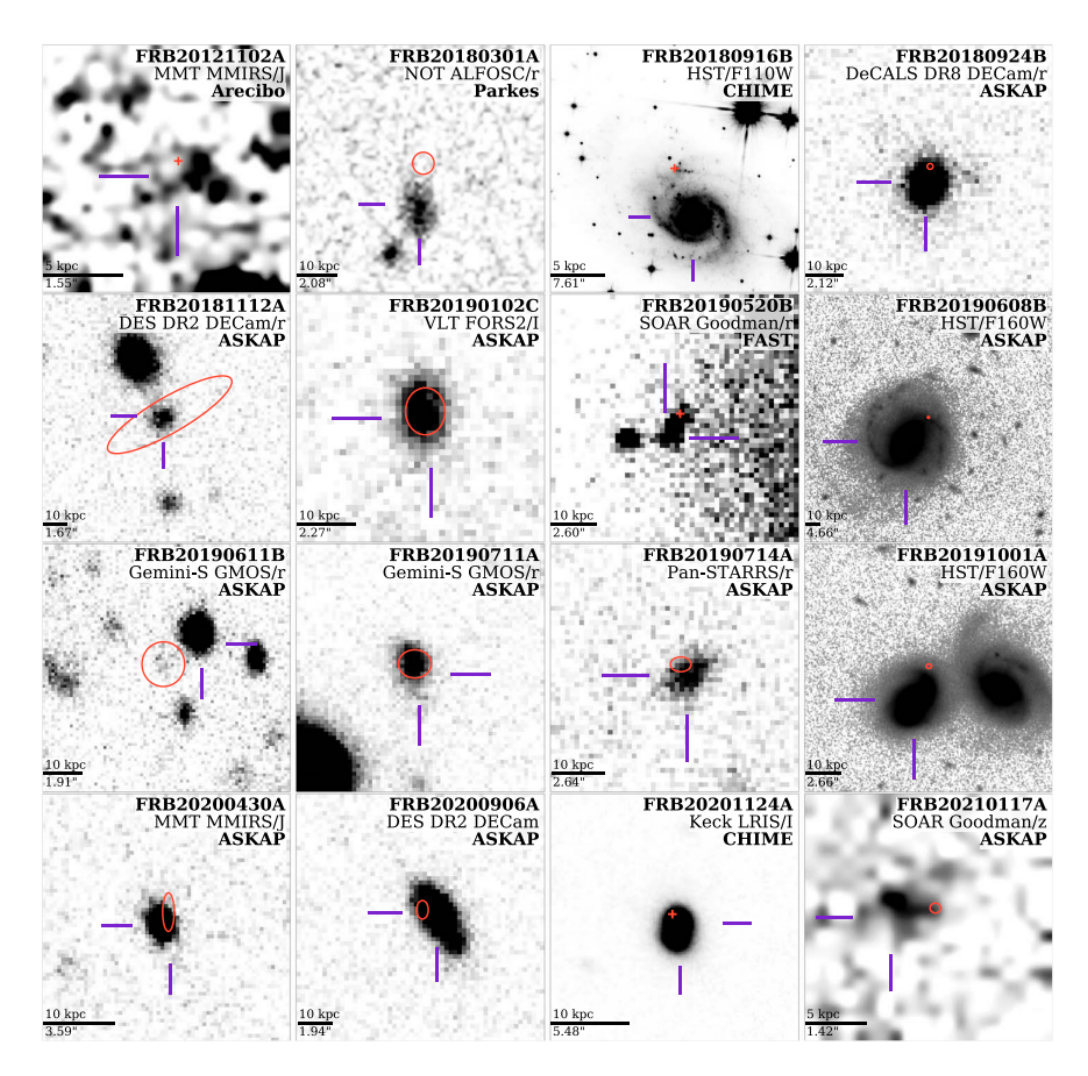


Figure 1.10: A sample of FRB host galaxies, with FRB localisation uncertainties marked with red ellipses. For 3 repeaters known at milli-arcsecond precision, their position is shown as a red plus symbol. Credits to Gordon et al. (2023b).

from old stellar populations. Notably, no statistically significant differences were found between repeaters and one-off sources in terms of stellar population properties in a sample of 23 localised FRBs (Gordon et al., 2023b). Although the number of localised FRBs is still low to obtain a good statistics, this could imply that the one-off vs. repeaters dichotomy is only apparent.

1.4.1 Persistent radio sources associated with FRBs

The milliarcsecond localisation precision achieved for some actively repeating FRBs (e.g. Marcote et al., 2022) allowed the intriguing discovery of persistent radio sources (PRSs). A PRS is a radio continuum source with position consistent with the FRB localisation coordinates, with $L_{\nu} > 10^{27} \text{ erg s}^{-1} \text{ Hz}^{-1}$ (Law et al., 2017) and appears compact (e.g. < 10 pc for R1, Marcote et al., 2017), i.e. non-resolved, at milli-arcsecond scales. These properties are inconsistent with typical values inferred from star-formation processes. Up to now, only two confirmed PRSs are known, both being associated with two actively repeating FRBs: R1 (Chatterjee et al., 2017) and FRB 20190520B (R1-twin; Niu et al., 2022). These FRB sources are very similar in terms of burst activity, host galaxy properties (Niu et al., 2022) and very high rotation measure⁷ (RM, Michilli et al., 2018; Anna-Thomas et al., 2023). In terms of spectral energy distribution (SED), the known PRSs exhibit flat radio spectra, with a spectral index $\beta \sim -0.27$ for R1 (Marcote et al., 2017) and $\beta \sim -0.4$ for R1-twin (Niu et al., 2022; Bhandari et al., 2023). In particular, the SED of the PRS associated with R1 resembles the Crab (PSR B0531+21) pulsar wind nebula, but with a magnetic field three orders of magnitude higher to match the implied energetics of the PRS (Resmi et al., 2021). For these reasons the concordance picture for the radio emission of their PRSs is a strongly ion-electron magnetized wind nebula powered by a young actively flaring magnetar (Margalit & Metzger, 2018). Interestingly, VLBI observations of R1-twin are also consistent with a hypernebula powered by the accretion of a central compact binary system (Sridhar et al., 2024; Bhandari et al., 2023). A third putative PRS is the one associated with FRB 20201124A, another very active FRB source (e.g. Zhou et al., 2022). Observations conducted with the VLA revealed the presence of a persistent, extended radio source coincident with the FRB position (Piro et al., 2021). However, at milliarcsecond scales the same radiation is completely resolved out (Nimmo et al., 2022a), ascribing the continuum radiation to extended star formation occurring near the FRB environment (Piro et al., 2021).

Since the discovery of the two known compact PRSs, numerous radio observations were conducted to monitor their flux variation over time. Regarding the PRS associated with R1, its flux density at 3 GHz has been observed to vary by $\sim 10\%$ over day timescales, consistent with the expected scintillation phenomenon in the MW (Chatterjee et al., 2017; Waxman, 2017). However, on a timescale of about 3 years, Rhodes et al. (2023) reported a flux variation at 1.28 GHz of approximately 30%, potentially intrinsic to the source. Spectroscopic observations of the H α emission line conducted with the Keck telescope allowed Chen et al. (2023) to estimate the mass of a hypothetical BH as the origin of PRS-R1 to be in the range of $10^{4-5}~M_{\odot}$, using stellar velocity dispersion measurements from the host galaxy. The measured radio luminosity of this source appears to be too high for a BH of this mass, considering the general population of active galactic nuclei (AGN) (Chen et al., 2023). Moreover, the level of flux density variation seems inconsistent with scintillation if the source is an AGN. Regarding the PRS associated with R1-twin, multiwavelength VLA observations have shown a putative $\sim 20\%$ decrease in flux density at 3.2σ level over a 1 yr timescale (Zhang et al., 2023c). However, VLBI observations over 2 yr timescales have reported no flux variation (Bhandari et al., 2023).

In general, a stable and constant flux density after about 1 year disfavors the scenario where

⁷The RM quantifies the extent of Faraday rotation, i.e. the change in the polarization angle of linearly polarized light as it travels though a magnetized plasma. It is proportional to the strength and direction of the magnetic field along the LOS and the electron density in the invervening medium.

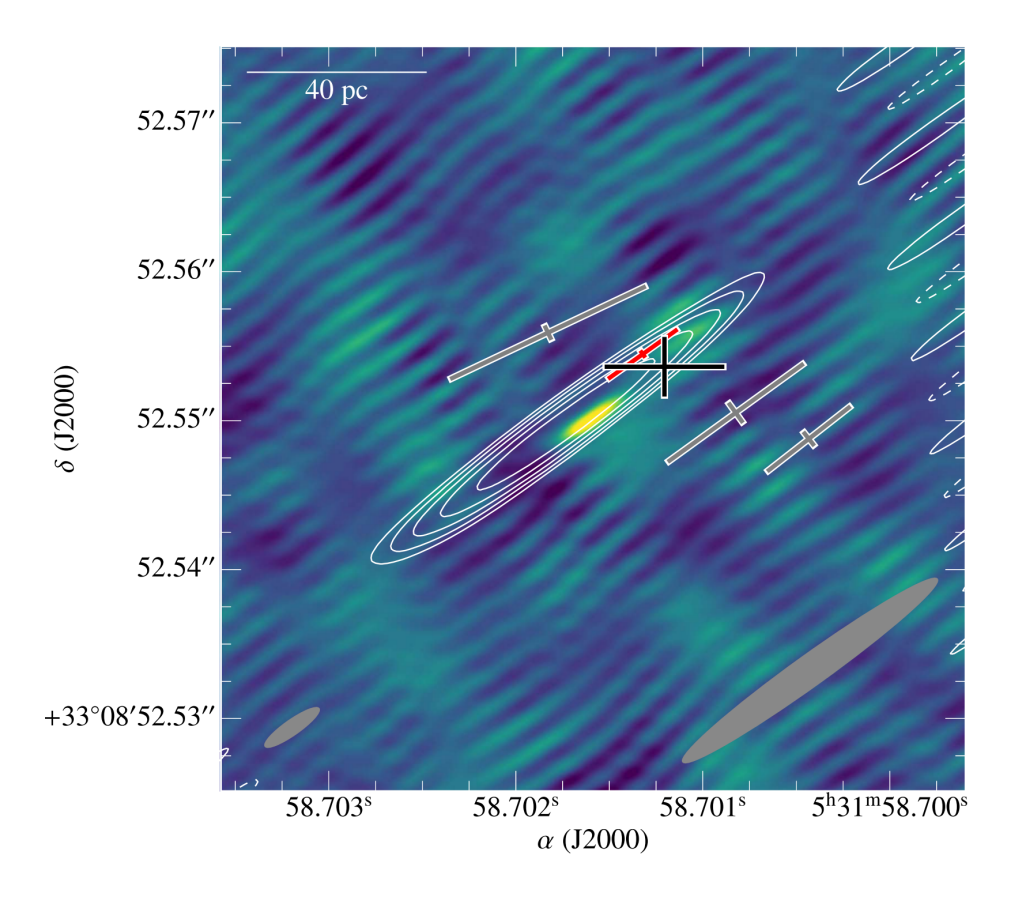


Figure 1.11: EVN image of the PRS associated with R1 at 1.7 GHz (white contours). During the observation, four bursts were detected. The red cross represents the localization of the strongest of them, the gray crosses represent the localization of the other three, and the averaged position of all four bursts is shown as a black cross. The lengths of the crosses indicate 1σ uncertainty in each direction. Contours start at a 2σ , with $\sigma = 10~\mu\text{Jy}$ the rms noise, increasing by factors of $\sqrt{2}$. The color scale shows the image at 5 GHz. The synthesized beam at 5 GHz is represented by the gray ellipse at the bottom left, the one at 1.7 GHz is at the bottom right. Dashed contours represent negative levels. Credits to Marcote et al. (2017).

the observed radio emission is caused by a young supernova remnant (Plavin et al., 2022). It is interesting to note that the bursts emitted by R1 are almost completely linearly polarized, while the PRS is unpolarized. This suggests that the PRS and the bursts do not share the same nature, or rather, that the PRS cannot be viewed as a buildup of bursts with low signal-to-noise ratio (S/N) (Gourdji et al., 2019).

The similarity between the PRSs associated with R1 and R1-twin motivated the search for PRSs having high luminosity in nearby dwarf galaxies (Vohl et al., 2023; Dong et al., 2024). For example, Vohl et al. (2023) searched for sources meeting these criteria in the LOFAR Two-Meter Sky Survey (LoTSS) source catalog, with evidence that they are not radio AGNs. From their results, it was possible to set a lower limit on the number density of compact radio sources at arcsecond scales of $856 \pm 150~\rm Gpc^{-3}$ above a flux threshold of 0.8 mJy at 144 MHz. Considering a sample of 15 localized FRBs with radio sensitivity limits that could allow the detection of a PRS (including six repeating FRBs), Law et al. (2022) estimated that the presence of a PRS could be up to 20% for repeating FRBs, as 2 out of the 6 repeating FRBs in their sample are associated with a PRS.

1.5 FRB progenitors and emission models

The interplay between observational data and theoretical advancements is crucial for unraveling the mysteries behind the FRB phenomenon. Technological advancements in radio telescopes and arrays, most of all the CHIME/FRB experiment, have significantly advanced the FRB research. CHIME not only reported the first discoveries of repeaters (although R1 was firstly discovered by Arecibo), but also the first FRB source catalog⁸ (CHIME/FRB Collaboration et al., 2021). Now that the FRB sample is becoming large, i.e. for now $\sim 10^3$ sources known, and sources become to be studied deeper both in time and spectral behaviour, observations can begin to better investigate theoretical models for both FRB progenitors and emission mechanisms, the latter, nowadays, still largely unconstrained.

Regarding progenitor theories, the most invoked are those that postulate that FRBs arise from the flaring activity of strongly magnetized NSs known as magnetars (Duncan & Thompson, 1992; Rea & Esposito, 2011; Turolla et al., 2015; Kaspi & Beloborodov, 2017). The latter, as opposed to pulsars, are not powered by their rotation, but instead by the decay of their strong (10¹⁴ – 10¹⁶ G), internal magnetic fields (Duncan & Thompson, 1992; Thompson & Duncan, 1995). Some observational evidences that magnetars could represent viable FRB progenitors are, e.g., the high linear polarization of the majority of known FRBs (Qu & Zhang, 2023); the high values of RMs of some highly active repeaters (e.g. Michilli et al., 2018; Niu et al., 2022), which may indicate a complex and strongly magnetized environment near the FRB production site; the spatial association of FRBs with star-forming regions (Bassa et al., 2017; Tendulkar et al., 2017; Marcote et al., 2020) and, in general, with host galaxies having high specific star formation rate (sSFR)⁹ (e.g. Gordon et al., 2023b) and an high volumetric rate of magnetar birth to explain the observed FRB rate (e.g. Nicholl et al., 2017; Cordes & Chatterjee, 2019).

But most of all, the FRB-magnetar connection was strengthened by the detection of FRB 20200428, the first ever Galactic FRB-like event, simultaneously discovered by CHIME (CHIME/FRB Collaboration et al., 2020) at 400 – 800 MHz and by the Survey for Transient Astronomical Radio Emission 2 (STARE2) at 1.4 GHz (Bochenek et al., 2020). Simultaneously, an X-ray burst was detected (Mereghetti et al., 2020; Ridnaia et al., 2020; Li et al., 2021a; Tavani et al., 2021), and identified with the soft gamma repeater J1935+2154 (SGR1935 –hereafter), one of the most active known magnetars (Stamatikos et al., 2014; Lien et al., 2014; Cummings,

⁸https://www.chime-frb.ca/catalog

⁹The latter is defined as the amount of SFR divided by the stellar mass of the host galaxy.

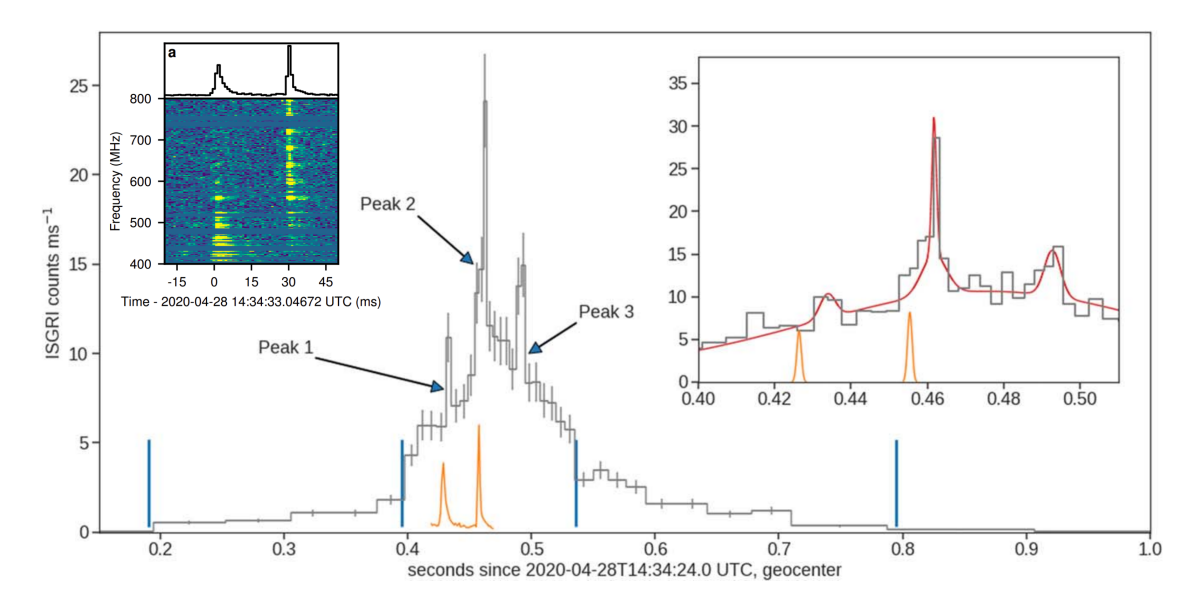


Figure 1.12: INTEGRAL 20–200 keV light curve (solid gray line) of the X-ray burst emitted by SGR J1935+2154. The orange line represents the position of the CHIME radio bursts, of which the de-dispersed dynamic spectrum is reported in the inset on the upper-left corner. The inset on the right shows a zoom-in on the burst arrival times, highlighting the proximity of the radio pulses to their X-ray counterparts. Adapted from Mereghetti et al. (2020); CHIME/FRB Collaboration et al. (2020).

2014; Kozlova et al., 2016; Younes et al., 2017). The simultaneous radio-X-ray detection of FRB 20200428 is represented in Figure 1.12, where the X-ray INTEGRAL light curve is reported, along with the arrival times of the CHIME burst. FRB 20200428 had an isotropic radio energy of $E_{\rm SGR} \simeq 2 \times 10^{34}$ erg (Bochenek et al., 2020; Margalit et al., 2020b), which is ~ 4 –5 orders of magnitudes higher than GPs from known pulsars (see e.g., Kuzmin, 2007) and ~ 1 order of magnitude lower than the least energetic extragalactic FRB (FRB 20200120E, Bhardwaj et al., 2021b). As shown in Figure 1.12, the X-ray bursts arrive 6.5 ± 0.1 ms after the radio pulses (Mereghetti et al., 2020), if one associates the CHIME bursts to the first and second X-ray peaks. Instead, if one associates them to the second and third peaks, then the implied delay becomes approximately 35 ms. In any case, the close time coincidence of the radio and X-ray emission are somewhat preferred by magnetospheric models (see, e.g., Lyutikov, 2002; Lyubarsky, 2020), but can be explained also for bursts originating at very large distances from the surface of the NS (Beloborodov, 2020; Margalit et al., 2020b).

Despite the evidence, no galactic magnetar showed long periods of bursting activity, especially at radio wavelengths, as the long-lived ones observed from, e.g., R1 for \sim 11 years up to now, or R3. The latter can be explained e.g., by considering a different type of magnetars than those known in our Galaxy, younger and with stronger magnetic fields (Beloborodov, 2017; Metzger et al., 2017; Margalit et al., 2020b). Moreover, the localisation of some FRBs in older stellar environments (e.g. Xu et al., 2022), with the most notable case of the closest FRB known, pin-pointed to a GC of the nearby galaxy M81 (Bhardwaj et al., 2021b; Kirsten et al., 2022a) are inconsistent with a core-collapse origin for the putative central magnetar. Still, it is theoretically possible to find magnetars also in GCs, born via non-standard, exotic formation channels such as, e.g., the accretion induced collapse (AIC) (Ablimit & Li, 2015; Ye et al., 2019) of a white dwarf (WD). In this scenario a millisecond pulsar, spun up subsequently from the accretion, with a strong magnetic field is supposed to form. Alternatively, the merger induced collapse (MIC) of a WD-WD system, as the latter dominate the centre of GCs (Kremer et al., 2021), is consistent with observations.

Among alternative FRB progenitor models there are those that explain FRB emission, in particular the one presenting periodic repetition, via accretion-based mechanisms onto a central

compact object like a BH or a NS (Waxman, 2017; Sridhar et al., 2021; Deng et al., 2021). In particular, Sridhar et al. (2021) show that FRB luminosities, rates and short durations can be explained by relativistic outflows powered by a compact binary with super-Eddington mass transfer. This type of progenitors are very similar to ultra-luminous X-ray sources (ULXs), i.e. accreting binary systems having X-ray luminosities $L_X \geq 10^{39}$ erg s⁻¹, significantly higher than any X-ray luminosity emitted by stellar processes (see, e.g. Fabbiano & Trinchieri, 1987; Kaaret et al., 2017).

As already described in Section 1.2.2, the short burst duration, combined with the large amount of energy radiatiated out, suggests a compact celestial object as the origin of FRBs, the latter being produced via coherent emission processes in which all the particles emitting the radio waves oscillate together. The emission models proposed for the FRB production are generally of two classes, differentiating whether the emission is supposed to occur near the surface of the NS (close-in models) or at a large distance from it (far-away models) (see, e.g., Lyubarsky, 2021, for a review on FRB emission mechanisms). The former explains the FRB emission as occurring within the NS magnetosphere (Pen & Connor, 2015; Cordes & Wasserman, 2016; Lyutikov et al., 2016; Kumar et al., 2017; Lu & Kumar, 2018; Yang & Zhang, 2018; Kumar & Bošnjak, 2020; Lyubarsky, 2020; Wang et al., 2020). One of the foremost contenders among these models is the coherent curvature radiation model, in which relativistic bunches of charged particles (i.e. electrons and/or positrons), contained in a spatial region of a wavelength size, are accelerated along the curved magnetic field lines (see, e.g., Ghisellini & Locatelli, 2018). The main predictions of this model are the preferred \sim GHz emission band for FRBs and a weak or even absent X/γ -ray counterpart (Ghisellini & Locatelli, 2018). The short duration of FRBs is a strong indication for a close-in emission mechanism. Another example for close-in models explain the FRB emission as originating from magnetic reconnection in the outer magnetosphere during a magnetar flare (e.g. Lyubarsky, 2020). On the other hand, far-away models usually involve the interaction between a magnetized surrounding plasma (at several stellar radii) and a relativistic shock wave generating from the central engine (e.g. a NS or a BH) (Lyubarsky, 2014; Waxman, 2017; Beloborodov, 2017, 2020; Metzger et al., 2019; Margalit et al., 2020a). As the shock wave moves through the magnetized plasma, it can trigger a synchrotron maser instability, where electrons gyrating in the magnetic field emit coherent radio waves (e.g. Metzger et al., 2019). The maser process amplifies the radio emission, leading to the extremely bright bursts observed as FRBs. As already mentioned, the short duration of FRBs seems to indicate an emission origin close to the surface of the central engine, but still one can recover such short durations from shocked "patches" of plasma in the far-away model context.

Interestingly, the narrowness of FRB spectra can be linked to the underlying FRB emission mechanism. Indeed, Kumar et al. (2024b) show that many processes, intrinsic to the emission mechanism or extrinsic to it, i.e. operating between the FRB source and the observer, can contribute to modify the spectrum and make it narrower than it was at the emission time in the rest-frame of the source. Examples of the latter are the plasma lensing phenomenon on radio waves traveling through a refractive plasma (e.g. Cordes et al., 2017), the latter causing high magnification over small bandwidths, multi-path propagation (i.e. scintillation), caused by an inhomogeneous plasma screen between the FRB and the observer. In more detail, the variation of the bandwidth of repeater bursts over time can be used to assess whether the narrowness of its burst spectra is actually due to the plasma lensing effect. Assuming that the lens is located in the strongly magnetised circumburst region, we expect that bursts from repeaters should present a varying bandwidth over time, as the magnetic field configuration in that region is probably very complex (e.g. Michilli et al., 2018). Therefore, if the bursts from a given repeater present steady narrow bandwidths over time, this could be an indication that this feature is intrinsic of the radiation mechanism rather than originating from propagation effects (Kumar et al., 2024b). Moreover, if narrow-band bursts are due to strong magnification plasma lensing, it is possible to show that close-in models are preferred. Indeed, Kumar et al. (2024b) show that far-away models predict bursts with spectra not narrower than $\frac{\nu}{\Delta\nu} \sim 0.6$, as a consequence of high-latitude effects, since the angular size of the source in this case is larger or comparable to the Doppler beaming angle γ^{-1} . Instead, for magnetospheric models, the source angular size is likely much smaller than γ^{-1} .

1.6 FRBs as an independent cosmological probe

Given the extragalactic nature of FRBs, and given the fact that the DM can be exploited as a proxy for the distance of the source (see, e.g., Section 1.2.1), one can employ FRBs to probe some key properties of our Universe on large scales. By localising more and more FRBs, more and more redshifts will be known, mapping the three dimensional distribution of baryonic matter of the Universe. The key observable is the DM of the burst, which encodes, via the dominant contribution of IGM electrons, the integrated amount of ionised matter along the LOS. This quantity, in particular its mean value, is predicted theoretically by the ΛCDM model, which in turn is described by fundamental cosmological parameters. Henceforth, by estimating the DM_{IGM} contribution and by measuring the host redshifts, one can constrain these parameters in an independent way. In this regard, independent probes are fundamental in cosmology to shed light on tensions like the long-standing tension at 4.4σ on the Hubble constant, H_0 , governing the expansion rate of the Universe, between early- (e.g. CMB) and late (e.g. SN Ia) epoch cosmological probes (but see e.g. Abdalla et al., 2022, for a complete review on the topic). One hypothesis is that tensions represent the need for a new physics in the Λ CDM model, or that they suggest the presence of systematic uncertainties not taken into account. To lower the latter one can opt for the combination of different cosmological probes, which are sensitive to the same cosmological parameters (e.g. Gawiser & Silk, 1998; Webster et al., 1998; Bridle et al., 1999; Dark Energy Survey Collaboration, 2018; Pelliciari et al., 2023a). Upcoming instruments should provide $O(10^3)$ FRBs/yr (e.g. Vanderlinde et al., 2019), making it realistic for FRBs to become a competitive probe for the key parameters governing the Λ CDM model independently to both early—and late type cosmological probes. Note that it is not necessary to know what is producing FRBs to exploit them as a cosmological probe. In the following, I briefly describe the ΛCDM, and then I show how FRBs can effectively constrain cosmological parameters.

1.6.1 Constraints on cosmological parameters

The dominant cosmological information is encapsulated in the IGM contribution of the DM of FRBs (see Section 1.2.1). Its mean value towards a redshift z is predicted theoretically in the Λ CDM model, and can be expressed as (Deng & Zhang, 2014; Gao et al., 2014; Zhou et al., 2014):

$$\langle \mathrm{DM}_{\mathrm{IGM}} \rangle(z) = \frac{3c\Omega_b H_0}{8\pi G m_p} \int_0^z \frac{(1+z') f_{\mathrm{IGM}}(z') \chi(z')}{E(z')} \mathrm{d}z' , \qquad (1.24)$$

where

$$\chi(z) = Y_{\rm H} X_{e,\rm H}(z) + \frac{1}{2} Y_p X_{e,\rm He}(z) ,$$

$$E(z) = \left[\Omega_m (1+z)^3 + \Omega_{\Lambda} g(z) + \Omega_k (1+z)^2 \right]^{1/2} ,$$

$$g(z) = \exp \left[3 \int_0^z \frac{1+w(z')}{1+z'} dz' \right] ,$$
(1.25)

and $X_{e,H}$ and $X_{e,He}$ are the fraction of ionized hydrogen (H) and helium (He), respectively, in the IGM, while $Y_H = \frac{3}{4}$ and $Y_p = \frac{1}{4}$ are the mass fraction of H and He. Similarly, f_{IGM} is

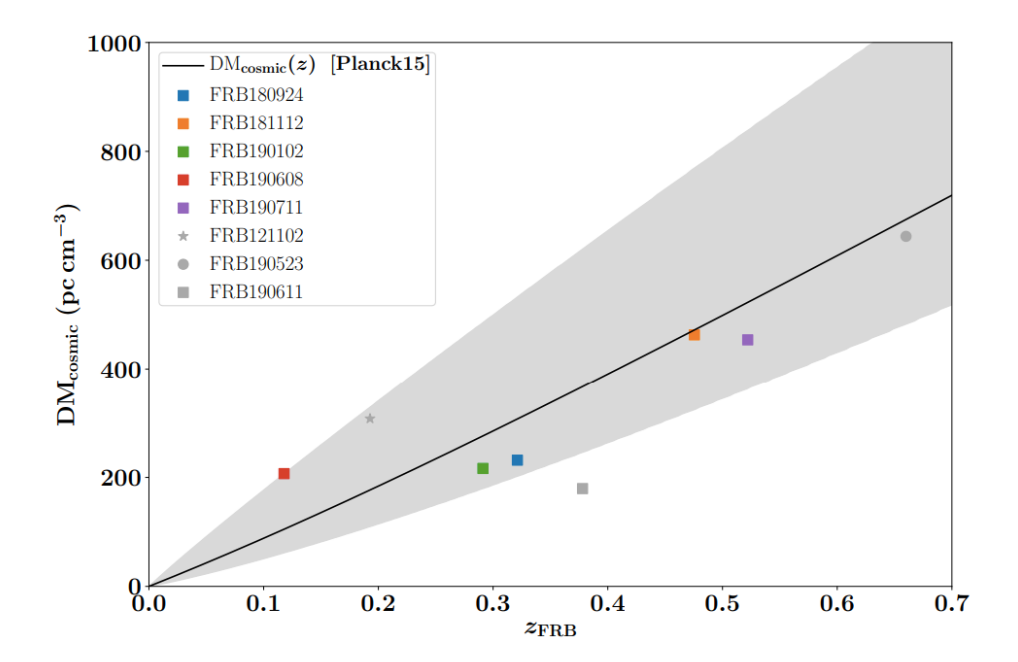


Figure 1.13: The $\mathrm{DM_{cosmic}}$ -redshift relation for a sample of well localised FRBs (coloured squares). Here $\mathrm{DM_{cosmic}}$ represents the IGM contribution to the dispersion measure, obtained after correcting the observed FRB DM for the Galactic DM and host galaxy DM contributions. The black line denotes the expected IGM contribution to the DM as from equation (1.24), considering cosmological parameters from Planck 15 results (Planck Collaboration et al., 2016). The shaded area covers 90% of the $\mathrm{DM_{cosmic}}$ values predicted by a model incorporating ejective feedback in Galactic halos. Credits to Macquart et al. (2020b).

the fraction of baryon mass in the IGM, which is close to $f_{\text{IGM}} = 0.8$ (e.g. Shull et al., 2012). Ω_k denotes the density parameter associated to the Universe curvature, while the dark energy density parameter, Ω_{Λ} , derives from the flat Universe constraint, i.e. $\Omega_{\Lambda} \equiv 1 - \Omega_m - \Omega_k$. The g(z) function encapsulates the variation of the dark energy EoS parameter w, defined as the ratio between the dark energy pressure and energy density. In the standard Λ CDM model, w is fixed to the constant value of -1. However, many cosmological models extends the Λ CDM considering a varying w with redshift, as parametrized by (Chevallier & Polarski, 2001):

$$w(z) = w_0 + w_a \frac{z}{1+z} \ . {1.26}$$

In this fashion, one can constrain cosmological parameters considering a varying w_0 (the model will be w_0 CDM) and a varying w_a (w_0w_a CDM). In the so-called *flat* Λ CDM model, $(w_0, w_a) = (-1, 0)$.

The relationship between DM and redshift is known in the literature as the "Macquart relation", in honour to the astrophysicist Jean-Pierre Macquart, who was the first to actually show that the DMs of known FRBs follow this relation with the redshifts of their host galaxies (Macquart et al., 2020b). Interestingly, the DMs of 5 well-localised FRBs were consistent with the expected $DM_{IGM} - z$ relation from Planck 15 results (Planck Collaboration et al., 2016) (see Figure 1.13). This has been a remarkable result, since it permitted to shed light on the so-called missing baryon problem, i.e. the observed discrepancy between the amount of baryonic matter measured from the cosmological microwave background radiation (CMBR) and Big Bang nucleosynthesis, and from more recent epoch measurements (see, e.g., de Graaff et al., 2019). The latter show a deficit in the amount of baryons by approximately $\sim 30\%$ (Shull et al., 2012). A proposed solution is that the remaining, missing baryons reside in the ionised phase of the

IGM, rather than inside galaxies, especially in the warm and hot ionised medium (WHIM). Since FRBs' DMs are sensitive to the amount of ionised matter along the LOS, the fact that the results of Macquart et al. (2020b) are consistent with theoretical predictions from CMBR + Big Bang nucleosynthesis point towards the confirmation of this hypothesis. In particular, Macquart et al. (2020b) constrained the baryon density parameter to $\Omega_b = 0.051^{+0.021}_{-0.025} h_{70}^{-1}$ at 95% confidence level (C.L.), where h_{70} is the Hubble constant divided by 70 km s⁻¹ Mpc⁻¹, using only localised FRBs.

We can see from equation (1.24) that the mean DM contribution coming from the IGM is not-so sensitive to Ω_m , given the integral over z. This quantity, namely $\langle \mathrm{DM}_{\mathrm{IGM}} \rangle(z)$, instead, depends linearly on the product $\Omega_b H_0$, making FRBs an important independent probe to constrain the value of H_0 . However, given the dependence on their product, $\Omega_b h^2$ and H_0 are totally degenerate parameters. This means that the latter cannot be constrained only by FRB observations. Given this degeneracy, one has to consider the combination of other cosmological probes with FRBs in order to break this degeneracy. For example, Walters et al. (2018) show that one can obtain per-cent precision constraints on $\Omega_b h^2$ when combining them with CMB + SN Ia + baryonic acoustic oscillations (BAOs).

In order to measure the value of $\mathrm{DM_{IGM}}$ one has to accurately estimate the host galaxy and MW DM contributions, which can lead to high uncertainties. Using a sample of nine localized FRBs with known redshifts, Hagstotz et al. (2022) obtained $H_0 = 62.3 \pm 9.1 \; \mathrm{km \; s^{-1} \; Mpc^{-1}}$. A more robust analysis of sixteen localized FRBs and 60 unlocalized FRBs, taking into account important biases such as, e.g. the FRB luminosity function, the telescope beamshape and the host DM contributions led to $H_0 = 73^{+12}_{-8} \; \mathrm{km \; s^{-1} \; Mpc^{-1}}$ (James et al., 2022a). Regarding the dark energy EoS, Zhang et al. (2023b) show that only for 10^6 localized FRBs it will be possible to reach a per-cent uncertainty level on the EoS w parameter, using FRBs alone.

1.6.2 Other relevant constraints

Other than offer constraints to cosmological parameters, FRBs are already used (as for the case of the missing baryon problem) to investigate more astrophysical-related aspects, such as the distribution of matter in the halos around galaxies, or to probe large-scale magnetic fields and turbulence.

Turbulence and large-scale magnetic fields. Starting from the turbulence, in this case the key observable is the scattering tail seen in many FRBs (see Section 1.2.2), indicative of a multi-path propagation in an inhomogeneous plasma. Hence, FRBs are sensitive to turbulence on scales that can be as large as the IGM scale, the largest in our Universe. It has been observed that FRBs are much less scattered, by approximately one order of magnitude, than pulsars (Cordes et al., 2016), indicating that the IGM has minor turbulence impact than the ISM. It is still under debate whether the observed temporal smearing of FRBs is caused mainly by the IGM or by the ISM of the MW and host galaxy of the source. Interestingly, the temporal smearing due to the host galaxy and the one caused by the propagation within the IGM have very different expected dependence on the redshift (Macquart & Koay, 2013), with the contribution from the host decreasing steeply with increasing redshift. Up to now, no evidence for such relationship has been found for a sample of localized FRBs (e.g. Qiu et al., 2020; Cordes et al., 2016), although the statistics considered is still poor and, many times, the time resolution adopted for FRB observation is too wide to probe (expected) scattering times.

The joint information on DM and RM from the same FRB observation can also lead to important constraints regarding the large-scale magnetic fields permeating the Universe (e.g. Piro & Gaensler, 2018). The origin of such large-scale magnetism, along with its impact on

galaxy formation is nowadays largely unknown and usually is treated theoretically (e.g. Springel, 2010; Rodrigues et al., 2019). By measuring both the DM and RM of an FRB, one can have a proxy for the integrated magnetic field strength parallel to the LOS (e.g. Lorimer & Kramer, 2004):

$$\langle B_{\parallel} \rangle \equiv \frac{\int_0^d n_e B_{\parallel} dl}{\int_0^d n_e dl} = 1.23 \ \mu G \left(\frac{\text{RM}}{\text{rad m}^{-2}} \right) \left(\frac{\text{DM}}{\text{pc cm}^{-3}} \right)^{-1} . \tag{1.27}$$

One has to keep in mind that this is only an averaged value for B_{\parallel} , hence in a situation in which the latter changes sign repeatedly along the LOS the value obtained from equation (1.27) will represent a poor reflection of the true, underlying magnetic field. Interestingly, RM variations with time of repeating FRBs can lead to important clues on the local magnetic field configuration at the source site (Yang et al., 2023).

Already some constraints from single FRBs have been presented in the literature. For instance, Masui et al. (2015) show that the measured RM = -186 ± 14 rad m⁻² observed from FRB 20110523A implies $\langle B_{\parallel} \rangle \sim 0.38~\mu\text{G}$. As for the potential in becoming a precise cosmological probe, $> 10^3$ FRBs with precisely measured RMs are required to distinguish between models for the IGM magnetic field seed (Akahori et al., 2016; Vazza et al., 2018).

Reionisation history of the Universe. Remarkably, the measure of the maximum DM in the FRB population can help shed light on the reionisation history of the Universe. Small primordial fluctuations in the global matter density field lead to temperature fluctuations $(\Delta T \sim 10^{-5} \text{ K})$ in the CMBR at $z \sim 1100$. The latter grow through gravitational interaction, resulting in dark matter halos. Within these halos, baryonic matter (gas) subsequently accretes, cools, and collapses into the first compact, luminous objects. The period from the CMBR (i.e. recombination) to the formation of the first luminous objects is called the Dark Ages, about which we know nothing due to the lack of direct observations. The formation of the first luminous sources changes the nature of the IGM, heating and reionizing it. Before this, the IGM was completely neutral, whereas it was fully ionized before recombination. This formation period is commonly known as the Cosmic Dawn. From this, the Universe starts to be ionised again, in a period called reionisation. Measurements of the Gunn-Peterson effect 10 and the optical depth parameter of the CMB indicate that reionization ends at a redshift of $z \sim 7$, while the formation of the first luminous sources is thought to occur between $z \sim 25$ –30. Beniamini et al. (2021) show that the maximum DM measured from a population of 1000 FRBs having DM > 6000 pc cm⁻³, can characterise the reionisation history of the Universe better than the current measurements from CMBR optical depth (Pagano et al., 2020). A smaller sample of FRBs, 100 localized FRBs, originating from redshifts 5 < z < 15, could constrain (at 68% C.L.) the CMB optical depth to within 11%, and the midpoint of reionization to 4%, surpassing current state-of-the-art CMB bounds and quasar limits (Heimersheim et al., 2022).

Fundamental physics. Lastly, the dispersive nature of FRBs can be used to place constraints on fundamental physics. Indeed, additional contributions to the ν^{-2} behaviour expected from dispersion in a cold plasma (see Section 1.2.1) could arise from a non-zero rest mass of photons (Bonetti et al., 2016; Xing et al., 2019; Lin et al., 2023; Ran et al., 2024), and/or the violations of the Einstein Equivalence Principle (Wei et al., 2015; Tingay & Kaplan, 2016; Zhang, 2016; Xing et al., 2019). A violation of the latter would imply that photons of different energies fall at different rates when traversing gravitational potentials. Instead, a non-zero photon mass would result in a dispersion relationship in pulse propagation as a function of

 $^{^{10}}$ The Gunn-Peterson effect is the complete absorption in the spectra of distant quasars caused by neutral hydrogen in the intergalactic medium.

frequency. The absence of such a delay provides a direct constraint on the photon mass. Up to now, the most stringent constraint on the rest mass of the photon is provided in Ran et al. (2024), who obtained $m_{\gamma} < 3.5 \times 10^{-51}$ kg analysing the bursts of localized FRBs employing a machine learning, cosmology-independent model. Regarding the Einstein Equivalence Principle, Xing et al. (2019) constrained equivalence principle violations to nearly one part in 10^{16} by analyzing the time delay between downward drifting pulses of R1.

Chapter 2

Observing FRBs with the Northern Cross radio telescope

In this Chapter, I summarize the ongoing effort to transform the Northern Cross (NC) radio telescope into an instrument for FRB surveys, operating at 408 MHz. Since the start of the Northern Cross Fast Radio Burst (NC-FRB) project, back in 2018, scientific results have been published in refereed journals (Locatelli et al., 2020; Trudu et al., 2022; Pelliciari et al., 2023b, 2024a). Ongoing efforts on both the instrument development and scientific research fronts aim to further advance the capabilities and scientific reach of the project. At the start of my Ph. D. (1th Nov. 2021), the working number of receiving cylinders was six (see Section 2.1 for details), while at the time of writing we exploit 16 cylinders for daily FRB observations. A timeline history regarding the status of the NC-FRB project is shown in Figure 2.1 Moreover, at the beginning of my Ph.D., the scheduling of multi-target observations was difficult due to hard-coded scripts. Therefore, I focused on this aspect and worked on developing codes (written in Python and Bash) that enabled easy scheduling of multi-target observation campaigns, which are used daily within the NC-FRB project for observations. This Chapter is outlined as follows. In Section 2.1 I briefly describe the NC radio telescope as a searching FRB instrument, providing also some of its historical remarks. In Section 2.1.1 I present the NC-FRB project, while in Section 2.2 I describe how FRB observations are conducted within the NC-FRB project, with particular interest on the pipelines developed during my Ph. D. aimed at facilitating both the observation scheduling and the FRB candidate selection.

2.1 The Northern Cross

The NC (Croce del Nord, in italian) is a T-shaped radio interferometer operating at 408 MHz, located at the Medicina Radio Astronomical Station near Bologna, Italy (Figure 2.2). Its arms are oriented in the North-South (N-S) and East-West (E-W) directions. It is a transit radio telescope, that can be steered only in the declination direction, allowing to observe only sources that are culminating at the local celestial meridian. Historically, the NC has been used for sky surveys, generating numerous catalogs of extragalactic radio sources. In particular, just after 6 years from the first light, a catalogue of 3235 extragalactic radio sources down to a flux completeness of 0.2 Jy was published (Colla et al., 1970), called B2.1 catalogue, with a flux limit at least five times lower than that of the major catalogues available at the time. Over the next three years, systematic observations continued, resulting in the publication of the B2.2 (Colla et al., 1972) and B2.3 (Colla et al., 1973) catalogues, both complete down to 0.25 Jy, and the B2.4 catalogue (Fanti et al., 1974), complete down to 0.6 Jy. Collectively, the B2 catalogues included 9923 radio sources, achieving significant recognition with approximately 600 citations. As an example of the significant impact of the B2 catalogue, it is worth noting that by analyzing

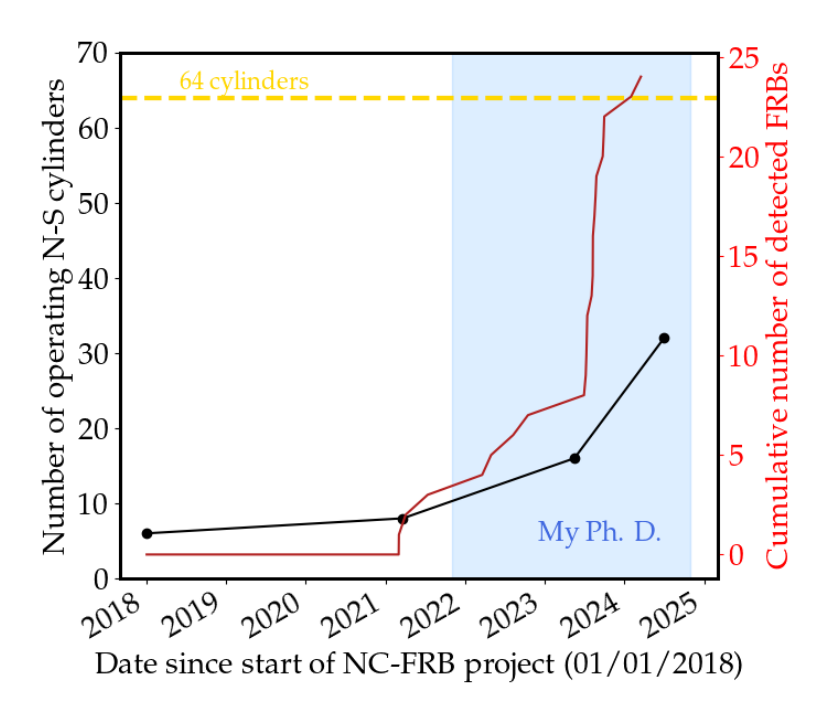


Figure 2.1: Status and performance of the first 6 years of the NC-FRB project. The red axis refers to single FRB bursts, not different sources. Indeed, the red curve is dominated by the multiple detections on FRB 20220912A, a single hyperactive repeater (see Chapter 4). The steep rise of the red curve is also a consequence of the change to 16 operating cylinders. The shaded blue bar represents the time during my Ph. D.



Figure 2.2: The Medicina Radio Astronomical Station located at Medicina, near Bologna, Italy. Visible in the picture are the NC antennas and the Medicina "Grueff" single dish to the right side. Credits to Locatelli et al. (2020).

Table 2.1: Characteristics of the current NC observational system. These parameters refer to a system composed only by the N–S arm. The last three parameters describe the acquisition system used when used to form a single beam.

N. of working receiving cylinders	16
N. of analog receivers per cylinder	4
N. of frequency channels	1024
Channel width	$14.4~\mathrm{kHz}$
Central frequency	$408~\mathrm{MHz}$
Analogue bandwidth	$16 \mathrm{\ MHz}$
Single receiver field-of-view	$38 \mathrm{deg^2}$
Time resolution	$138.24 \ \mu s$
N. bits	16
N. coarse channels	21
Throughput	$311.11~{\rm Mb~s^{-1}}$

the number of radio sources as a function of flux density (the logN – logS relation), important evidence was provided supporting the idea that the Universe evolved according to the "Big Bang" model. Although this was already established with the discovery of the CMBR (Penzias & Wilson, 1965), the results from the B2 catalogue offered further confirmation of this theory (Colla et al., 1972). In 1985, a new survey utilizing the N–S arm led to the publication of the B3 catalogue (Ficarra et al., 1985). This comprehensive catalogue listed 13354 radio sources, complete down to 0.1 Jy, covering an area between declinations +37°15′ and +47°37′. Finally, in the early 1990s, a specialized system was developed and implemented for observing millisecond and sub-millisecond pulsars using the E–W arm (D'Amico et al., 1996). This system enabled the observation of a sample of radio pulsars in coordination with the Compton Gamma-Ray Observatory mission (Gehrels et al., 1994) from 1991 to 1995. Through the analysis of the pulse profiles, the values of the period, period derivative, and position of 55 pulsars were determined.

The N–S arm features 64 reflective cylinders, each measuring 7.5 × 23.5 m, and focusing incoming radiation onto 64 dipoles along the focal line. The effective collecting area of the instrument is approximately 8000 m², when considering an antenna efficiency of 0.71 (Bolli et al., 2008). The work of Locatelli et al. (2020) describes how the focal line of sixteen cylinders has been modified to group the signals from sixteen dipoles, providing four analog signals per cylinder and 64 receiving inputs for the upgraded section. All the principal properties of the receiving system used for current observations are summarised in Table 2.1. These inputs are connected to a front-end, which is mounted on the focal line, hosting low noise amplifiers and optical fiber transmitters (Perini, 2009). Since 2021 March 21th, from six employed cylinders, the NC transitioned to eight cylinders (Trudu et al., 2022). From 2023 May 17th (Pelliciari et al., 2024a) the available cylinders changed to 16, for a total of 64 receiving signals. In the near future both the NC arms will be operative for FRB science, but at the writing of this Thesis, only part of the NS arm is ready.

2.1.1 The NC-FRB project

Despite the receiving system still being under refurbishment and commissioning, the NC-FRB project has already made significant progress in advancing its observational capabilities and scientific contributions in studying FRBs. Before my involvement, the project had already achieved considerable milestones, particularly highlighted in the works of Locatelli et al. (2020) and Trudu et al. (2022).

Locatelli et al. (2020) detailed the early stages of equipping the NC radio telescope for FRB surveys at 408 MHz. In this work the receiving system is described in details, along with the first system validation via the successful observation of the bright radio pulsar B0329+54. Moreover, the potential of the NC in being a blind FRB survey is described, showing how its wide field-of-view (~350 deg² exploiting all the 64 N–S cylinders, and forming 20 independent beams, Locatelli et al., 2020) will be exploited for constraining the all-sky FRB-rate as well as the slope of the FRB energy distribution.

Trudu et al. (2022) presented the first successful detections of FRBs using the NC radio telescope, following an extensive 19-month observational campaign targeting four repeating FRBs: FRB 20180916B, FRB 20181030A, FRB 20200120E, and FRB 20201124A. During this period, the system was upgraded from six to eight cylinders, improving the sensitivity and detection capabilities. Before the upgrade, a single burst from FRB 20180916B was detected with a fluence threshold of 51 Jy ms. After the upgrade, two additional bursts from the same source were observed, with a lower fluence threshold of 38 Jy ms, confirming the source's periodicity within its 5.2-day activity window. The observed burst rate was consistent with the expected rate based on CHIME/FRB data (Chime/Frb Collaboration et al., 2020). No detections were made for the other three FRBs, but the study provided constraints on the slope of the differential fluence distribution for FRB 20181030A and FRB 20200120E, suggesting steep slopes.

Two additional NC-FRB projects are presented in Chapter 3, based on Pelliciari et al. (2023b), and Chapter 4, based on Pelliciari et al. (2024a).

Moreover, NC observations also played a crucial role in multi-wavelength observational campaigns. For instance, Pilia et al. (2020) utilized the telescope as part of a multi-wavelength monitoring on R3, while Bailes et al. (2021) considered NC data for a multi-wavelength campaign on the Galactic magnetar SGR 1935.

2.2 FRB observations

In the following I describe the entire chain between data acquisition within the NC-FRB project, and the final FRB candidate validation.

2.2.1 Data acquisition

The radio signals are transmitted to the station building via analog optical fiber links. The RF receiver manages optical-electrical conversion, filtering, amplification, conditioning, and single down-conversion to an intermediate frequency (IF) of 30 MHz, with output power digitally attenuated in steps up to 31.5 dB. A splitter chain distributes local oscillator, clock, and synchronization signals to the IF circuitry.

Digital acquisition and signal processing are handled by the Analog Digital Unit (ADU) board, a digital platform developed for the Low Frequency Aperture Array (LFAA) component of the Square Kilometre Array (SKA). The ADU includes sixteen dual-input Analog to Digital Converters (ADCs) and two Field Programmable Gate Array (FPGA) devices, digitizing and processing broadband RF streams from up to 32 single polarization antennas at an 800 MHz sampling rate. Time-stamped samples are synchronized to coordinated universal time (UTC), with signal processing performed on the FPGAs. The modular firmware design incorporates interfaces to physical peripherals and control structures, while the signal processing core manages tasks like cable mismatch correction, channelization, delay correction, and frequency domain beamforming. This setup allows the generation of a single beam¹ with a minimum integration

¹At the writing of this Thesis we form only a single beam. However, in the near future it will be possible to

time of about at 1.08 microseconds integration time and a frequency resolution of 781 kHz. The latter case is used for current FRB observations and, indeed, throughout the analyses reported in this Thesis we formed only one beam in the sky. We then apply a downsampling in order to have a 138.24 μ s sampling time and a 14.4 kHz frequency resolution, chosen to reduce the intrachannel smearing for high DM events (Trudu et al., 2022).

Data streams, transmitted over a 40 Gb link using a custom SPEAD protocol, are received by a compute server capable of processing different simultaneous data streams. These streams are stored using a simple binary format for calibration and monitoring purposes, and the frequency channels of interest are saved using a modified SigProc Filterbank format, enabling efficient real-time data writing and conversion.

In addition to the primary observations conducted with the NC radio telescope, my Ph. D. work also involved the enabling of the Medicina "Grueff" single dish radio telescope (Mc radio telescope, hereafter) for the study of FRBs and pulsars. I managed the installation and testing of FRB-BASEBAND², a public pipeline designed to convert baseband VDIF data (i.e. raw voltages) from single-dish radio telescopes into channelized filterbank files. This development was crucial in enabling the detection of fast transients using this telescope. Although we have not yet achieved a confirmed detection of an FRB with the Mc radio telescope, we have successfully detected single pulses from the pulsar B0329+54 (see Figure 2.3) and we conducted an extensive observational campaign utilizing both telescopes on an active repeater (refer to Chapter 4). This collaborative effort between the two facilities has provided valuable insights into the characterisation of both spectral and energetic properties of this source.

2.2.2 Calibrations

To calibrate the receiving system of the Northern Cross and enable observations of fast transients, we describe the calibration tests usually conducted before actual observations. These tests are extensively detailed in Locatelli et al. (2020), but we will provide a summary here.

The calibration procedure follows the standard method used in interferometric observations. The complex voltages of each pair of receivers are cross-correlated to form complex visibilities:

$$V_{ij} = \langle v_i(t)v_j(t)^* \rangle_{\Delta t} , \qquad (2.1)$$

where $\langle \rangle_{\Delta t}$ represents the average over an integration time Δt , while the * operator represents the complex conjugation operation. The visibilities in Eq. (2.1) are ideal, while the instrument records visibilities corrupted by the response of the receivers. These recorded visibilities, referred to as observed visibilities, are related to the ideal ones through the so-called complex gains g:

$$V_{ij}^{o}(t,\nu) = g_i(t,\nu)g_j(t,\nu)^*V_{ij} . {2.2}$$

The purpose of the calibration procedure is to determine the gains g, which can be obtained once the ideal visibilities are known. This is achieved by observing sources, known as calibrators, whose properties are well established.

As described in Locatelli et al. (2020); Trudu et al. (2022), we use two bright radio sources, i.e. Taurus A (Tau A) and Virgo A (Vir A) as calibrators for our purposes. We steer the telescope towards the declination of each source, performing a standard on-off observation. In the latter, we estimate the background noise contribution and we subtract it from the observed power when the sources are within an hour angle $-2^{\circ} \leq \varphi \leq +2^{\circ}$. For each source, we fit a Gaussian function to the profile full width at half-maximum (FWHM) for 21 frequency channels

form multiple beams inside the field-of-view of the NC radio telescope, permitting to increase the localisation capability of the telescope.

²https://github.com/pharaofranz/frb-baseband

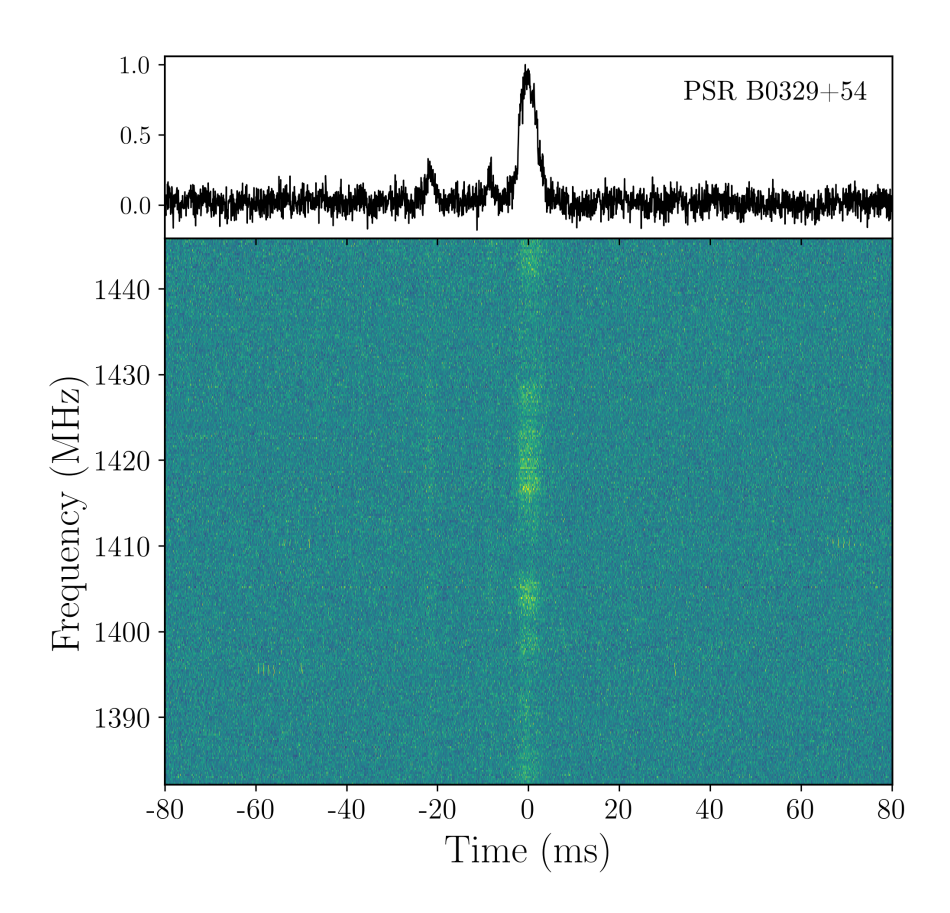


Figure 2.3: Single pulse detection of PSR B0329+54 with the Mc radio telescope at 1.4 GHz. The main panel shows the dynamic spectrum, incoherently de-dispersed at DM = 26.7641 pc cm⁻³ (as reported in Manchester et al., 2005), while the top panel shows the frequency-averaged time series. The estimated S/N of the burst is \sim 33. Evident in the dynamic spectrum is the main pulse of the pulsar, preceded by two narrower and fainter sub-pulses.

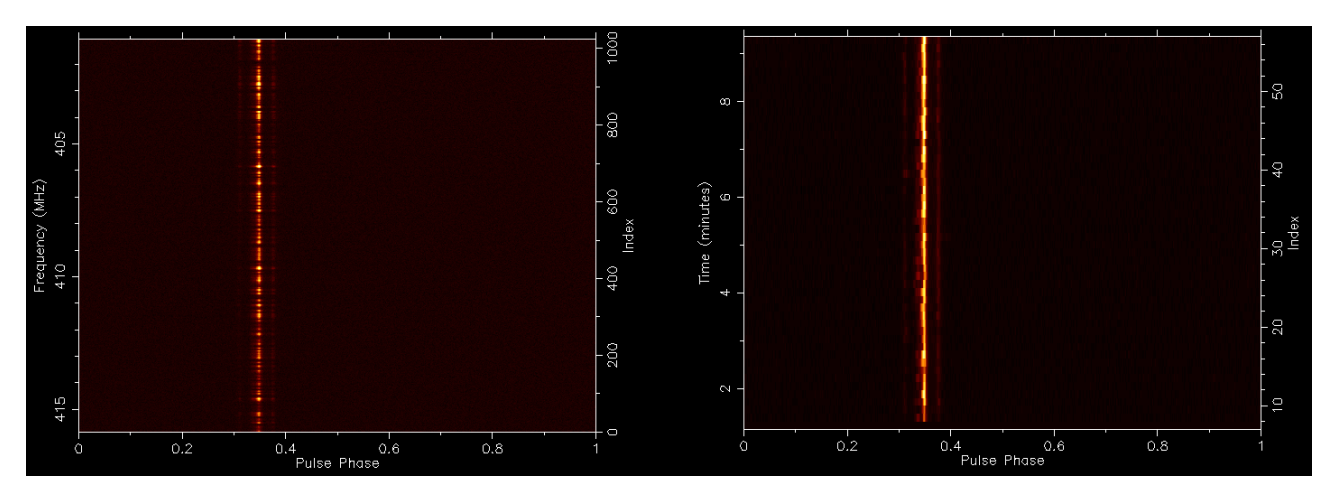


Figure 2.4: Observed profile of the bright pulsar PSR B0329+54 at 408 MHz with the NC radio telescope. Left: intensity profile as a function of the rotational phase and frequency channels, integrated over 10 s. Right: intensity profile as a function of the rotational phase and single-pulse time ($\sim 700 \text{ ms}$) over the 16 MHz bandwidth.

equally spaced across the NC bandwidth. We estimated the conversion between counts and Jy for each channel from the best fit amplitudes and assuming a flux density for each source following Perley & Butler (2017). The assumed values for the flux density of calibrators are 1078 Jy and 569 Jy for Tau A and Vir A, respectively (Perley & Butler, 2017).

Finally, we estimate the instrument SEFD from each source by solving the radiometer Eq. (1.15), solving for SEFD = $T_{\rm sys}/G$. The resulting SEFDs, averaged over the NC bandwidth, are 9000 ± 400 Jy and 7800 ± 180 Jy for Tau A and Vir A, respectively. We note a $\sim 20\%$ variation across the bandwidth for all the considered calibrators. Moreover, the SEFD depends slightly on the Galactic latitude, qualitatively expected as the sky temperature contribution to the SEFD increases towards the Galactic plane. We then consider a unique value of SEFD = 8400 ± 420 Jy, obtained by averaging the SEFDs from the individual calibrators. This analysis has been included in Trudu et al. (2022).

After each calibration run, we validate the calibration procedure by forming a beam centred on the bright pulsar B0329+54 and producing a folding plot like the one reported in Figure 2.4, considering the nominal parameters of the pulsar, i.e. its period and DM. Moreover, we also check if the single-pulse detection pipeline (see Section 2.2.4) works fine by analysing B0329+54 data, searching for its single-pulses. Possibly, we include also data from the Crab pulsar (B0531+21), which can be considered a much more similar case to FRB detections since it is known to emit GRPs (e.g. Karuppusamy et al., 2010).

2.2.3 Scheduling observations

Setting observation schedules. The first step in scheduling transient observations is the preparation of observation folders. These folders will serve the scheduling script to gather all necessary information for scheduling observations. To create these folders, a simple MATLAB script called NCFRB_PrepareObs.m can be used. This script is user-friendly and allows the creation of observation folders by setting a few parameters:

• The name of the source to be observed (SourceName). This name must correspond to the name of the source specified in an external source catalog, which is another MATLAB script called MINT_J2000SourceCoordinate.m. In case the planned observations will regard a new target source, the user must add it to the MINT_J2000SourceCoordinate.m catalog, specifying the source name and its RA and Dec coordinates at the J2000 epoch.;

- The start (startDateUT) and end (stopDateUT) dates of observation. For an observational campaign of N days, N observation folders will be created;
- The array configuration used (arrayConf). For this parameter, it is necessary to specify whether the observations are to be made with the sub-array 1N, 2N, where 8 cylinders will be used in these two cases, or 1N2N, using 16 cylinders in the latter case;
- The type of observations to be performed (obsType). The possible options are "Tracking," if an observation folder is to be created in beamforming mode, or "Calibration" if a folder is to be created for interferometric observation, the latter used for instrument calibration procedures;
- Output path (outPath) where the observation folders will be created;
- Path pointing to previously performed calibrations (calibPath).

The output of PrepareObs.m script is an observation directory, placed at outPath, having name YYYYMMDDThhmmss_SourceName_arrayConf. This directory contains 5 files. The most relevant for our activity is obs_setup.txt, containing all the information used in the effective observation scheduling. Among the latter there are the RA, Dec coordinates of the source and the precise start and stop times for the observation.

Scheduling beamforming observations. Once the observation folders have been created, the scheduling of observations can proceed. During my Ph.D., I developed the Python script scheduler.py, which facilitates user-friendly scheduling of multi-source observational campaigns. Before the creation of this script, scheduling observational campaigns was highly cumbersome and complex. The scheduling of each individual observation essentially comprises three parts: the mechanical movement of the NC antennas (managed by the bash executable monitor), the beam-tracking of the source (beam_tracking_scheduler_mat2py.py), and the actual data acquisition (best_frb_scheduler.py). Therefore, each of these actions requires a different script.

The monitor application only needs a single text file containing a list of schedules. These schedules are formatted as follows:

```
ANT; UTC; YYYY-MM-DDThh: mm; arrayConf; decSource_deg; SourceName;
ANT; UTC; YYYY-MM-DDThh: mm; arrayConf; decSource_deg2; SourceName2;
...
```

where decSource_deg is the declination (J2000) of the source to be observed, expressed in degrees unit. The other two scripts, however, must be launched individually for each observation, with the inputs specified manually. For example, for the acquisition script bestfrb_scheduler.py, these inputs include the path of the observation folder (i.e., outPath from NCFRB_PrepareObs.m), a string representing the start time of the observation, the duration of the observation in seconds, and the instrument configuration file. Clearly, in the case of multi-source observational campaigns, such a scheduling procedure is infeasible if done manually.

Therefore, as mentioned earlier, the **scheduler.py** script was implemented. The help screen of this script is as follows:

```
Usage: scheduler.py [options]

NCFRB scheduler. You have to provide the start and stop date of observations, along with an external list of sources.

Options:
```

```
-h, --help
                           show this help message and exit
    --nameSRC=NAME
                           Source name you want to monitor.
9
    --cadence=TCAD
                           Cadence of your monitor. Example: 7 if you want to
                           monitor your source every 7 days. (Default: 1 i.e.
11
                           every day
12
                           Start of observations. Example format: 20220606.
    --start=START
13
    --stop=STOP
                           Stop of observations. Example format: 20220608.
14
                           The full path to the obs. directories (Default:
    --obs_dir=OBS_DIR
15
                           /jbod/SCHEDULE_OBS/).
16
                           The path where the output schedule file will be
    --ant_move=OUTPATH
17
                           stored. (Default: /jbod/ant_scheduler/schedule.csv)
18
    --path_schedules=SCHEDULES
19
                           The path where the schedules for acquisition and
20
                           steering (+screenlog) will be stored. (Default:
21
                           /jbod/ant_scheduler/)
22
                           Clean the schedules (default: False)
    --clean=CLEAN
23
                           Go launch the schedules (default: False)
    --go=GO
```

Listing 2.1: Descriptive help message for the scheduler.py script used within the NC FRB project to schedule osbservational campaigns

The important input parameters to set, as indicated in the header of the help message, include the source name, the start date, and the stop date of the observations. Additionally, the script allows setting a temporal cadence for a given source. This is particularly useful in cases where two sources transit the meridian at similar times but have very different declinations. Consequently, both sources cannot be observed on the same day by the NC. By setting the **cadence** parameter, it becomes possible to schedule these two sources on alternate days automatically.

Basically, what this script does is update the schedule file (located at the path specified by the input ant_move). Before starting with the effective scheduling, the user may want to clean the previous schedule file by setting clean to True. The user is required to set the parameter go to True in correspondence with the last schedule entry. This way, the script will display the final content of the schedule file on the screen and, upon user confirmation, it will proceed to automatically launch the tracking and acquisition scripts for each observation. As the final step, the script automatically launches the antenna movement script. All these scripts are executed in screen mode, allowing the user to close the terminal once scheduler.py is executed. Additionally, we have verified that memory usage is not an issue for the Medicina server (i.e. where all the scripts for scheduling, etc., are installed), even when dealing with a long list of scheduled observations. The scheduler.py was used extensively to prepare all the observations presented in Chapter 3 and Chapter 4, as well as for current, daily NC observations which are not part of this Thesis. Usually, all the observation folders are stored at the path /jbod/SCHEDULE_OBS/ while the output of scheduler.py, i.e. the observation folder with the correspondent un-processed or processed SigProc Filterbank file inside it, are stored at /jbod/PROC/ path. This is done in order to facilitate the analysis and FRB search pipeline, having all the processed observations at a single path.

2.2.4 Data reduction and FRB searching

The processing of raw voltages in SigProc Filterbank format is carried out using the script best_frb_post_processor.py, which is directly linked to the output of scheduler.py. The latter controls a simple external catalog where the name of the sources to be scheduled for observations are stored, along with their coordinates and, importantly, a Boolean variable that determines whether the raw Filterbank output should be processed after acquisition. Indeed, it is unsafe to process a Filterbank while acquiring data from a subsequent source, given the fact that both the acquisition and the processing are handled by the same machine. Therefore, the

user can choose whether to process the raw voltage outputs in Filterbank format or to keep it in a raw format for a later post-processing.

The processing script reads the beamformed complex voltages, which are already channelized but with a very coarse frequency resolution. Therefore, further channelization is performed by executing a simple Fast Fourier Transform (FFT) with a window in this case. The edge channels are removed. Subsequently, the power for each sample is calculated (thus the data are no longer in complex format), and normalization is performed so that the statistical mean of the data is zero and the variance is unitary. Finally, an output Filterbank is generated with the data stored in 16-bit format.

Once the data has been processed, it is possible to search for radio bursts within it. To do this, we use a pipeline that executes various steps and combines softwares that have been used and tested in the literature for FRB search, i.e. HEIMDALL (Barsdell et al., 2012) and classification (Gajjar et al., 2018; Agarwal et al., 2019). We describe the steps performed by the FRB search pipeline, along with a brief general description of the single steps, in the following.

Excision of spurious artificial signals. Although the 400-416 MHz band used by NC is designated solely for astronomical observations, various artificial radio signals (RFI) can still occur, which pose a challenge when trying to detect very faint extragalactic signals. Broadly speaking, RFIs can be either persistent channels or impulsive, very short-duration signals (e.g., radar). Persistent RFIs are usually persistent during the observation session and can be flagged by applying a static mask. Impulsive RFIs can be ignored during the subsequent candidate classification phase. Essentially, these RFIs, being produced on Earth, do not undergo any dispersion and can be easily identified. In our case, we apply offline RFI mitigation using the PRESTO software, specifically rfifind.

Dedispersion and candidate search. As described in the previous chapter, signals from FRBs exhibit high DM due to the crossing through cold plasma between the source and the observer. Since these signals are weak in the data, dedispersion is required, to produce a peak in the frequency-averaged signal (called a time series), making it easier to recognize. The dedispersed signal will be stronger the closer the applied DM is to the intrinsic value of the burst. There are essentially two types of dedispersion algorithms: the "incoherent" method, which is approximate, and the "coherent" method, which is exact. In our case, we usually apply the former, which involves searching for the DM (initially unknown) over a wide range of values. This process is carried out using the HEIMDALL GPU-accelerated tool, which also applies the Matched Filtering method to search for radio pulses (the reader can refer to Rajwade & van Leeuwen (2024) for a complete and comprehensive review of de-dispersion algorithms). The output of HEIMDALL is a list of candidates, providing the arrival time in seconds from the start of the observation, the DM that maximizes the candidate's S/N, the S/N, and the pulse duration (expressed in boxcars). Optionally, if the user specifies a DM as input to frb_post_processor.py, coherent dedispersion of the data is performed. The latter involves the exact reversal of the dispersion effect caused by the interstellar medium on the pulsar/FRB signals. This is achieved by applying a frequency-dependent phase shift to the received signal, preserving the original signal phase information and resulting in a much sharper and more accurate pulse profile, with no intrachannel smearing. This method is computationally intensive but provides superior time resolution compared to "incoherent" de-dispersion. When running the pipeline for FRB candidate search, we typically specify an S/N threshold below which candidates are discarded. In our observations, this threshold is set at 7σ or 10σ , where σ is the rms noise derived from the radiometer equation (Eq. 1.15). The exact choice for it depends principally on the level of RFI contamination, so that a lower threshold will give more false candidates in output.

Candidate Classification. Existing pipelines for single-pulse searches produce hundreds, if not thousands, of candidates per observation session, even when clustering and sifting methods are applied during candidate searches. Most of these candidates turn out to be "false positives", i.e., RFI signals erroneously reported as real radio bursts. Therefore, it is necessary to use methods for classifying the candidates output. During my Ph.D., I used two main algorithms specifically designed for the classification and recognition of real FRB candidates. These are Machine Learning (ML) tools, exploiting convolutional neural network (CNN) architectures, trained over extensive datasets from several radio telescopes and bandwidths (Gajjar et al., 2018; Agarwal et al., 2020). Currently installed and operational on the Northern Cross server, used for data analysis, are the SPANDAK (Gajjar et al., 2018, 2021, 2022), and the FETCH pipelines (Agarwal et al., 2020). The latter takes the candidates produced by HEIMDALL as input, screens out false positives that appear over a wide range of DM in a short time interval, generates plots for each candidate that passes the selection steps, and finally classifies these candidates using a CNN architecture. Specifically, this algorithm is very simple, aiming to detect a feature resembling a vertical line (i.e., the dedispersed burst) in a 2D image. For each candidate, the ML model considers two inputs, i.e. the 2D dynamical spectrum and the corresponding butterfly plot. Candidates are then classified into three different classes, ranking them from highest to lowest based on their probability of being a genuine astrophysical burst. An example of the output of the classification pipeline is provided in Figure 2.5. Finally, the ultimate validation of the candidate is performed manually through visual inspection. It is also useful to re-plot the candidate using a different number of sub-bands and applying further temporal down-sampling, trying to increase the S/N per channel as much as possible.

2.3 Conclusions

In this Chapter, we presented the NC-FRB project, detailing the transformation of the NC radio telescope into an instrument for FRB detection at 408 MHz. Since the project start in 2018, approximately, the NC has undergone a series of upgrades aimed at increasing its sensitivity and expanding its operational capacity. Throughout this Chapter, we have emphasized the technical advancements made to streamline observations, from the development of efficient scheduling systems to the implementation of a robust data reduction pipeline. These improvements have enhanced daily FRB observations and increased the system reliability, as seen in the accurate classification of FRB candidates using machine learning algorithms. In conclusion, the NC-FRB project has reached a pivotal stage in its development. The significant upgrades to the receiving system and the successful detection of FRBs during observational campaigns underscore the project's scientific impact. While further improvements are still needed – such as the full reactivation of both arms of the telescope – the NC is already contributing valuable data to the field of FRB research. Looking ahead, the planned upgrades will not only increase the telescope's sensitivity and detection rate but also improve its localization accuracy, enabling more detailed studies of FRB sources and their environments. This will place the NC in a position to address key scientific questions about the nature and origin of these enigmatic cosmic events, solidifying its role as a crucial instrument in the study of FRBs.

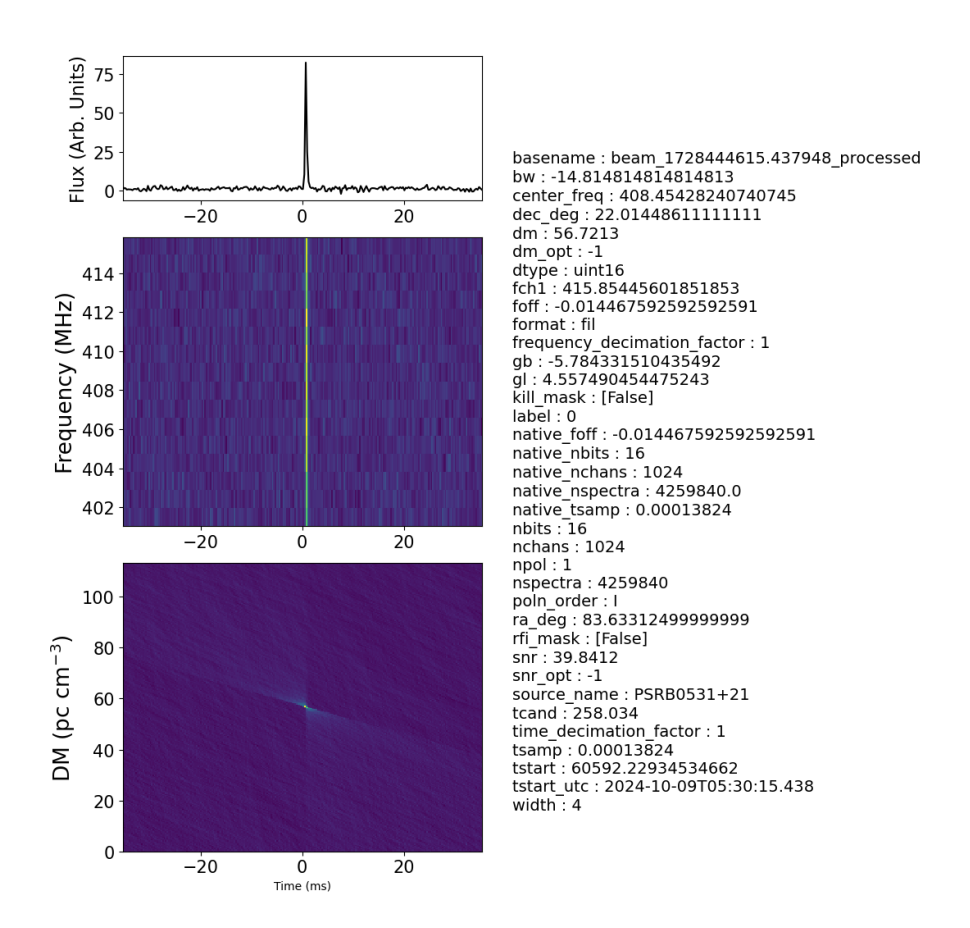


Figure 2.5: Example of a candidate as the final output of the single-pulse detection pipeline used within the NC-FRB project. Here is reported a single pulse NC detection of the Crab pulsar (B0531+21). The upper subpanel shows the frequency-averaged time series of the pulse, the central subpanel shows the dynamic spectrum, de-dispersed at the DM which maximise the S/N of the pulse, while the lower sub-panel shows the time-DM plot. On the right are reported key information of the pulse candidate, such as, e.g., its TOA, the DM maximising its S/N, along with information regarding the observation performed.

Chapter 3

FRB-magnetar connection in a sample of nearby galaxies

Based on Pelliciari et al., 2023, "The Northern Cross Fast Radio Burst project. III. The FRB-magnetar connection in a sample of nearby galaxies", A&A, 674, A223. https://doi.org/10.1051/0004-6361/202346307

3.1 Abstract

The nature of FRB progenitors is still a matter of debate, although magnetars are invoked by most models. The proposed FRB-magnetar connection was strengthened by the discovery of an FRB-like event from the Galactic magnetar SGR J1935+2154 (SGR1935, hereafter) (CHIME/FRB Collaboration et al., 2020; Bochenek et al., 2020).

In this Chapter we aim to investigate how prevalent magnetars such as SGR1935 are within FRB progenitors. To this end, we carried out an FRB search in a sample of seven nearby (< 12 Mpc) galaxies with the NC Radio Telescope for a total of 692 h.

We detected one 1.8 ms burst in the direction of M101 with a fluence of 58 ± 5 Jy ms. Its dispersion measure of 303 pc cm⁻³ places it most likely beyond M101. Considering that no significant detection comes indisputably from the selected galaxies, we place a 38 yr⁻¹ upper limit on the total burst rate (i.e. including the whole sample) at the 95% confidence level. This upper limit constrains the event rate per magnetar to $\lambda_{\rm mag} < 0.42$ magnetar⁻¹ yr⁻¹ or, if combined with literature observations of a similar sample of nearby galaxies, it yields a joint constraint of $\lambda_{\rm mag} < 0.25$ magnetar⁻¹ yr⁻¹. We also provide the first constraints on the expected rate of FRBs hypothetically originating from ULX sources, since some of the galaxies observed during our observational campaign host confirmed ULXs. We obtain < 13 yr⁻¹ per ULX for the total sample of galaxies observed.

Our results indicate that bursts with energies $E>10^{34}$ erg from magnetars such as SGR1935 appear more rarely compared to previous observations and further disfavour them as unique progenitors for the cosmological FRB population. This provides support to the idea that there is a greater contribution from a population of more exotic magnetars not born via core–collapsed supernovae.

3.2 Introduction

Of the FRB progenitor candidates, magnetars – NSs powered by the decay of their strong $(10^{14} - 10^{16} \text{ G})$ magnetic field (Duncan & Thompson, 1992; Rea & Esposito, 2011; Turolla et al., 2015; Kaspi & Beloborodov, 2017) – are the most widely considered. The FRB–magnetar

connection was strengthened by the detection of FRB 20200428, the first Galactic FRB-like event discovered (CHIME/FRB Collaboration et al., 2020; Bochenek et al., 2020); it was observed simultaneously with an X-ray burst (Mereghetti et al., 2020; Ridnaia et al., 2020; Li et al., 2021a; Tavani et al., 2021), emitted by the SGR1935, one of the most active known magnetars (Stamatikos et al., 2014; Lien et al., 2014; Cummings, 2014; Kozlova et al., 2016; Younes et al., 2017). The reported isotropic-equivalent energy emitted at radio wavelengths by this burst, $E_{\rm SGR} \simeq 2 \times 10^{34}$ erg (Bochenek et al., 2020; Margalit et al., 2020b), lies between those of the energetic pulsar giant radio pulses (see e.g., Kuzmin, 2007) and extragalactic FRBs. Further observations revealed fainter bursts from SGR1935 (Zhang et al., 2020; Burgay et al., 2020; Good & Chime/Frb Collaboration, 2020; Alexander & Fedorova, 2020; Kirsten et al., 2021; Dong & Chime/Frb Collaboration, 2022; Maan et al., 2022; Huang et al., 2022; Pearlman & Chime/Frb Collaboration, 2022).

Since magnetars are connected to a young stellar population, they are expected to be found in regions of star formation. While this has been observed for some FRBs (Chatterjee et al., 2017; Marcote et al., 2017; Bassa et al., 2017; Tendulkar et al., 2017; Ravi et al., 2019; Marcote et al., 2020; Bhardwaj et al., 2021b; Niu et al., 2022; Piro et al., 2021; Tendulkar et al., 2021; Nimmo et al., 2022c), others have been found in galaxies with low SFR, mainly in their outskirts (Heintz et al., 2020; Mannings et al., 2021; Bhandari et al., 2022). Notably, the repeating FRB 20200120E was recently found in a globular cluster in the nearby galaxy (NG, hereafter) M81 (Kirsten et al., 2022a). It is also theoretically possible to find young magnetised NSs in GCs, formed either via the accretion-induced collapse of a white dwarf (WD; Tauris et al., 2013; Wang & Liu, 2020) or the collapse of a compact binary system induced by a WD-WD, WD-NS or NS-NS merger (Giacomazzo & Perna, 2013; Schwab et al., 2016; Zhong & Dai, 2020).

CHIME/FRB Collaboration et al. (2020) observed a sample of 15 NGs within 12 Mpc with SFRs higher than that of the MW in order to search for SGR1935-like FRBs–(i.e. bursts with energy $E_0 > 4 \times 10^{34}$ erg). The advantage of targeting NGs over the MW is that the whole population of magnetars is simultaneously observed, therefore increasing the probability of detecting a burst with respect to individual magnetars. No bursts were observed, allowing them to place a constraint on the burst rate of SGR1935-like events $0.007 < \lambda_{\rm mag} < 0.4 \ {\rm yr}^{-1}$ magnetar⁻¹, where the lower limit is set by the detection of the SGR1935 burst itself (CHIME/FRB Collaboration et al., 2020).

We present long monitoring observations of a sample of NGs taken with the NC Radio Telescope in the search for FRBs with the aim to study the FRB–magnetar connection, following CHIME/FRB Collaboration et al. (2020). We note that some of the galaxies observed within our observational campaign host confirmed ultra–luminous X-ray (ULX) sources, accreting binary systems with X-ray luminosities $L_X \geq 10^{39}$ erg s⁻¹, which is significantly higher than any X-ray luminosity emitted by stellar processes (Fabbiano, 1989; Kaaret et al., 2017).

The Chapter is structured as follows: Section 4.3 describes the observations and the sample of NGs observed, Section 3.4 presents constraints on the FRB burst rate of magnetars (Section 3.4.1) and ULXs (Section 3.4.2) determined using these observations. Finally, the implications that our constraints have on the connection between FRBs and their progenitors, along with our conclusions, are discussed in Section 4.5.

3.3 An FRB search in a sample of nearby galaxies

3.3.1 Sample description and observations

Our sample consists of seven galaxies within a maximum distance of 12 Mpc, whose characteristics are summarized in Table 3.1. We selected them based on their reported high SFRs, since magnetars such as SGR1935, born through core-collapse supernovae (CCSNe), trace young

Table 3.1: Properties of the observed NG sample. Columns list: coordinates, distances (D), SFRs, the dispersion measure contribution from the MW interstellar medium (DM_{ISM}) computed as the maximum between the YM16 (Yao et al., 2017) and NE2001 (Cordes & Lazio, 2002, 2003) models, and the total exposure time spent on source. SFRs are estimated from H α luminosities for all the galaxies but M82 and IC 342, for which infrared luminosities were used. References for distances are: [1] McConnachie et al. (2005); [2] Karachentsev et al. (2004); [3] Dalcanton et al. (2009); [4] Shappee & Stanek (2011); [5] Anand et al. (2018); [6] Newman et al. (2001); and [7] Hoyt et al. (2019). References for SFRs are: [8] Rahmani et al. (2016); [9] Gao & Solomon (2004); [10] Förster Schreiber et al. (2003); [11] Kennicutt et al. (2008).

	R.A. (J2000)	Dec (J2000)	D	SFR	$\mathrm{DM}_{\mathrm{ISM}}$	T
			(Mpc)	$(M_{\odot} \text{ yr}^{-1})$	$(pc cm^{-3})$	(hr)
M31	$00^{\rm h}42^{\rm m}44.3^{\rm s}$	$+41^{\circ}16'07.5''$	0.79 ± 0.03 [1]	0.35 [8]	142	51
IC342	$03^{\rm h}46^{\rm m}48.5^{\rm s}$	$+68^{\circ}05'46.0''$	3.3 ± 0.3 [2]	2.8 [9]	178	102
M82	$09^{\rm h}55^{\rm m}52.4^{\rm s}$	$+69^{\circ}40'46.9''$	3.53 ± 0.04 [3]	13 [10]	41.2	184
M101	$14^{\rm h}03^{\rm m}12.6^{\rm s}$	$+54^{\circ}20'55.5''$	$6.4 \pm 0.5 \ [4]$	2.9[11]	30.9	96
NGC6946	$20^{\rm h}34^{\rm m}52.3^{\rm s}$	$+60^{\circ}09'13.2''$	$7.7 \pm 0.3 [5]$	4.3[11]	145.8	115
M106	$12^{\rm h}18^{\rm m}57.6^{\rm s}$	$+47^{\circ}18'13.4''$	$7.8 \pm 0.6 \ [6]$	2.8[11]	25.8	84
M66	$11^{\rm h}20^{\rm m}15.0^{\rm s}$	$+12^{\circ}59'28.6''$	11.1 ± 0.4 [7]	2.7 [11]	31.1	63

star formation sites. Apart from M31 and IC 342, all the galaxies were already included in the sample observed by CHIME/FRB Collaboration et al. (2020). We included M31 for its proximity and similarity to the MW. As already mentioned, among the galaxies observed, M82, M101, IC 342 and NGC 6946 host confirmed ULXs. They are M82 X-1 (Ptak & Griffiths, 1999), M101 X-1 (Stetson et al., 1998), IC 342 X-1, IC 342 X-2 (Rana et al., 2015) and NGC 6946 X-1 (Fabbiano & Trinchieri, 1987; Roberts & Colbert, 2003). These objects are currently believed to be the result of super-Eddington accretion onto a stellar mass BH (e.g. Liu et al., 2013), or a NS (Pintore et al., 2020, and references therein). We monitored each galaxy daily during its transit through the telescope's primary beam using eight cylinders of the N-S arm of the array (we refer the reader to Locatelli et al., 2020, for details of the system). Due to limitations of this acquisition software, a source cannot be tracked continuously as it moves across the telescope's field of view; therefore, we employed the "shift and track" strategy used in Trudu et al. (2022), where seven discrete delay values are approximately equally spaced in angular size to cover the field of view. The resulting telescope beam pattern is shown in Figure 3.1, where the seven peaks corresponding to the seven beam-forming delays are clearly visible. Such a beam pattern implies that the sensitivity to the source varies by up to 40% as it transits through the primary beam. As the variation in the beam response within each delay bin is small ($\approx 10\%$), in the following analysis we assume it to be constant and equal to its average value (dashed line in Figure 3.1). The energy detection threshold, E_{\min} , for a burst observed in the delay bin j from the galaxy i can be written as

$$E_{\min,i,j} = 4\pi D_i^2 \,\Delta\nu \,\frac{F}{A_j},\tag{3.1}$$

where D_i is the source distance, $\Delta \nu = 16$ MHz the observing bandwidth, A_j the average beam gain in the j-th delay bin and F = 38 Jy ms the NC fluence threshold corresponding to the peak of the central beam assuming a 10σ detection threshold (Trudu et al., 2022). In this Chapter we assume 1 ms as the reference burst duration.

Observations started on December 26, 2021, and ended on August 21, 2022, for a total of 692 hr. Data were stored to disk with a time resolution of 138.24 μ s and a frequency channel width of 14.468 kHz. We calibrated our data using interferometric observations of Cas A (see Locatelli et al., 2020, for details on the calibration procedure), carried out approximately at

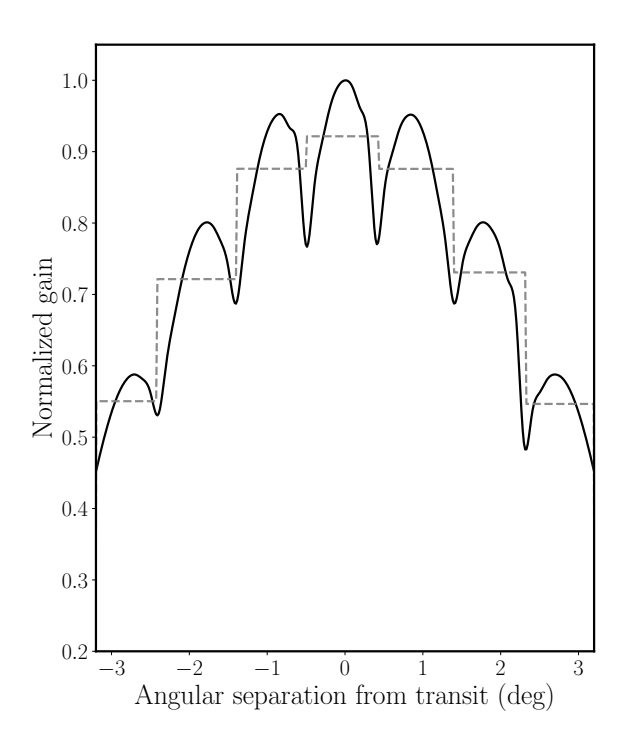


Figure 3.1: Normalized NC beam-forming response (solid line) as the source transits across the telescope field of view. Dashed lines represent the average value of the telescope beam response for each delay bin.

the beginning, halfway and at the end of the observational campaign. Receiver phases and amplitudes remained fairly constant over week-long timescales; nevertheless, our observing campaign was interspersed with monthly observations of the pulsar B0329+54 and the repeating FRB 20180916B (CHIME/FRB Collaboration et al., 2019). Both sources served as calibration tests for the stability of our system and, at the same time, FRB 20180916B was observed within its window of expected activity (CHIME/FRB Collaboration et al., 2019; Pastor-Marazuela et al., 2021; Pleunis et al., 2021b; Trudu et al., 2022) for the purpose of obtaining multiwavelength observations (Pilia et al., 2020; Tavani et al., 2020; Trudu et al., 2022).

We regularly detected single pulses from B0329+54 at its nominal DM, ~ 26.8 pc cm⁻³ (Hassall et al., 2012), and detected two new bursts from FRB 20180916B, in addition to those presented in Trudu et al. (2022), in agreement with the expected repetition rate. Figure 3.2 shows their de-dispersed waterfall plots, labelled B4 and B5 to follow the Trudu et al. (2022) nomenclature, and their best-fit values are listed in Table 3.2. These detections provide evidence for calibration stability across the whole campaign.

The search for FRBs in our galaxy sample was performed using the SPANDAK pipeline (Gajjar et al., 2018), which flags RFI through RFIFIND (Ransom et al., 2002) and searches for single pulses with HEIMDALL (Barsdell et al., 2012). We used the same search setup described in Trudu et al. (2022), within the $0 < DM < 1000 \text{ pc cm}^{-3}$ range, with a S/N greater than six and a boxcar duration shorter than 35 ms in order to balance the search time and our scientific goals whilst remaining consistent with the observed width distribution of FRBs (Petroff et al., 2022; CHIME/FRB Collaboration et al., 2021).

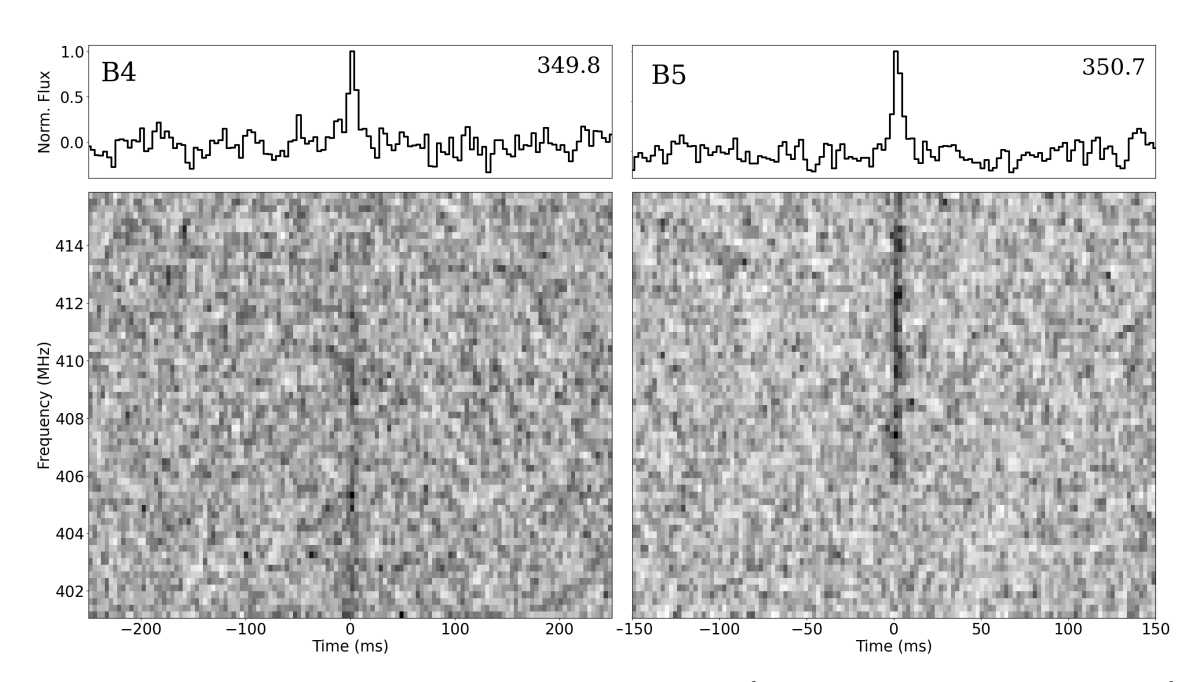


Figure 3.2: Bursts from FRB 20180916B observed on April 30th 2022 (left panel) and August 9th 2022 (right panel), respectively. Bottom panels show the dynamic spectra, while the top panels show the frequency averaged profiles. The best-fit DMs (in pc cm⁻³) at which the bursts were de-dispersed are reported in the top right corner of each plot. Data were down-sampled to have 64 frequency channels, each 0.25 MHz wide, and time bins with 2.2 ms width for better display.

Table 3.2: Properties of B4 and B5 bursts from FRB 20180916B. We report, from the top row to the bottom, the barycentric time of arrival (TOA) expressed as the modified julian day (MJD), the signal to noise ratio (S/N), the fit-optimized DM, the full width at half maximum (FWHM) duration, the flux density and the fluence of the bursts.

Parameter	B4	В5
TOA (MJD)	59699.52603591	59800.25184782
$\mathrm{S/N}$	15	20
$DM (pc cm^{-3})$	349.8 ± 0.1	350.7 ± 0.1
$\Delta t \; (\mathrm{ms})$	6.35 ± 0.1	5.7 ± 0.3
Flux density (Jy)	15 ± 1	19 ± 1
Fluence (Jy ms)	96 ± 6	108 ± 5

Table 3.3: Observational properties of FRB 20220320. The uncertainty on the FRB position corresponds to the beam full width at half maximum.

Parameter	Value
R.A. (J2000, deg)	211(3)
Dec. (J2000, deg)	54.4(5)
T.o.A	2022-03-20 01:14:02.40 (UT)
S/N	11
$DM (pc cm^{-3})$	303 ± 2
$\Delta t \; (\mathrm{ms})$	1.8 ± 0.3
Flux density (Jy)	32 ± 3
Fluence (Jy ms)	58 ± 5

3.3.2 FRB detection from the direction of M101

We found no candidates with a S/N > 10 throughout the whole campaign and ~ 100 candidates with $6 \le S/N \le 10$ that were further visually inspected and double-checked. We selected a minimum S/N of 6 to avoid missing potential weak signals during the search for FRB signals; however, throughout the analysis presented in this Chapter (see Section 3.4), we consider a more conservative minimum S/N of 10. Most candidates were discarded due to the presence of RFI contamination and noise properties that showed deviations from a theoretical Gaussian distribution. The only candidate that conservatively passed the selection, detected with a $S/N \sim 11$, is shown in Figure 3.3.

We assessed the likelihood of a candidate signal by computing the number of false candidates with S/N higher than the detection threshold, expected because of noise outliers. The number of false positive events is a function of the S/N and can be computed as (Cordes & McLaughlin, 2003)

$$N_{\text{false}}(> \text{S/N}) = 2N_{\text{DM}} \frac{\Delta T}{dt} P(> \text{S/N}), \tag{3.2}$$

where $N_{\rm DM}$ is the number of DM trials considered in the FRB search, set internally in HEIMDALL, ΔT the total duration of the observations, dt the time sample duration, and

$$P(> S/N) = \frac{2}{\sqrt{\pi}} \int_0^x e^{-z^2} dz \equiv \frac{1}{2} \left[1 - \operatorname{erf}\left(\frac{S/N}{\sqrt{2}}\right) \right]$$
(3.3)

the probability that an event is due to a noise statistical fluctuation. In our case, $N_{\rm DM} \sim 3000$, $\Delta T = 692$ h, and dt $\sim 138~\mu \rm s$, resulting in $N_{\rm false} \sim 10^{-9}$ for S/N ≥ 10 . Hence, we consider our candidate to be a genuine FRB.

The burst, hereafter FRB 20220320, was detected on 2022 March 30 UT = 01:14:02.40 (Barycentric time of arrival, ∞ MHz), in the direction of M101, and its properties are listed in Table 3.3.

We measured a DM = 303 ± 2 pc cm⁻³, which disfavours a local origin. The DM contribution along the line of sight of M101 due to the ISM is DM_{ISM} $\simeq 23-31$ pc cm⁻³, according to the NE2001 (Cordes & Lazio, 2002, 2003) and the YMW16 (Yao et al., 2017) electron density models, while the contribution from the Galactic halo is ~ 50 pc cm⁻³ (Agarwal et al., 2019; Macquart et al., 2020a; Yamasaki & Totani, 2020; Lemos et al., 2023). Finally, the intergalactic medium (considering $z \simeq 0.001$) contributes approximately ~ 2 pc cm⁻³ (Macquart et al., 2020a), although this value, for low redshift galaxies, depends on the line of sight (Li et al., 2019). These contributions, if coming from M101, would imply a moderately high DM_{host}, $\simeq 220$ pc cm⁻³. In our case, the almost face-on inclination of M101 seems to disfavour a large DM_{host} for M101 (Xu & Han, 2015). Although James et al. (2022b), by analysing 16 FRBs from Australian Square

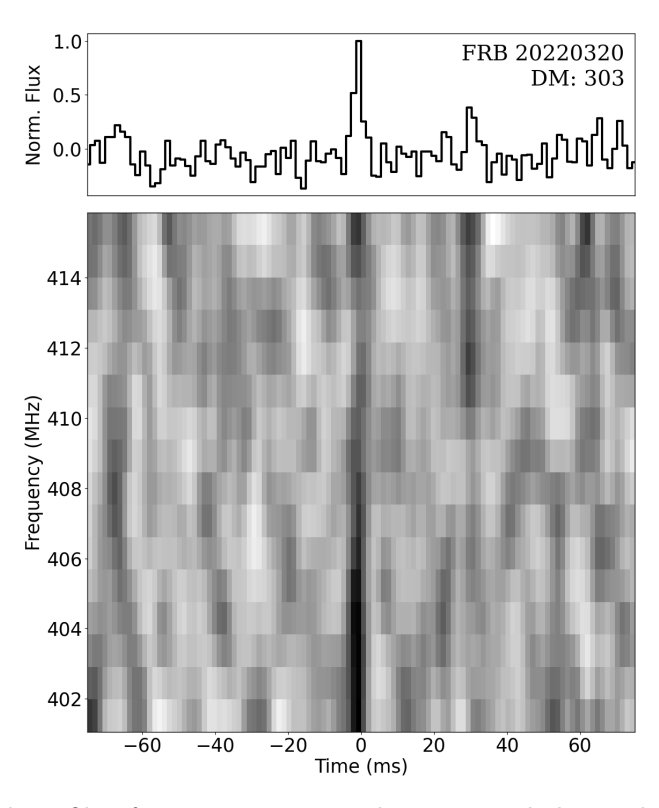


Figure 3.3: De-dispersed profile of FRB 20220320. The top panel shows the frequency-averaged time series, and the bottom panel shows its dynamic spectrum, coherently de-dispersed at DM = 303 pc cm⁻³. The time and frequency resolutions are 1.3 ms and 1 MHz, respectively, chosen for a better visualisation of the burst.

Kilometre Array Pathfinder (ASKAP) observations, found $\langle DM_{host} \rangle \sim 186 \pm 50 \text{ pc cm}^{-3}$, which would be compatible with an origin from M101, other works point towards lower values for the host DM contribution (Niino, 2020; Zhang et al., 2020). This is further evidence that an association with M101 is unlikely.

If we consider the burst to be originating farther away, assuming a more conservative value ${\rm DM_{host}} \simeq 100~{\rm pc~cm^{-3}}$, the burst would be placed at a maximum redshift of $z \sim 0.18$, that is to say, at a luminosity distance of $\sim 870~{\rm Mpc}$. For the distance estimation we considered a seven-year Wilkinson Microwave Anisotropy Probe (WMAP7) cosmology (Komatsu et al., 2011) to be consistent with Macquart et al. (2020a). Given this maximum redshift, its spectral luminosity would be at most $6.3 \times 10^{33}~{\rm erg~s^{-1}~Hz^{-1}}$, well within the range of extragalactic FRB spectral luminosities (Bochenek et al., 2020; CHIME/FRB Collaboration et al., 2020; Luo et al., 2020).

3.4 Upper limits on the FRB repetition rate from our observations

In this section we show how the observations conducted in our NG campaign allowed us to extract important upper limits on the FRB burst rate. In particular, we developed a simple model to calculate the expected rate of FRB events from the whole sample of galaxies listed in Table 3.1, considering as a first case a single population of SGR1935-like magnetars as FRB progenitors. By taking λ_{mag} , the average burst rate per magnetar, and γ , the power-law energy distribution slope for magnetar bursts, as free parameters, we discuss how the upper limits on the rate from the whole galaxy sample translate into upper limits on λ_{mag} and γ . We also discuss how our observations could constrain the FRB event rate if FRBs originated from ULXs.

Indeed, accretion-based mechanisms for the FRB engine have been proposed (Waxman, 2017; Katz, 2017, 2020; Sridhar et al., 2021; Deng et al., 2021).

3.4.1 SGR1935-like magnetars

We started by computing the total burst rate from our galaxy sample, considering a single population of magnetars similar to SGR1935. This means that we restricted our analysis to magnetars that have radio efficiencies $\eta \sim 10^{-5}$, the ratio of energy radiated in the radio and X-ray bands by SGR1935 (Mereghetti et al., 2020; Tavani et al., 2021; Ridnaia et al., 2020; CHIME/FRB Collaboration et al., 2020; Bochenek et al., 2020), and burst energetics $E \geq E_0$, where $E_0 = 2 \times 10^{34}$ erg is the isotropic radio energy released by FRB 20200428 (Bochenek et al., 2020; Margalit et al., 2020b; CHIME/FRB Collaboration et al., 2020). This energy follows by considering d = 7 kpc to be the distance to SGR1935 (Margalit et al., 2020b).

Following CHIME/FRB Collaboration et al. (2020), we assumed that the magnetar burst rate \Re from a given galaxy is proportional to its SFR. We computed the number of SGR1935-like magnetars residing in a certain galaxy by scaling for $N_{\rm mag}/{\rm SFR}_{\rm MW}$, with $N_{\rm mag}=29$ (Olausen & Kaspi, 2014; Kaspi & Beloborodov, 2017) the number of Galactic magnetars and SFR_{MW} = 1.65 \pm 0.19 M_{\odot} yr⁻¹ the Galactic SFR (Licquia & Newman, 2015).

With these prescriptions, the rate expected from the galaxy i of our sample can be expressed as

$$\Re(\lambda_{\text{mag}}, \gamma; > E_{\text{min},i,j}) = N_{\text{mag}} \frac{\text{SFR}_{i}}{\text{SFR}_{MW}} \times \\
\times \int_{E_{\text{min},i,j}}^{E_{\text{max}}} K_{0} \left(\frac{E}{E_{0}}\right)^{-\gamma} \Theta[E - E_{0}] dE, \tag{3.4}$$

where $E_{\min,i,j}$ is the minimum burst energy detectable from the galaxy i in the delay bin j (equation 3.1). The integral is the burst rate energy function, which we assumed to follow a power law with index γ . We note that the Heaviside function, Θ , restricts the case to SGR1935-like bursts (i.e. with energy $E \geq E_0$). We considered the maximum energy, E_{\max} , to be

$$E_{\text{max}} = \eta \, E_{\text{mag}},\tag{3.5}$$

with $\eta \sim 10^{-5}$ and $E_{\rm mag}$ the total magnetic energy reservoir for a magnetar with magnetic field B (Margalit et al., 2020b):

$$E_{\text{mag}} = 3 \times 10^{49} \left(\frac{B}{10^{16} \,\text{G}}\right)^2 \,\text{erg.}$$
 (3.6)

We considered $B = 2 \times 10^{14}$ G, the magnetic field strength of SGR1935 (Israel et al., 2016), and verified that a higher value for B does not appreciably affect our results.

The burst rate normalization, K_0 , can be expressed as a function of the burst rate per magnetar λ_{mag} :

$$\lambda_{\text{mag}} = \int_{E_0}^{E_{\text{max}}} K_0 \left(\frac{E}{E_0}\right)^{-\gamma} dE, \tag{3.7}$$

yielding:

$$K_0 = \lambda_{\text{mag}} \frac{(1 - \gamma) E_0^{-\gamma}}{E_{\text{max}}^{-\gamma+1} - E_0^{-\gamma+1}}.$$
 (3.8)

Equation 3.4 can therefore be re-written as

$$\Re(\lambda_{\text{mag}}, \gamma; > E_{\text{min},i,j}) = N_{\text{mag}} \lambda_{\text{mag}} \frac{\text{SFR}_{i}}{\text{SFR}_{\text{MW}}} \frac{E_{\text{max}}^{-\gamma+1} - E_{\text{min},i,j}^{-\gamma+1}}{E_{\text{max}}^{-\gamma+1} - E_{0}^{-\gamma+1}}.$$
(3.9)

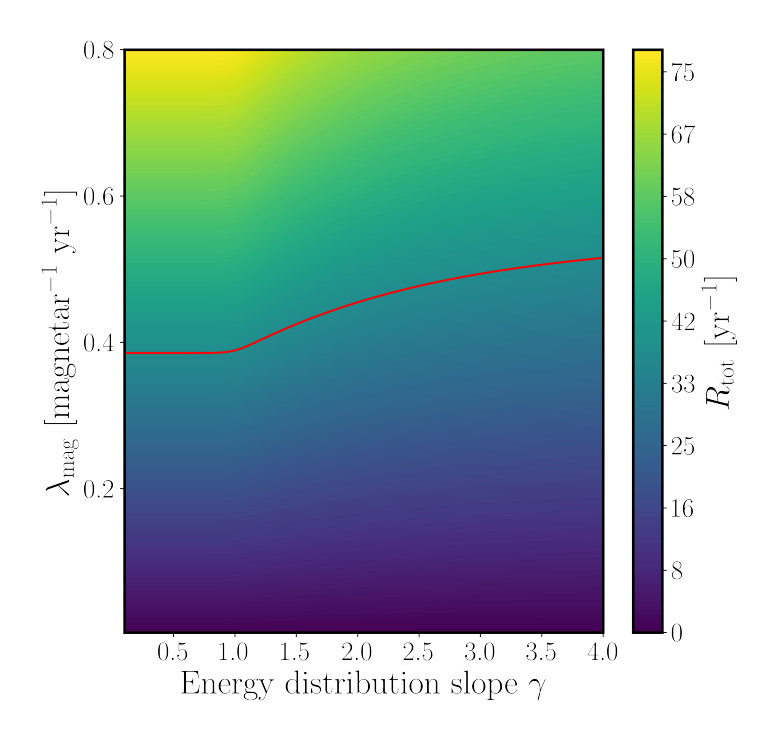


Figure 3.4: Expected burst rate (colour-map) as a function of the energy distribution slope, γ , and the SGR1935-like burst rate per magnetar, λ_{mag} , from the whole observing campaign of NGs. The red line is the 95% CL upper limit obtained via our observations.

We could then compute the total expected burst rate from our NG sample as the sum of the rate for each galaxy in each delay bin, weighted by their corresponding integration time:

$$\mathcal{R}_{\text{tot}}(\lambda_{\text{mag}}, \gamma) = \frac{\sum_{i}^{N} \sum_{j}^{N_b} \mathcal{R}(\lambda_{\text{mag}}, \gamma; > E_{\min,i,j}) T_{i,j}}{\sum_{i}^{N} \sum_{j}^{N_b} T_{i,j}},$$
(3.10)

where $N_b = 7$ is the number of delay bins and $T_{i,j}$ is the total integration time of the *i*-th galaxy in the delay bin *j*. The total expected burst rate is mildly dependent upon the slope of the energy distribution and much more significantly dependent upon the burst rate per magnetar as can be visually assessed in Figure 3.4. Our observations led to a 95% confidence level (CL; Gehrels, 1986) upper limit on the total burst rate of $\mathcal{R}_{\text{tot}} < 38 \text{ yr}^{-1}$. By imposing this upper limit, we obtain a 95% CL constraint on the burst rate per magnetar that varies between $\lambda_{\text{mag}} < 0.38 \text{ magnetar}^{-1} \text{ yr}^{-1}$ for $\gamma \leq 1$ and $\lambda_{\text{mag}} < 0.47 \text{ magnetar}^{-1} \text{ yr}^{-1}$ for $\gamma \simeq 3$. After marginalizing over the energy distribution slope γ , we derive $\lambda_{\text{mag}} < 0.42 \text{ magnetar}^{-1} \text{ yr}^{-1}$.

Previous works derived constraints for the magnetar burst rate. In particular, CHIME/FRB Collaboration et al. (2020) obtained $0.007 < \lambda_{\rm mag} < 0.4$ magnetar⁻¹ yr⁻¹ at the 95% CL from the detection of FRB 20200428 and the non-detection from a sample of 15 NGs. However, the authors adopted slightly different values than us for the distances and SFRs of the galaxies that are common to our sample (see their Extended Data Table 1), and they considered a lower SFR_{MW} of 1 M_{\odot} yr⁻¹. If we use their values in our estimate, we obtain $\lambda_{\rm mag} < 0.3$ magnetar⁻¹ yr⁻¹. By combining our observations with CHIME/FRB Collaboration et al. (2020), we can obtain an even further improved upper limit on $\lambda_{\rm mag}$. Assuming the distance and SFR values presented in Table 3.1 for both samples, we recomputed the total rate expected from the joint observations (Eqs. 3.9 and 3.10), which has to be compared with the upper limit obtained from the total observing time (\sim 1370 h). As a result, we obtain $\lambda_{\rm mag} < 0.25$ magnetar⁻¹ yr⁻¹ at the 95% CL, the most stringent upper limit on the burst rate per magnetar to date. In Section 4.5

Table 3.4: Upper limits for the FRB repetition rate (last column) coming from confirmed ULXs. In the second column we report the number of ULXs present in a given galaxy. The last row considers the total expected ULX ensamble derived from equation (3.12).

ULX	$N_{ m u}$	$\lambda_{\rm u} [{\rm yr}^{-1}]$
IC 342 X-1, IC 342 X-2	2	< 128
M82 X-2	1	< 140
M101 X-1	1	< 273
NGC 6946 X-1	1	< 227
All	14	< 13

we discuss this result in the framework of the FRB-magnetar connection.

3.4.2 Ultra-luminous X-ray sources

An alternative formation channel to the more standard magnetar models predicts that FRBs can be produced by short-lived relativistic flares from super-Eddington accreting NSs and BHs (Sridhar et al., 2021). The isotropic energy emitted by this kind of FRB is postulated to lie in the range 10³⁴ erg - 10⁴⁵ erg (Sridhar et al., 2021), which implies that these sources would have been detected with the NC sensitivity. Therefore, the observing time spent on these galaxies is useful for placing an upper limit on the rate of FRBs produced by these accreting objects.

We followed the approach described in Section 3.4 and expressed the rate expected from the population of ULXs, $\mathcal{R}_{u,i}$, in the galaxy i of our sample:

$$\mathcal{R}_{u,i}(\lambda_u) = N_{u,i} \,\lambda_u,\tag{3.11}$$

where $N_{u,i}$ is the number of ULX sources expected in the galaxy i and λ_u is the average burst rate per ULX for energies in the $10^{34} < E < 10^{45}$ erg range. The number of ULX sources can be expressed as a function of the SFR (Kovlakas et al., 2020):

$$N_{u,i} = 0.51 \frac{\text{SFR}_i}{\text{M}_{\odot} \,\text{yr}^{-1}}.$$
 (3.12)

We expect from equation (3.12) a total of ~ 14 ULXs in the galaxies we observed. The total expected burst rate, $\mathcal{R}_{u,\text{tot}}$, from our NG sample then becomes:

$$\mathcal{R}_{u,\text{tot}}(\lambda_u) = \frac{\sum_{i}^{N} \sum_{j}^{N_b} \mathcal{R}_{u,i}(\lambda_u) T_{i,j}}{\sum_{i}^{N} \sum_{j}^{N_b} T_{i,j}},$$
(3.13)

The observed upper limit at the 95% CL on the total burst rate is $\simeq 38~\rm yr^{-1}$, the same as determined in Section 3.4.1, since it depends only on the total observing time. Therefore, by imposing $\mathcal{R}_{u,\text{tot}} < 38~\rm yr^{-1}$, we obtain $\lambda_u < 13~\rm yr^{-1}$ for the average burst rate per ULX. This is the first upper limit on the FRB repetition rate hypothetically coming from ULXs. We note that this upper limit is two to three orders of magnitude lower than the reported repetition rate of most active repeaters from FRB 20121102A and FRB 20180916B, $r \sim 10^3~\rm yr^{-1}$ (Margalit et al., 2020b). We also find this contrast by computing the repetition rate for confirmed ULXs only, that is to say, without estimating the population of ULXs from equation (3.12) and only considering already discovered ULXs in the galaxies we observed. We report the upper limits obtained for each case in Table 3.4 and discuss the possible implications of these results in the following section.

3.5 Discussion and conclusions

In this paper we present an FRB search in a sample of seven NGs taken with the NC Radio Telescope. The campaign was 692 h long and yielded the detection of a 58 Jy ms, 1.8 ms long burst with a DM = 303 pc cm⁻³, observed in the direction of M101, although most likely coming from a more distant source. Therefore, we consider that no detections came from the monitored galaxies. We used this result to investigate the connection between FRBs and magnetars, by computing the total burst rate, \mathcal{R}_{tot} , expected from our galaxy sample, assuming, as unique FRB progenitors, magnetars such as SGR J1935+2154, and obtaining $\mathcal{R}_{\text{tot}} < 38 \text{ yr}^{-1}$ at the 95% CL. We considered λ_{mag} , the average burst rate per magnetar, and γ , the slope of the burst energy distribution, as free parameters for our SFR-based model. In addition, we derived the average FRB rate per ULX from the same observations of NGs. Among the target galaxies of our observational campaign, some host confirmed ULXs, from which, at least theoretically, an FRB would have obtained enough energy (Sridhar et al., 2021) to be detected by the NC.

Since the detection of the Galactic FRB-like signal, it has been tempting to claim that magnetars such as SGR1935 (i.e. magnetars similar in energetics and formed through CCSNe) represent the entire cosmological population of FRBs. Although the implied volumetric rate from the detection of FRB 20200428 is consistent with the faint energy of the cosmological rate density (Lu et al., 2022), SGR1935-like magnetars cannot explain the high repetition rate of active repeaters (Margalit et al., 2020b). Moreover, FRB 20200428 is about one order of magnitude fainter than the average FRB (Bochenek et al., 2020; CHIME/FRB Collaboration et al., 2020; Luo et al., 2020), although giant magnetar flares may be bright enough to fill the gap (Margalit et al., 2020b). The discrepancy in the repetition rate, along with the discovery of the M81 repeater localized in a globular cluster (Bhardwaj et al., 2021b; Kirsten et al., 2021), led to consider other, more exotic NS formation channels (Kremer et al., 2021, 2023), and question the presence of a single population of magnetars as FRB progenitors.

Our observations do not constrain the burst energy slope well, although they somewhat disfavour flat slopes ($\gamma < 1$) over steeper ones ($\gamma > 1$). The average burst rate per magnetar is, instead, constrained to be $\lambda_{\rm mag} < 0.42$ magnetar⁻¹ yr⁻¹. This upper limit halves the range for the magnetar burst rate implied by the detection from the STARE2 (Bochenek et al., 2020), $0.0036 < \lambda_{\rm mag} < 0.8$ magnetar⁻¹ yr⁻¹, consistently with the results from CHIME NG observations, $0.007 < \lambda_{\rm mag} < 0.4$ magnetar⁻¹ yr⁻¹ (CHIME/FRB Collaboration et al., 2020). We also show how the upper limit lowers to $\lambda_{\rm mag} < 0.25$ magnetar⁻¹ yr⁻¹ if we consider our NG observations combined with the monitoring reported in CHIME/FRB Collaboration et al. (2020).

Considering the STARE2 detection, Margalit et al. (2020b) already pointed out that the cosmological FRB rate, including repeating sources, can be explained only by adding a second magnetar population that is younger and with a stronger magnetic field with respect to the SGR1935-like ones (Margalit et al., 2019; Blanchard et al., 2016). This second population includes more exotic magnetars, not born through the usual supernova core collapse, but through a much rarer formation channel. Our constraints imply that the burst rate per magnetar of SGR-like events is approximately a factor of two smaller than previously reported, implying rarer events. From the perspective of a two-population model, our results imply that rare magnetars should be more prominent than considered earlier in order to compensate for the smaller burst rate from SGR1935-like magnetars. Moreover, the detection of FRB 20200120E in a globular cluster (Bhardwaj et al., 2021a; Kirsten et al., 2022a) has similar implications (Lu et al., 2022), namely that the formation of magnetars is possible inside globular clusters through compact object mergers, accretion-induced collapse, or a WD-merger-induced collapse (Kirsten et al., 2022a; Kremer et al., 2021, 2023). However, the nanosecond structures observed in some bursts from FRB 20200120E could be explained in terms of a recycled millisecond pulsar origin

(Majid et al., 2021; Kremer et al., 2021). Hence, it is not clear whether M81-like FRBs could represent this needed population of rarer FRB progenitors.

Among other exotic but prominent progenitor models, we find accretion-based mechanisms (Waxman, 2017; Katz, 2017, 2020; Sridhar et al., 2021; Deng et al., 2021). In particular, the recent model of Sridhar et al. (2021) is able to explain both the energetics and the chromaticity behaviour seen in FRB 20180916B (Pastor-Marazuela et al., 2021). Estimating the total number of ULXs present in our sample of galaxies to be 14, we have constrained the average rate of FRB events per ULX to $\lambda_u < 13~\rm yr^{-1}$ at the 95% CL. We have also provided individual upper limits for each monitored ULX. These initial estimates show a discrepancy of a few orders of magnitude when compared to the repetition rates of the most active repeaters (Margalit et al., 2020b). As already pointed by Sridhar et al. (2021), a strongly magnetised object in the compact pair could be necessary to power cosmological FRB luminosities, making these events much rarer and more difficult to detect. In conclusion, our limits on the burst rate disfavour both magnetars and ULXs as progenitors of very active repeating sources such as FRB 20180916B and FRB 20121102A.

Chapter 4

Multiwavelength study of the actively repeating FRB 20220912A

Based on Pelliciari et al. 2024, "The Northern Cross Fast Radio Burst project IV. Multi-wavelength study of the actively repeating FRB 20220912A", A&A, 609, A219. https://doi.org/10.1051/0004-6361/202450271

4.1 Abstract

A fraction of the FRB population have shown repeating bursts, however it is still unclear whether these represent a distinct class of sources. We investigated the bursting behaviour of FRB 20220912A, one of the most active repeating FRBs known thus far. In particular, we focused on its burst energy distribution, linked to the source energetics, and its emission spectrum, with the latter directly related to the underlying emission mechanism. We monitored FRB 20220912A at 408 MHz with the NC radio telescope and at 1.4 GHz using the 32-m Mc radio telescope. Additionally, we conducted 1.2 GHz observations taken with the uGMRT searching for a PRS coincident with FRB 20220912A, and we included high energy observations in the 0.3–10 keV, 0.4–100 MeV and 0.03–30 GeV energy range. We report 16 new bursts from FRB 20220912A at 408 MHz during the period between October 16th 2022 and December 31st 2023. Their cumulative spectral energy distribution follows a power law with slope $\alpha_E = -1.3 \pm 0.2$ and we measured a repetition rate of $0.19 \pm 0.03 \; hr^{-1}$ for bursts having a fluence of $\mathcal{F} \geq 17 \; Jy$ ms. Furthermore, we report no detections at 1.4 GHz for $\mathcal{F} \geq 20$ Jy ms. These non-detections imply an upper limit of $\beta < -2.3$, with β being the 408 MHz – 1.4 GHz spectral index of FRB 20220912A. This is inconsistent with positive β values found for the only two known cases in which an FRB has been detected in separate spectral bands. We find that FRB 20220912A shows a decline of four orders of magnitude in its bursting activity at 1.4 GHz over a timescale of one year, while remaining active at 408 MHz. The cumulative spectral energy distribution (SED) shows a flattening for spectral energy $E_{\nu} \geq 10^{31}$ erg Hz⁻¹, a feature seen thus far in only two hyperactive repeaters. In particular, we highlight a strong similarity between FRB 20220912A and FRB 20201124A, with respect to both the energy and repetition rate ranges. We also find a radio continuum source with $240 \pm 36 \mu Jy$ flux density at 1.2 GHz, centered on the FRB 20220912A coordinates. Finally, we place an upper limit on the γ to radio burst efficiency η to be $\eta < 1.5 \times 10^9$ at 99.7% confidence level, in the 0.4 – 30 MeV energy range. The strong similarity between the cumulative energy distributions of FRB 20220912A and FRB 20201124A indicate that bursts from these sources are generated via similar emission mechanisms. Our upper limit on β suggests that the spectrum of FRB 20220912A is intrinsically narrow-band. The radio continuum source detected at 1.2 GHz is likely due to a star formation environment surrounding the FRB, given the absence of a source compact on milliarcsecond scales brighter

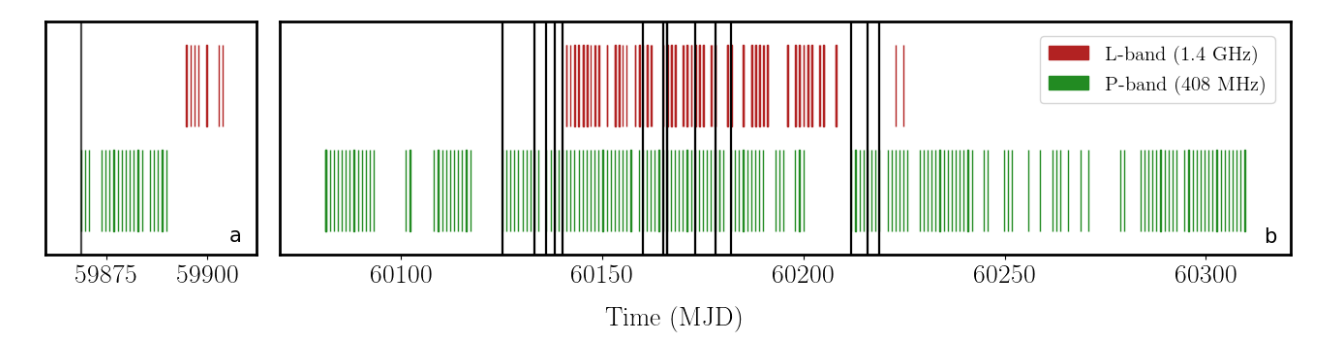


Figure 4.1: Overview of the FRB 20220912A monitoring campaign. Panel a displays the MJD range 59868 – 59903 (35 days), while panel b shows the MJD range 60081 – 60309 (228 days). Green (red) vertical blocks indicate observations at 408 MHz (1.4 GHz). Vertical black lines represent burst detections at 408 MHz. Each observing session at 408 MHz last \sim 35 minutes, while 1.4 GHz observations started 15 minutes before the P band run and last \sim 60 minutes.

than 48 μ Jy beam⁻¹ (Hewitt et al., 2024). Finally, the upper limit on the ratio between the γ and radio burst fluence disfavours a giant flare origin for the radio bursts unlike observed for the Galactic magnetar SGR 1806-20.

4.2 Introduction

Nowadays there are about ~ 800 distinct known FRB sources (CHIME/FRB Collaboration et al., 2021; Xu et al., 2023) and most of them classified as one-off events. However, about 50 sources have shown repeated emission (Chime/Frb Collaboration et al., 2023), ruling out catastrophic events as their origin. It is unclear whether all FRB sources are repeating in nature, although bursts from repeaters are statistically wider in temporal width and narrower in bandwidth compared to one-off FRBs (Pleunis et al., 2021b).

Among repeaters, various differences are found, especially in their observed level of activity. Indeed, the burst rate of repeaters spans a wide range of values, ranging from less active sources, which can exhibit a burst rate as low as $\sim 10^{-3}~\rm hr^{-1}$ (Chime/Frb Collaboration et al., 2023) to the most active ones (so-called hyperactive sources) showing sporadic burst storms in which the repetition rate rises up to several hundreds of bursts per hour (Li et al., 2021b; Nimmo et al., 2022a; Xu et al., 2022; Zhang et al., 2022, 2023a; Feng et al., 2023). On the other hand R3, which shows a 16.3 \pm 2.6 days periodic window of activity (Pleunis et al., 2021b; Pastor-Marazuela et al., 2021), has not revealed any burst storms, given that its repetition rate is consistent with an origin coming from a Poissonian process (Sand et al., 2023).

An interesting feature that has emerged from very long monitoring of the two hyperactive repeaters R1 and FRB 20201124A is the flattening of their burst energy distributions at the highest burst energies (Hewitt et al., 2022; Jahns et al., 2023; Kirsten et al., 2024). This suggests a possible link between repeating and non repeating FRB sources (James et al., 2022a; Kirsten et al., 2024), the latter presenting a flat luminosity distribution (James et al., 2022b,a), which could potentially imply that the most energetic bursts are produced by a different emission mechanism compared to the less energetic ones.

In September 2022, CHIME discovered FRB 20220912A, a repeating FRB source having DM of 219.46 pc cm⁻³ (McKinven & Chime/Frb Collaboration, 2022), subsequently localised with arcsecond precision in the outskirts of a moderately star forming, massive galaxy at redshift z = 0.0771 (Ravi et al., 2023). Bursts were detected at different frequencies, between 408 MHz and 2.3 GHz (see Zhang et al., 2023a, and references therein), with a period of particularly high activity. A burst rate of $\sim 400 \text{ hr}^{-1}$ was observed at 1.4 GHz, for a 90% fluence threshold

of 4 mJy ms (Zhang et al., 2023a). A fraction of the observed bursts show very narrow-band spectra (Zhang et al., 2023a) and short duration ($\sim 16~\mu s$), the latter usually clustered in dense burst forests (Hewitt et al., 2023). The source was recently localised at RA (J2000) = $23^{\rm h}09^{\rm m}04.8988^{\rm s} \pm 0.0003^{\rm s}$, Dec (J2000) = $48^{\circ}42'23.908'' \pm 0.005''$ (Hewitt et al., 2024), placing it closer to the centre of the host galaxy than previously suggested. Their observations also rule out the presence of a PRS down to a $\sim 20~\mu \rm Jy~beam^{-1}$ level. It was argued by Ravi et al. (2023) that the DM contribution by the host is low ($\leq 53~\rm pc~cm^{-3}$). A low DM host contribution, along with an approximately zero RM (McKinven & Chime/Frb Collaboration, 2022; Zhang et al., 2023a; Feng et al., 2023; Hewitt et al., 2023), corroborates the hypothesis of a clean local environment (Hewitt et al., 2023).

In this work, we report the first multi-wavelength monitoring campaign of FRB 20220912A, carried out at 408 MHz with the NC radio telescope, at 1.4 GHz with The Mc 32-m radio telescope and at X and γ rays with the The Neil Gehrels Swift Observatory (Swift) (Gehrels et al., 2004) and AGILE (Tavani et al., 2009) satellites. Furthermore, we use new deep continuum radio observations taken with the uGMRT at band 5 (1.0 – 1.4 GHz) to investigate the presence of a PRS in the direction of FRB 20220912A.

The Chapter is structured as follows. In Section 4.3 we describe the multi-wavelength campaign conducted on FRB 20220912A. In Section 4.4, we describe and discuss the results of the observations. Finally, we present our conclusions in Section 4.5.

4.3 Observations

4.3.1 Northern Cross radio telescope

The NC telescope configuration used in this Chapter has two differences with respect to observations presented in Trudu et al. (2022) and Pelliciari et al. (2023b) (Chapter 3). First, it doubles the collecting area, combining sixteen cylinders of the North-South arm into a single beam, whose half-power beam width is now $1.6^{\circ} \times 0.25^{\circ}$. Second, the delay correction needed to form the beam is performed at higher cadence, namely every 5 s, effectively tracking the source across the field of view. Observations are stored to disk as 16-bit SIGPROC (Lorimer, 2011) filterbank files, with a time resolution of 138.24 μ s and a 14.468 kHz frequency channel width (see Locatelli et al., 2020, for a detailed description of the system).

We started monitoring FRB 20220912A with eight cylinders on 16 October 2022, forming a single beam at the source coordinates, R.A. $(J2000) = 23^h\,09^m\,04.9^s$, Dec $(J2000) = +48^\circ\,42'\,25.4''$ (Ravi et al., 2023). After the first 14 hours on-source, the observations were interrupted and resumed on 17 May 2023, when 16 cylinders were employed. Observations ended on 31 December 2023, for a total of 122 hr on-source. Each session of observation lasted for ~ 35 min. As in Trudu et al. (2022) and Pelliciari et al. (2023b), we performed a weekly calibration through interferometric observations of Cas A. A summary of the conducted observations is shown in Fig. 4.1.

4.3.2 Medicina "Grueff" radio telescope

Simultaneous observations were carried out at 1.4 GHz (L band) with the 32-m Mc radio telescope. The total duration of the campaign was 177 hours, made of ~ 1 hr daily runs. We recorded the 2-bit baseband data in both circular polarisations written to disk in VDIF format (Whitney et al., 2010), using the local digital baseband converter (DBBC) system (Tuccari, 2003). Observations are centred at 1414 MHz, sampling a 128 MHz bandwidth divided into four separated sub-bands. Data were converted to filterbank format using a custom-built pipeline (Kirsten et al., 2020) and stored to disk with a 250 kHz frequency and 64 μ s time resolution

Table 4.1: Burst properties at 408 MHz from FRB 20220912A. Columns are, from left to right, the burst ID, the barycentric arrival time (B.A.T) at infinite frequency expressed as the MJD, the fit-optimised DM, the FWHM duration, the peak flux density, the fluence, the spectral energy and the isotropic burst energy, the latter computed multiplying the spectral energy for 16 MHz, i.e. the bandwidth used in NC observations.

ID	TOA	DM	Width	$F_{\rm peak}$	F	E_{ν}	E_i
	(B.A.T.)	$(pc cm^{-3})$	(ms)	(Jy)	(Jy ms)	$(10^{30} \text{ erg Hz}^{-1})$	(10^{37} erg)
B01	59868.885988115	219.6(5)	4.1(5)	18(1)	74(5)	12.3(7)	20(1)
B02	60125.160302085	220.2(3)	3.1(4)	7.4(6)	23(2)	3.8(3)	6.1(5)
B03	60133.142754625	220.1(2)	9.4(6)	4.3(4)	40(4)	6.7(5)	10.7(8)
B04	60136.132478465	219.6(4)	4.1(6)	6.8(6)	28(2)	4.6(4)	7.4(6)
B05	60138.120952875	219.7(6)	16(2)	4.8(3)	77(5)	12.8(7)	20(1)
B06	60140.121695755	220.4(2)	3.4(4)	7.6(6)	26(2)	4.3(3)	6.9(5)
B07	60160.070367215	220.1(2)	1.4(2)	9(1)	13(2)	2.1(3)	3.4(5)
B08	60165.061278865	219.4(3)	5.2(8)	7.3(6)	38(3)	6.3(5)	10.1(8)
B09	60166.045907535	219.9(2)	3.2(5)	6.2(6)	24(2)	3.3(4)	5.3(6)
B10	60166.045908315	219.7(2)	3.1(4)	5.5(7)	20(2)	2.8(3)	4.5(5)
B11	60173.031215725	221.3(5)	14.6(8)	10.1(3)	147(5)	24.5(6)	40(1)
B12	60178.024922305	220.1(4)	2.9(1)	29.9(7)	86(2)	14.4(3)	23.1(5)
B13	60182.006531445	220.2(2)	4.3(3)	13.3(6)	57(3)	9.5(4)	15.2(6)
B14	60211.931989265	220(1)	4.3(6)	4.9(5)	21(3)	3.5(4)	5.6(6)
B15	60215.918013385	220.8(4)	6.8(7)	6.5(4)	44(3)	7.3(5)	11.8(8)
B16	60218.898463655	223(1)	10(2)	3.8(4)	38(5)	6.3(8)	10(1)

respectively. Two circular polarisations were averaged together to obtain total intensity data. The telescope has a SEFD of 458 Jy at 1.4 GHz, which leads (using the radiometer equation) to a result of $\sigma_L \simeq 1.2$ Jy ms root mean square (rms) noise for a burst of 1 ms of duration. To test the data acquisition and conversion we observed PSR B0329+54 and we successfully detected single pulses on this basis.

4.3.3 uGMRT

To search for a PRS coincident to the position of FRB 20220912A, continuum radio observations of FRB 20220912A were performed with the uGMRT in the 1050-1450 MHz (band-5) frequency range on 2023 November 1st. The total bandwidth was split into 16384 channels of 24.414 kHz each. The field of FRB 20220912A was observed for a total of ~ 3 hours. The sources 3C48 and J2322+509, a nearby source to the target, were used as absolute flux scale and phase calibrators, respectively.

The high spectral resolution of our data enabled us to split the total bandwidth in eight sub-bands of 50 MHz each for easier data reduction. We processed each sub-band independently by carrying out a standard interferometric data reduction¹ using the Common Astronomy Software Applications (CASA; McMullin et al., 2007) package. We iteratively performed flagging of RFI, bandpass, amplitude and phase calibrations for each sub-band. Finally, the calibrated visibilities of all the sub-bands were recombined for imaging. We assumed 3C48 to be 17.7 Jy at 1.2 GHz, with a spectral index $\beta = -0.76$ (Perley & Butler, 2013). These measurements were used for the 3C48 flux and bandpass calibrations, which were then transferred to J2322+509. Finally, we determined gain and phase calibration for J2322+509 and then transferred them to the target field. Owing to severe RFI, two out of eight sub-bands were flagged, thus leaving

 $^{^{1}} See \ https://science.nrao.edu/facilities/vla/docs/manuals/obsguide/topical-guides/lofrequents/facilities/vla/docs/manuals/obsguide/topical-guides/lofrequents/facilities/vla/docs/manuals/obsguide/topical-guides/lofrequents/facilities/vla/docs/manuals/obsguide/topical-guides/lofrequents/facilities/vla/docs/manuals/obsguide/topical-guides/lofrequents/facilities/vla/docs/manuals/obsguide/topical-guides/lofrequents/facilities/vla/docs/manuals/obsguide/topical-guides/lofrequents/facilities/vla/docs/manuals/obsguide/topical-guides/lofrequents/facilities/vla/docs/manuals/obsguide/topical-guides/lofrequents/facilities/vla/docs/manuals/obsguide/topical-guides/lofrequents/facilities/vla/docs/manuals/obsguide/topical-guides/lofrequents/facilities/vla/docs/manuals/obsguide/topical-guides/lofrequents/facilities/vla/docs/manuals/obsguide/topical-guides/lofrequents/facilities/vla/docs/manuals/obsguide/topical-guides/lofrequents/facilities/vla/docs/manuals/obsguides/facilities/vla/docs/manuals/obsguides/facilities/vla/docs/manuals/obsguides/facilities/vla/docs/manuals/obsguides/facilities/vla/docs/manuals/obsguides/facilities/vla/docs/manuals/obsguides/facilities/vla/docs/manuals/obsguides/facilities/vla/docs/manuals/obsguides/facilities/vla/docs/manuals/obsguides/facilities/vla/docs/manuals/obsguides/facilities/vla/docs/manuals/obsguides/facilities/vla/docs/manuals/obsguides/facilities/vla/docs/manuals/obsguides/facilities/vla/docs/manuals/obsguides/facilities/vla/docs/manuals/obsguides/facilities/vla/docs/manuals/obsguides/facilitie$

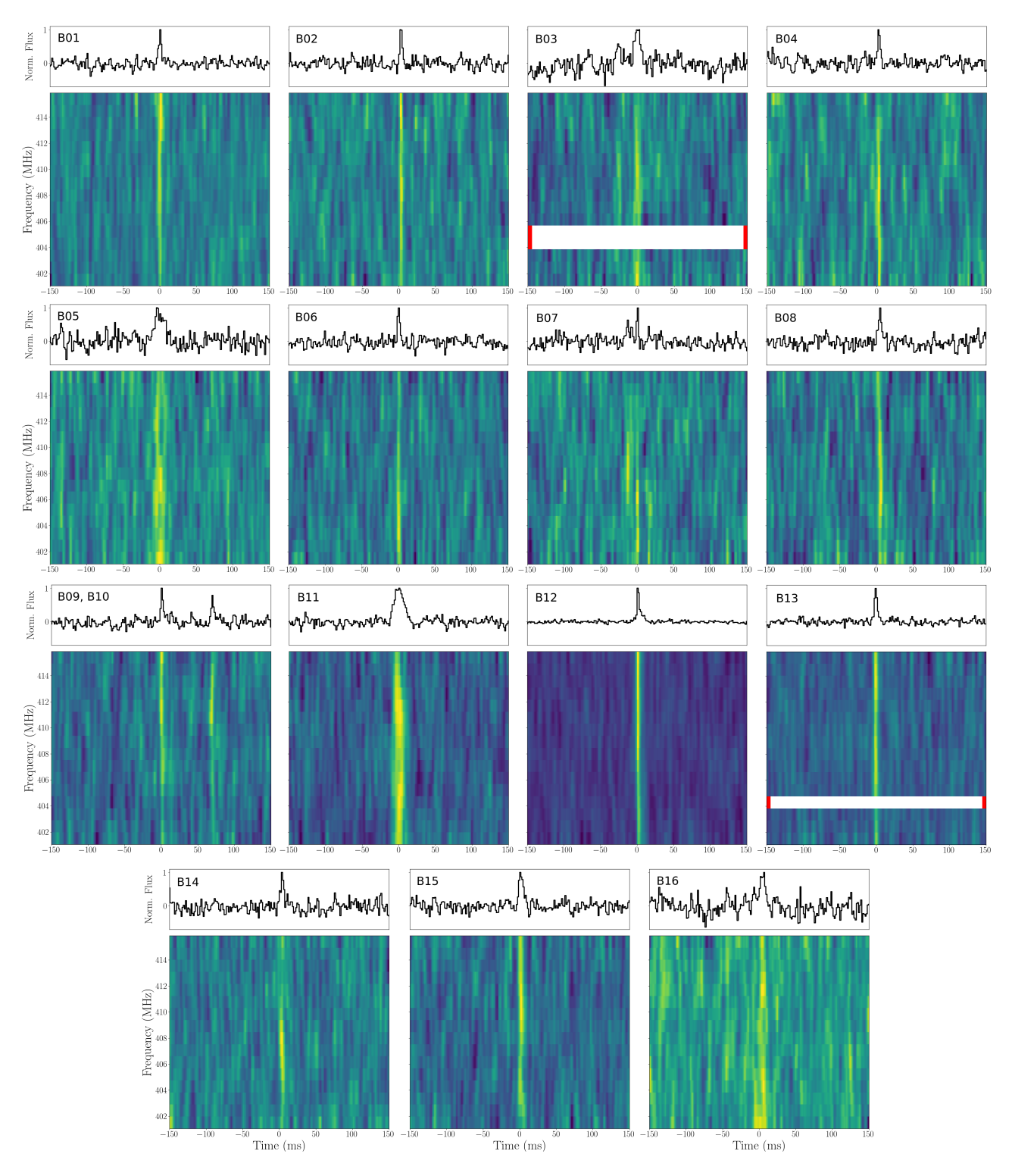


Figure 4.2: Bursts from FRB 20220912A observed at 408 MHz. Both the de-dispersed, dynamic spectrum (bottom sub-panels) and the frequency-averaged profiles (top sub-panels) are shown. For a better visualisation, the data were down-sampled to have 16 frequency channels (each 1 MHz wide) and time bins 1.5 ms in width. Horizontal white rows (highlighted with red ticks) are flagged channels due to RFI.

300 MHz of remaining bandwidth. Imaging was carried out with the TCLEAN task in CASA, by weighting the visibilities according to the briggs scheme with a ROBUST parameter -1. We achieved a final noise level of $36 \mu Jy$ beam⁻¹ at an angular resolution of $1.97'' \times 1.77''$.

4.3.4 Swift and AGILE monitoring

Since its discovery (McKinven & Chime/Frb Collaboration, 2022), FRB 20220912A has been added to the AGILE list of sources monitored during the Spinning-mode observations. We verified the source exposure with the MiniCalorimeter (MCAL; $0.4\,\mathrm{MeV} \leq E \leq 100\,\mathrm{MeV}$) detector and the AGILE gamma-ray imaging detector (GRID; $30\,\mathrm{MeV} \leq E \leq 30\,\mathrm{GeV}$). We took the de-dispersed topocentric arrival times at infinite frequencies as the arrival time for each burst. AGILE acquired MCAL data covering 3 of the 16 bursts presented here, due to the South Atlantic Anomaly (SAA) passages or Earth occultation. We selected good events with standard selection criteria, such as the SAA passages time intervals exclusion, along with the inclusion of events with off-axis angles smaller than 60 degrees or at angles from Earth direction greater than 80 degrees.

A monitoring campaign with Swift was also started in autumn 2022, similar to the one dedicated to FRB 20180916B (partially reported in Tavani et al., 2020; Trudu et al., 2023). Swift observed FRB 20220912A with the X-ray Telescope (XRT, Burrows et al., 2005), as one of the three instruments on board. The Swift/XRT X-ray (0.3–10 keV) data were obtained daily after time of opportunity requests during source activity phases (on November 2022, and July-October, 2023, partially covering the radio monitoring presented in this work). The XRT observations were carried out in windowed timing (WT) readout mode, with 2–10 daily pointings. The time resolution of WT data is 1.8 ms and each pointing has a typical exposure of ~ 1.8 ks. We considered the combination of all the data and processed them using the XRTDAS software package (v.3.7.0)² within the HEASoft package (v.6.32.1). We cleaned and calibrated the data with standard filtering criteria using the xrtpipeline task and the calibration files available from the Swift/XRT CALDB (version 20230705). The imaging analysis was executed selecting events in the energy channels between 0.3 and 10 keV and within a 20 pixel ($\sim 47''$) radius, including the 90% of the point-spread function. The background was estimated from a nearby source-free circular region with the same radius value.

4.4 Results and discussion

The search for FRB candidates in NC data follows the strategy employed in Trudu et al. (2022) and Pelliciari et al. (2023b), using the SPANDAK pipeline (Gajjar et al., 2018), which flags RFIs through RFIFIND (Ransom et al., 2002) and searches for single pulses with HEIMDALL (Barsdell et al., 2012). We considered a S/N greater than 8 and a boxcar width shorter than 35 ms. We carried out our search using DM between 200 pc cm⁻³ and 240 pc cm⁻³, given the nominal 220 pc cm⁻³ DM of the source. In the case of observations at 1.4 GHz, we set the threshold S/N > 10, to minimise the RFI contamination. To cross-check the results of the single-pulse search conducted at 1.4 GHz with the pipeline described above, we searched for FRBs in a large amount of data also with the processing pipeline described in Kirsten et al. (2021, 2024), which searches FRB with HEIMDALL and classifies bursts with the deep learning classifier FETCH (Agarwal et al., 2020). We estimated the completeness of our observations at both 408 MHz and 1.4 GHz via injections of simulated burst. We used FRB-FAKER³ (Houben et al., 2019) to inject 100 bursts of 1 ms duration with a DM of 220 pc cm⁻³ at random times.

²developed by the ASI Space Science Data Center (SSDC)

³https://gitlab.com/houben.ljm/frb-faker

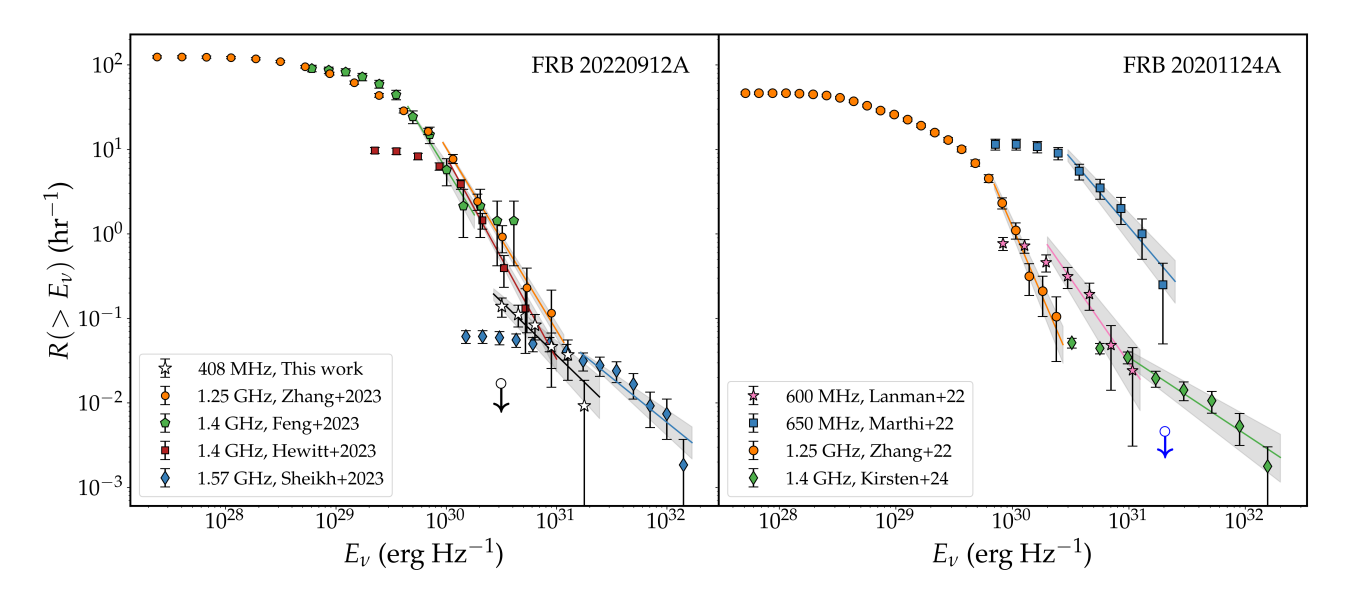


Figure 4.3: Comparison between the cumulative spectral energy rate distribution for two hyperactive repeaters at different observing frequencies and times. Left: FRB 20220912A at 408 MHz (white stars; this work), 1.25 GHz (orange circles; Zhang et al., 2023a), 1.4 GHz (green pentagons and red squares; Feng et al., 2023; Hewitt et al., 2024) and 1.572 GHz (blue diamonds; Sheikh et al., 2023). The 95% C.L. UL for $R(E_{\nu} > 2.5 \times 10^{30} \, \mathrm{erg \ Hz^{-1}})$ from our 1.4 GHz observations is plotted as a black downward arrow. Right: FRB 20201124A at 600 MHz (pink stars; Lanman et al., 2022), 650 MHz (blue squares; Marthi et al., 2022), 1.25 GHz (orange circles; Zhang et al., 2022) and 1.4 GHz (green diamonds; Kirsten et al., 2024). The 95% C.L. UL for $R(E_{\nu} > 2 \times 10^{31} \, \mathrm{erg \ Hz^{-1}})$ from P (334 MHz) resulting from non-detections in Kirsten et al. (2024), is plotted as a blue downward arrows.

We varied the S/N of the injected burst between 5 and 20 and we ran the same pipeline used for the search in order to retrieve the injected bursts. We find a 95% completeness for a fluence of 17 and 20 Jy ms at 408 MHz and 1.4 GHz respectively.

We detected a total of 16 bursts at 408 MHz and labeled them as "Bn", then ordered them according to their time of arrival (ToA). We show their dynamic, de-dispersed spectra in Fig. 4.2, while their measured properties are reported in Table 4.1. All radio bursts, except for the first one, B01, were detected during the second period of the campaign (i.e. later than May $17^{\rm th}$, 2023) when 16 cylinders were used. We fit a Gaussian profile to the de-dispersed FRB spectrum, integrated over the burst profile, and found that the full width at half maximum (FWHM) of all bursts are compatible with the 16 MHz bandwidth, apart from B14, whose extensions is only ~ 6 MHz. Furthermore, we found no evidence of scattering and sub-burst structures on time scales larger than 138.24 μ s for any of the detected burst.

Given the S/N of a burst, we computed its fluence as the product of its peak flux density F_{peak} and its FWHM duration w, where the former is obtained as (Lorimer & Kramer, 2004):

$$F_{\text{peak}} = \text{S/N} \frac{\text{SEFD}}{A\sqrt{N_p N_c (1 - \xi) \Delta \nu_{\text{ch}} w}} \zeta(\text{ToA}). \tag{4.1}$$

Here, SEFD = 8400 Jy (Trudu et al., 2022) holds for each receiver (i.e., each group of sixteen dipoles), $N_p = 1$ is the number of polarisations, $N_c = 1024$ is the number of spectral channels and $\Delta\nu_{\rm ch} = 14.4$ kHz the channel width. Furthermore, A is the number of receivers included in either the eight (A = 32) or sixteen (A = 64) cylinders, ξ is the fraction of channels excised by RFIs, and, finally, the attenuation of the primary beam at the burst ToA is given by ζ (ToA) (Trudu et al., 2022; Pelliciari et al., 2023b).

Given the burst fluence, we computed the corresponding burst spectral energy E_{ν} :

$$E_{\nu} = 10^{30} \frac{4\pi}{(1+z)^2} \left(\frac{D_L}{10^{28} \text{ cm}}\right)^2 \left(\frac{\mathcal{F}}{\text{Jy ms}}\right) \text{ erg Hz}^{-1}.$$
 (4.2)

Here the burst isotropic energy is E_i (e.g. Macquart & Ekers, 2018b; Chawla et al., 2022) per unit bandwidth. Also, $D_L = 380.86$ Mpc is the luminosity distance of the source, obtained considering z = 0.0771, the redshift of the source, and the Planck 2015 cosmology (Planck Collaboration et al., 2016).

We computed the cumulative spectral energy rate $R(>E_{\nu})$ at 408 MHz. We plot it in Fig. 4.3, together with spectral energies from literature observations⁴. It follows a power law in the $3 \times 10^{30} < E_{\nu} < 3 \times 10^{31}$ erg Hz⁻¹ range:

$$R(>E_{\nu}) = R_0(>E_{\nu,0}) \left(\frac{E_{\nu}}{E_{\nu,0}}\right)^{\alpha_E},$$
 (4.3)

where $E_{\nu,0}=3\times 10^{30}$ erg Hz⁻¹. As a reference, the NC 95% completeness fluence limit corresponds to 3×10^{30} erg Hz⁻¹. We found the best fit values to be $R_0=0.19\pm 0.03~{\rm hr}^{-1}$ and $\alpha_E=-1.3\pm 0.2$, respectively. We do not report any detections at 1.4 GHz, from which we placed a 95% C.L. upper limit (UL) of 0.017 hr⁻¹ on the burst rate at 1.4 GHz for $\mathcal{F}\geq 20~{\rm Jy}$ ms (corresponding to $E_{\nu}=3.2\times 10^{30}~{\rm erg~Hz}^{-1}$).

We repeated the analysis for FRB 20201124Å⁵, another very actively repeating FRB source (Xu et al., 2022; Zhang et al., 2022). The resulting distributions are shown in Fig. 4.3, while the best fit parameters obtained for each observation are listed in Table 4.2.

The cumulative spectral energy rates are fairly similar between FRBs 20220912A and 20201124A, both in the range of the energetic and the repetition rate. This could be an indication that these two sources share the same emission mechanism (James et al., 2020), as also highlighted by other similarities such as their reported double-peaked waiting time distribution and complex time-frequency structures of their bursts (see e.g. Zhang et al., 2022, 2023a). Regarding FRB 20220912A, the repetition rate for bursts having $E_{\nu} \geq 2 \times 10^{30}$ erg Hz⁻¹ decreased from $\sim 10 \text{ hr}^{-1}$ (Zhang et al., 2023a; Feng et al., 2023) during a storm event, to $\sim 0.1 \text{ hr}^{-1}$, approximately two months later (Sheikh et al., 2023), when the storm ended. Lastly, it dropped to less than 0.017 hr⁻¹ nearly a year later, as we could see from our 1.4 GHz monitoring (see Fig. 4.3). However, the source remained active at 408 MHz, exhibiting comparable levels of repetition rate to those reported by Sheikh et al. (2023). FRB 20220912A is, as far as we know, the only FRB source that shows a decline of more than four orders of magnitude in its burst rate in the L band.

A similar behaviour, albeit inverted in frequency, can be seen for FRB 20201124A, where the burst rate dropped from $\sim 0.2~\rm hr^{-1}$ as reported at $550-750~\rm MHz$ observations (Marthi et al., 2022) to $< 5 \times 10^{-3}~\rm hr^{-1}$ at $(2 \times 10^{31}~\rm erg~\rm Hz^{-1})$, as resulting from non-detections at 334 MHz in $\sim 650~\rm hr$ of observing time (Kirsten et al., 2024). To obtain the minimum spectral energy corresponding to the latter observational campaign, we used equation 4.2, considering the 91 Jy ms completeness fluence reported in Kirsten et al. (2024).

Interestingly, we note the same flattening of the cumulative spectral energy rate distribution for high energetic bursts as the one previously reported for R1 (Hewitt et al., 2022; Jahns et al., 2023) and, more recently, for FRB 20201124A (Kirsten et al., 2024). As can be noted also from the best fit values obtained for α_E in Table 4.2, the case for FRB 20220912A is particularly

⁴Isotropic energies are obtained by multiplying the spectral energies for 16 MHz at 408 MHz and 64 MHz at 1.4 GHz, respectively.

⁵We considered a redshift z = 0.098 (Kilpatrick et al., 2021), corresponding to a luminosity distance $D_L = 453.3$ Mpc (Zhang et al., 2022).

Table 4.2: Parameters obtained from the power-law fitting of the cumulative energy distributions for FRBs 20220912A and 20201124A. The first column represents the spectral energy threshold over which data no longer follow a simple power law, the second and third column represent the best-fit values for the parameters of the fitting power-law function (equation 4.3). The references for the data that we used to compute the cumulative burst rate distributions are listed in the last column.

$E_{\nu,0} \ (10^{30} \ {\rm erg \ Hz^{-1}})$	$R_0 \; ({\rm hr}^{-1})$	α_E	Ref.				
	FRB 20220912A						
1	20.5 ± 3	-2.13 ± 0.3	Feng et al. (2023)				
1	10.5 ± 1.5	-2.15 ± 0.01	Zhang et al. (2023a)				
2	1.51 ± 0.2	-2.4 ± 0.2	Hewitt et al. (2024)				
3	0.19 ± 0.03	-1.3 ± 0.2	This work				
25	0.036 ± 0.007	-1.03 ± 0.3	Sheikh et al. (2023)				
	FRB 20	201124A					
0.5	6.8 ± 0.5	-2.5 ± 0.2	Zhang et al. (2022)				
2	0.74 ± 0.18	-2.0 ± 0.3	Lanman et al. (2022)				
3	9 ± 2	-1.7 ± 0.3	Marthi et al. (2022)				
10	0.035 ± 0.01	-0.96 ± 0.2	Kirsten et al. (2024)				

similar to FRB 20201124A. We note that α_E shifts from approximately -2 for $E_{\nu} \geq 10^{30}$ erg Hz⁻¹ to roughly -1 at $E_{\nu} \simeq 2 \times 10^{31}$ erg Hz⁻¹. Moreover, high energetic bursts present a slope $\alpha_E = -1.03 \pm 0.3$, obtained by analysing L band data from Sheikh et al. (2023), which is fully consistent with the power law slope, α_E , obtained by fitting the cumulative luminosity distribution of apparently non-repeating FRBs (James et al., 2022a,b; Shin et al., 2023). As a reference, James et al. (2022a) obtained $\alpha_E = -0.95^{+0.18}_{-0.15}$, but the other measurements are still consistent with this value. Regarding R1, the cumulative isotropic energy distribution flattens to $\alpha_E = -0.88 \pm 0.01$ for $E_{\rm iso} \geq 1.3 \times 10^{38}$ erg (Jahns et al., 2023). This value for α_E roughly agrees with other reported values as obtained by fitting the R1 cumulative energy distribution at high energies (Law et al., 2017; Gourdji et al., 2019; Cruces et al., 2021; Hewitt et al., 2022). Even if the cumulative slopes are similar to the case of FRBs 20220912A and 20201124A, we note that $E_{\rm iso} = 1.3 \times 10^{38}$ erg corresponds to a spectral energy of $^6 \sim 4 \times 10^{29}$ erg Hz⁻¹, which is approximately one order of magnitude lower than the break spectral energy we obtained for the other two repeaters.

4.4.1 Constraints on broad-band spectral index

No multi-band observations of FRB 20220912A have been reported yet. However, from a period of burst storm detected by the Five-hundred-meter Aperture Spherical Telescope (FAST), Zhang et al. (2023a) obtained a synthetic L band (1-1.5 GHz) spectral index of -2.6 ± 0.21 (Zhang et al., 2023a). This value was derived by fitting a spectrum obtained by averaging the fluence of all their reported bursts, characterised by having single narrow-band spectra with emission occurring only over 20% of the observing bandwidth (Zhang et al., 2023a), in different frequency channels. Although this is a valid way to obtain an in-band spectral index, we suggest some caution when making a direct comparison between an UL on the broad-band spectral index and the in-band β value obtained in Zhang et al. (2023a). Indeed, our observations probe the broad-band spectrum of the source, which can be obtained only when considering simultaneous bursts arriving at separate frequency bands.

⁶We divided the break istropic energy as reported in Jahns et al. (2023) by 450 MHz, i.e. an average effective bandwidth as reported therein. This value for the break spectral energy agrees well with what reported in Hewitt et al. (2022), when considering a bandwidth of 275 MHz.

Table 4.3: ULs on fluence and broad-band spectral index β for Mc radio telescope observations for which there is a simultaneous burst detection at 408 MHz from NC radio telescope. The second and third columns represent the limits on fluence and broad-band spectral index, respectively. The former represent the 2σ detection threshold, where σ is the Mc radio telescope rms noise computed on a sample of data of duration τ , with τ the FWHM of the given burst as observed at 408 MHz.

Burst ID	$\mathcal{F}_{1.4} (2\sigma, \text{ Jy ms})$	β
B08	< 6.3	< -1.6
B09	< 4.9	< -1.4
B10	< 4.8	< -1.1
B11	< 10.1	< -2.3
B12	< 4.4	< -2.3
B13	< 5.5	< -1.9

During our observational campaign, a total of six bursts (B08-B13) have been detected in the P band during simultaneous L band observations of which we do not report any counterpart. Henceforth, we use these non-detections to provide ULs on the L band fluence of these bursts, which (in turn) imply ULs on the FRB 20220912A broad-band (408 MHz – 1.4 GHz) spectral index. For each detected burst with an L band simultaneous observation we computed the fluence UL using the radiometer equation (4.1), considering the same width of the corresponding burst in the P band. We considered a 2σ detection threshold in this case, since our goal has not been to search for bursts blindly with HEIMDALL, which has a minimum S/N search of ~ 6 . Instead, we manually inspected the Mc radio telescope data at burst topocentric arrival times, after correcting them for the DM of the bursts. The brightest burst we detected during our campaign is B11, with a measured fluence $F = 145 \pm 4.6$ Jy ms at 408 MHz. We do not report any significant radio emission down to 2σ at 1.4 GHz and this translates into a fluence UL of 10.1 Jy ms in the L band for a burst having a 14.6 ms duration. This UL translates into $\beta < -2.3$. The same limit on β is obtained by the non-detection of an L band counterpart for B12, which has an high S/N as well but with a $\times 10$ shorter duration than B11. We report all the ULs obtained from our observations in Table 4.3.

Our non-detections in the L band undermine the hypothesis of a positive (or flat) broad-band spectral radio emission. We find our UL on β in disagreement with $\beta=2.1$, as measured for a burst from R1 in the multi-frequency, Arecibo (1.4 GHz) – VLA (3 GHz) campaign; namely, this is the only simultaneous FRB detection present in the literature (Law et al., 2017). The other bursts reported in Law et al. (2017) have not been detected simultaneously by the two observatories, showing that the broad-band spectral behaviour of the source cannot simply be modelled by a power law function. Moreover, also a spectrum with $\beta \sim 1$ as the one measured from FRB 20200428, the Galactic FRB, simultaneously detected by CHIME at 600 MHz CHIME/FRB Collaboration et al. (2020) and STARE2 at 1.4 GHz (Bochenek et al., 2020) can be ruled out based on our observations. Therefore, our UL could imply either that FRB 20220912A is characterised by a steep radio spectrum or it could be a consequence of its intrinsically narrow-band emission (Zhang et al., 2023a; Feng et al., 2023; Sheikh et al., 2023).

Our UL is somewhat inconsistent with the very flat spectrum usually observed for radio-loud magnetars (Camilo et al., 2008; Lazaridis et al., 2008; Dai et al., 2019); however, large fluctuations in the spectral index are observed locally in magnetars, for instance, in the case of XTE J1810–197 (Lazaridis et al., 2008; Maan et al., 2022). An interesting exception is the radio-loud magnetar Swift J1818.0–1607, which has shown emission in a steep spectrum with $\beta \simeq -2.26$ (Lower et al., 2022). A broad-band emission with this spectral index seems to be disfavoured by our observations. Nevertheless, we must be careful in comparing the spectral index for radio-loud magnetars and FRBs, since (up to now) the former showed only

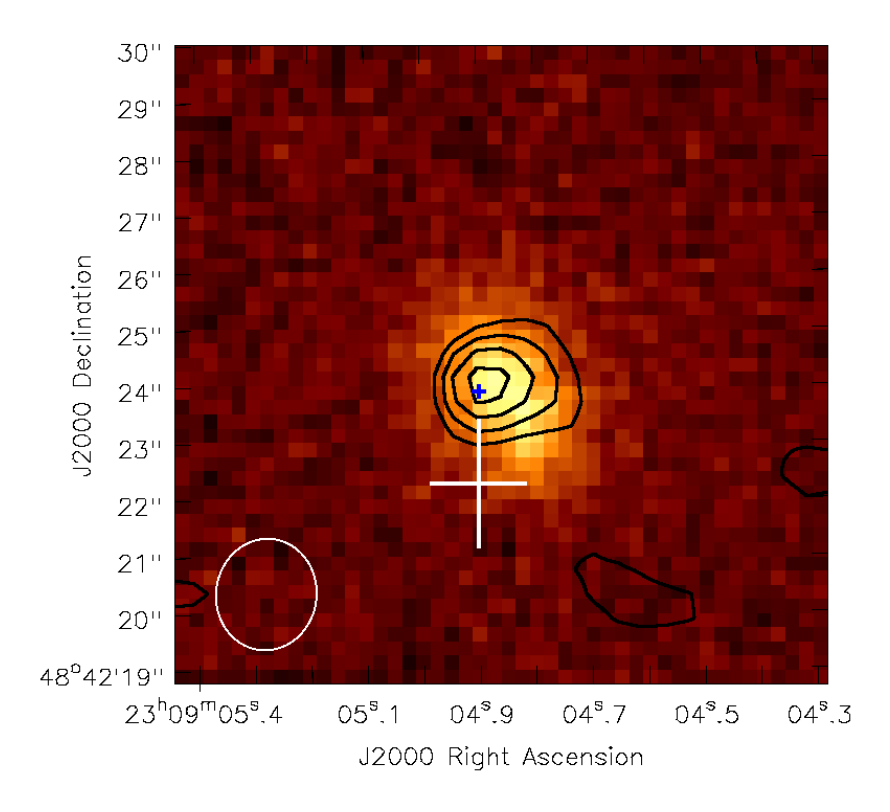


Figure 4.4: Optical Pan-STARRS (i filter) image of PSO J347.2702+48.7066, the host galaxy of FRB 20220912A, with contour levels representing the continuum radio source we detected at 1.26 GHz, with a 1.97" \times 1.77" synthesised beam. Contours are drawn from three to six times the rms noise level $\sigma \simeq 36~\mu \rm Jy~beam^{-1}$. The white cross represents the position of the APTF J23 radio source, with the cross extensions corresponding to 1σ uncertainties on its centroid (Hewitt et al., 2024), while the blue cross indicates the position of FRB 20220912A localised at milliarcsecond angular resolution (Hewitt et al., 2024). The synthesised beam of our uGMRT observations is represented in the bottom left corner of the image as a white ellipse.

pulsed emission (but see also Esposito et al., 2020). The only two exceptions to date are SGR J1935+2154 (CHIME/FRB Collaboration et al., 2020; Bochenek et al., 2020; Zhang et al., 2020; Kirsten et al., 2021; Good & CHIME/FRB Collaboration, 2020) and 1E 1547.0–5408 (Israel et al., 2021), which also showed FRB-like bursts, before entering a pulsar-like phase (Zhu et al., 2023). For the former, FRB-like bursts are emitted in random phases (unlike radio pulsations, which instead arrive in a phase windows anti-aligned with X-ray pulsations), hinting at different emission mechanisms between radio pulses and FRB-like bursts (Zhu et al., 2023). For 1E 1547.0–5408, rather, FRB-like bursts are not aligned in phase with radio pulsations, nor with X-ray bursts (Israel et al., 2021).

4.4.2 Continuum radio emission from FRB 20220912A host galaxy

In our uGMRT image at 1.26 GHz, we detect a continuum source spatially coincident with the coordinates of PSO J347.2702+48.7066, the host galaxy of FRB 20220912A. The source integrated and peak flux densities are consistent at 1σ level; thus, we considered it as unresolved in our observations. Its centroid has coordinates R.A. (J2000) = $23^{\rm h}09^{\rm m}04.88^{\rm s} \pm 0.017$ s, Dec. (J2000) = $+48^{\circ}42'24.04'' \pm 0.25''$. Such position is well in agreement with R.A. (J2000) = $23^{\rm h}09^{\rm m}04.8988^{\rm s} \pm 0.0003$ s, Dec. (J2000) = $+48^{\circ}42'23.9078'' \pm 0.005''$, namely the localisation of FRB 20220912A obtained from European VLBI Network (EVN) observations (Hewitt et al., 2024). The radio contours of the source we detect are shown in Fig. 4.4, as well as the VLBI localisation of the FRB. In the same figure, the optical image taken from the Panoramic Survey

Table 4.4: AGILE FRB 20220912A bursts coverage and MCAL ULs. The second and fourth columns report the presence or absence of the source in the field of view (FoV) of the two onboard detectors here considered, respectively. In the third column we report the existence of an MCAL data acquisition at trigger time. MCAL fluence 3σ ULs in 0.4-30 MeV band are evaluated only when no coincident data acquisitions at the burst times is present; MCAL trigger "False Alarm Rate" (FAR) are evaluated when coincident data acquisition is present. ULs (1 ms) refer to the UL fluences that would be required to issue a trigger with the onboard 1 ms MCAL trigger logic timescale (see Ursi et al., 2022a). Since there is no evidence of a detection in the acquired triggers, we checked in the 100 days preceding each burst time to estimate the FAR corresponding to each trigger.

	MOAT	MOAT	CDID	TTT	MOAT	TIT
Burst	MCAL	MCAL	GRID	UL	MCAL	UL
ID	FoV	D.A.	FoV	(3σ)	trigger FAR	$1 \mathrm{\ ms}$
				$[{\rm erg}~{\rm cm}^{-2}]$	$[\mathrm{evt/hour}]$	$[{\rm erg}~{\rm cm}^{-2}]$
B01				idle mode		
B02	YES	NO	NO	_	_	3.22×10^{-8}
B03				idle mode		
B04	YES	NO	NO	_	_	2.59×10^{-8}
B05	YES	NO	YES	_	_	1.84×10^{-8}
B06	YES	NO	NO	_	_	5.15×10^{-8}
B07				no data		
B08	YES	NO	NO	_	_	4.22×10^{-8}
B09	YES	YES	NO	2.06×10^{-7}	~ 4.0	_
B10	YES	YES	NO	2.04×10^{-7}	~ 4.0	_
B11	YES	YES	NO	2.00×10^{-7}	~ 4.0	_
B12	YES	NO	NO	_	_	2.17×10^{-8}
B13				idle mode		
B14				idle mode		
B15	YES	NO	YES	_	_	1.83×10^{-8}
B16				no data		

Telescope & Rapid Response System (Pan-STARRS) data archive 1 (PS1; Flewelling et al., 2020) is shown.

We measured a flux density of $240 \pm 36~\mu Jy$ at 1.26 GHz, which corresponds to a spectral luminosity of $L_{\nu} \simeq 4 \times 10^{28}~{\rm erg~s^{-1}~Hz^{-1}}$. We are aware that EVN observations ruled out the presence of a PRS surrounding FRB 20220912A at milliarcsecond scale for an rms of 16 μJy beam⁻¹, placing an UL of $1.2 \times 10^{28}~{\rm erg~s^{-1}~Hz^{-1}}$ on its spectral luminosity at 1.4 GHz (Hewitt et al., 2024). In the same work, a continuum radio source, APTF J230904+484222 (APTF J23), detected by the Westerbork Synthesis Radio Telescope Aperture Tile In Focus (WSRT-APERTIF) has been reported, with a position consistent with the coordinates of FRB 20220912A host galaxy. This source has a peak flux density of $270 \pm 40~\mu Jy$ beam⁻¹, which falls within the measured flux range of our source, considering the associated uncertainties. Although APTF J23 is offset by $\sim 1.6''$ with respect to the FRB VLBI position (see Fig. 4.4), the $\sim 2''$ uncertainties associated to its centroid makes APTF J23 consistent at 2σ level with the position of our detected source. We thus conclude that the source we detect and APTF J23 are the same radio source, albeit observed in this work with an improved spatial resolution by a factor of four.

Finally, we note that the contour levels of the PRS we are aiming to detect are offset by approximately 0.6" (about 0.9 kpc in physical size) from the geometric centre of the host galaxy. This offset lowers the plausibility that an active galactic nucleus (AGN) is the origin of this source and, instead, suggests that the radio emission is originating from a star formation region in the vicinity of FRB 20220912A.

Table 4.5: Swift exposures and flux ULs (0.3-10 keV).

Start time	Stop time	UL
(UTC)		$[{\rm erg}\ {\rm cm}^{-2}{\rm s}^{-1}]$
2022-11-11 19:26:15	2022-11-20 18:29:56	2.3×10^{-13}
2023-07-25 00:09:32	2023-07-30 02:47:55	2.5×10^{-13}
2023-08-29 21:26:07	2023-09-09 21:01:56	2.1×10^{-13}
2023-09-29 22:27:14	2023-10-05 21:30:56	4.9×10^{-13}

4.4.3 Results from the high energy monitoring of FRB 20220912A

As a first step, we checked the burst exposures in the AGILE source monitoring, as well as the position of the source within the AGILE FoV at each burst time. The relative AGILE exposure to the source is reported in Table 4.4. We obtained a coverage of three of the observed bursts with MCAL data but no detection was found analysing the light curves in five binnings (16, 32, 64, 256 ms, and 1 s) and considering shifts of 1/4 of bin (four shifts for the first two time scales, two for the second two). We extracted a 3σ C.L. fluence ULs in 0.4-30 MeV energy band considering a cut-off power-law model, with a photon index of -0.70 and cut-off energy of 65 keV (as reported for the FRB 200428 burst by Mereghetti et al., 2020). We also estimated UL fluences that would be required to issue a trigger with the onboard 1 ms MCAL trigger logic timescale (see Ursi et al., 2022b). We report the corresponding ULs in Table 4.4. These MCAL UL values are somewhat lower than the similar values previously published (see for instance Trudu et al., 2023), thanks to the non-standard spectral model applied in this work. The most stringent UL that we can place on the radio efficiency $\eta = E_{\gamma}/E_{\rm Radio}$ is from burst B05, for which the non-activation of the MCAL trigger system permits us to obtain $\eta < 1.5 \times 10^9$ at 3σ C.L. in the 0.4-30 MeV energy range. We conclude that observations in this work confirm the exclusion of giant X-ray flares as possible X-ray countepart of B05. Moreover, we set an UL value on η consistent with those previously reported for one-off and repeater sources (see, e.g., Figure 3 from Pearlman et al., 2023, and references therein). We note that our UL for η is conservative. Indeed, η depends on the radio isotropic energy of the burst, which in turn relies on the spectral occupancy. In our case, we considered $\Delta \nu = 16$ MHz, which is the observed bandwidth of the NC radio telescope, but the unknown intrinsic spectral width of the burst likely exceeds this value, and it could allow tighter constraints to be placed on η .

AGILE/GRID covered 2 of the 16 bursts (B05 and B15) at their ToA. We analysed GRID data near burst arrival times on short (100 s around the bursts), and longer timescales (±10 days and 100 days starting about B05 trigger time). The long-timescale data analysis was performed applying the standard AGILE multi-source maximum likelihood (AML; Bulgarelli et al., 2012), which is mainly applied to exposures longer than a few hours. We report no detection at short timescales for AGILE/GRID. Finally, we extracted 3 σ ULs in the E \geq 100 MeV band for two long time integrations, 10 days after each burst and 100 days after burst B05 (the latter period of time includes also B15). We obtained UL_{10d} = 2.0 × 10⁻¹¹ erg cm⁻² s⁻¹ and UL_{100d} = 4.4 × 10⁻¹² erg cm⁻² s⁻¹. From the latter, we obtained $L_{\gamma} < 7.1 \times 10^{43}$ erg s⁻¹ for the persistent γ -ray luminosity of the source.

No X-ray source was detected at $> 3\sigma$ C.L. in the whole Swift/XRT WT mode dataset. We note however, with a detailed single observation check, that no radio burst was exposed even including three more proposals acquired in photon counting (PC) mode: burst B01 occurred 16 hrs after the observation on October 16th, 2022, while B16 occurred within our third observations but did not fall within the WT mode sky window. We then extracted a 3σ countrate ULs for our observations using the XIMAGE package (sosta command) and converted to fluxes using a standard single power-law spectral model with a photon index of 2.0, and correcting for

absorption for a column density of N_H fixed to the Galactic value of $1.43 \times 10^{21} \text{cm}^{-2}$ (HI4PI Collaboration et al., 2016) corrected for the redshift of the source (Ravi et al., 2023). The X-ray observations exposure and the corresponding ULs for the persistent X-ray fluence are reported in Table 4.5. From the latter, we obtained an UL for the persistent X-ray luminosity $L_X = 4\pi D_L^2 F_X/(1+z) < 3.4 \times 10^{42} \text{ erg s}^{-1}$, where D_L is the luminosity distance of FRB 20220912A. We note that this UL excludes the majority of mid- and high-luminosity AGNs, which typically have X-ray luminosity $L_X \geq 10^{43} \text{ erg s}^{-1}$ (e.g. Padovani et al., 2017). This offers further evidence that the radio source detected with uGMRT (see Section 4.4.2) originates from a region of star formation, rather than from an AGN.

4.5 Summary and conclusions

In this work, we present a campaign of simultaneous observations at 408 MHz and 1.4 GHz, taken with the NC and Mc radio telescopes, respectively, of one of the most active repeaters known to date: FRB 20220912A. During the campaign, we detected 16 bursts from FRB 20220912A at 408 MHz. We found that the cumulative burst rate as a function of the spectral energy at 408 MHz can be aptly fitted with a single power-law function $R(>E_{\nu}) \propto E_{\nu}^{\alpha_E}$, with $\alpha_E = -1.3 \pm 0.2$. We do not report any burst detection at 1.4 GHz in a total of 177 hr above a fluence and a spectral energy threshold of $\mathcal{F} > 20$ Jy ms and 3.2×10^{30} erg Hz⁻¹, respectively. These non-detections place an UL of 0.017 hr⁻¹ at 95% C.L for the burst rate at 1.4 GHz, which is about four orders of magnitude lower than the level of activity reported at the same frequency during a burst storm of the source (Zhang et al., 2023a; Feng et al., 2023) at the same spectral energy. On the other hand, the source remained active at 408 MHz with comparable repetition rate as observed from a long monitoring after the end of the burst storm (Sheikh et al., 2023). Interestingly, we note that the cumulative spectral energy rate distribution of FRB 20220912A flattens for bursts having a spectral energy of $E_{\nu} \geq 10^{31} \text{ erg Hz}^{-1}$, changing slope from approximately $\alpha_E \approx -2$ to $\alpha_E \approx -1$. This flattening feature has been reported so far for two other well-studied hyperactive repeaters, R1 (Hewitt et al., 2022; Jahns et al., 2023) and FRB 20201124A (Kirsten et al., 2024). As discussed in Kirsten et al. (2024), this could be linked to a different type of emission mechanism, emission site or beaming angle between low and high energy bursts. This could potentially represent a link between one-off bursts and repeating sources (James et al., 2022b; Kirsten et al., 2024). The fact that also FRB 20220912A shows this kind of behaviour, combined with the fact that high energy bursts present a slope that is amply consistent with that of the non-repeaters population (James et al., 2022a,b; Shin et al., 2023), provides further support to the idea that a fraction of apparently non-repeating FRBs could (instead) be repeating sources with very low repetition rates (Ravi, 2019; James, 2023). We compared the cumulative spectral energy rate for FRB 20220912A and FRB 20201124A, highlighting a strong similarity between the two distributions, both in terms of the spectral energy and repetition rate ranges.

In total, 6 of the 16 bursts detected at 408 MHz arrived during simultaneous observations at 1.4 GHz, allowing us to place the first ULs to the broad-band (408 MHz – 1.4 GHz) spectral index β of FRB 20220912A. Analysing the Mc data at the ToA of burst B11, which has the highest fluence, we obtained an UL of β < –2.3, indicating that the source (under the assumption of an intrinsically broad-band emission) exhibits a very steep spectral index. Our observations then strongly disfavor a flat or even inverted spectrum for FRB 20220912A. We note that this is different than what has been reported for the only two simultaneous detections of FRBs in separate frequency bands, the latter indicating a positive spectral index (Law et al., 2017; Bochenek et al., 2020; CHIME/FRB Collaboration et al., 2020). Our findings support the idea that the intrinsic spectrum of FRB 20220912A's bursts is narrow-band, as reported in recent

observations (Zhang et al., 2023a; Feng et al., 2023; Sheikh et al., 2023; Hewitt et al., 2024).

Additionally, we reported three-hour-long continuum radio observations of FRB 20220912A field using the band 5 (1050-1450 MHz) of the uGMRT. We detected a continuum radio source of $240\pm40~\mu\mathrm{Jy}$ flux density that is spatially coincident with the FRB 20220912A VLBI localisation. Given it has not been detected in recent, deep, EVN observations (Hewitt et al., 2024), we suggest that this continuum radio source may possibly originate from a region of star formation, potentially located in the vicinity of the FRB source. This is corroborated by the 0.6" offset (0.9 kpc in physical size) between the source centroid and the geometric centre of the optical host galaxy, which excludes the hypothesis that the radio source is being powered by an AGN.

Finally, we report the results of an X- and γ -ray monitoring of FRB 20220912A with the Swift and AGILE space missions in X- and γ rays, respectively. We reported no detection for either of these high-energy campaigns. Regarding AGILE, we placed an UL on the radio efficiency of $\eta = E_{\gamma}/E_{\rm radio} < 1.5 \times 10^9$ for the B05 burst, consistent with literature ULs from one-off sources and repeaters (Pearlman et al., 2023), along with a persistent γ -ray luminosity UL of $L_{\gamma} < 7.1 \times 10^{43}$ erg s⁻¹. From Swift observations we obtained instead a UL for the persistent X-ray luminosity (0.3 – 10 keV) of $L_{X} < 3.4 \times 10^{42}$ erg s⁻¹.

Appendix A. Multi-wavelength follow up of new CHIME repeaters

The extensive observing time available with the NC is ideal for monitoring FRB sources, particularly for studying the physical properties of active repeaters. For this reason, in addition to the observations mentioned in this Chapter and in Chapter 3, further monitoring of other FRB sources has been carried out and continues nowadays. One example is FRB 20240114A, one of the newest discovered repeaters from CHIME/FRB (Shin & CHIME/FRB Collaboration, 2024), which soon after its discovery showed hyper-activity (e.g. Uttarkar et al., 2024; Ould-Boukattine et al., 2024). As done for FRB 20220912A, we started monitoring this source right after its discovery, collecting two burst detections at 408 MHz (Pelliciari et al., 2024b,c), shown in Figure 4.5. As evident from the Figure, while the burst on the left presents a single, Gaussian-shaped burst component, the one on the right presents multiple sub-burst components. The main one (labelled as C1 in Figure 4.5) has a FWHM duration of 1.8 ms and a fluence of 124.3 ± 1.5 Jy ms. The second component (C2) arrives ~ 7.5 ms before C1, has a 1.9 ms duration, and a fluence of 24.6 ± 1.5 Jy ms. We also note a third, faint component (C3) arriving 3 ms after C1. with a duration of 1 ms. Interestingly, this composite burst has been simultaneously detected by Westerbork RT-1 at a central frequency of 328 MHz (Ould-Boukattine et al., 2024). The total burst bandwidth probed by this simultaneous detection is 116 MHz, still consistent with the observed bandwidth of repeaters (see, e.g., Pleunis et al., 2021b). Moreover, our two burst detections have been used in Kumar et al. (2024a), to reveal a potential quenching of the source emission at low frequency after an initial period of activity.

Apart from FRB 20240114A, observations of NC are often complemented by observations at higher frequencies through observations requests with the Mc, Noto, and Sardinia radio telescopes. Thus, in addition to the goal of studying how the activity of a source varies through long and repeated observations, there is also the aim of investigating the spectral properties of FRBs, which are still not well understood.

In particular, Chime/Frb Collaboration et al. (2023) reported the discovery of 25 repeating sources (gold sample) along with 14 repeater candidates (silver sample). Among the gold sample, many repeaters present high repetition rates. We conducted a multiwavelenght P-L band monitoring of the most promising sources of the gold sample, in terms of repetition rate.

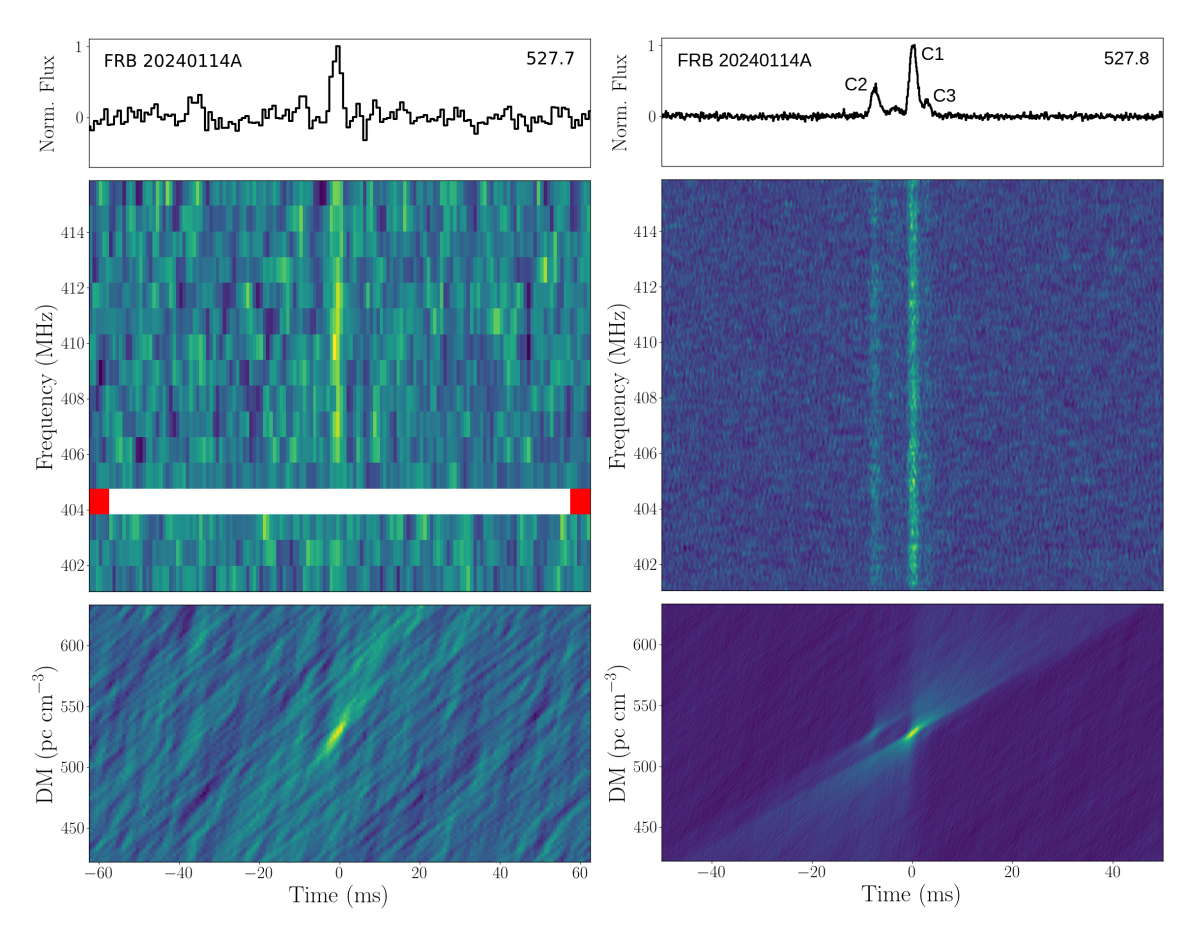


Figure 4.5: Burst detections of FRB 20240114A at 408 MHz with the Northern Cross radio telescope. For each plot, the upper sub-panel shows the frequency-averaged time-series, the central sub-panel shows the dynamic spectrum, incoherently de-dispersed at the DM reported in the upper right corner of the plot, and the lower sub-panel shows the butterfly DM-time plot.

For these observations we used the same obervational setup as described in Section 4.3. In particular we selected FRBs 20201130A, 201909915D and 20200929C. Additionally, we monitored four repeater candidates from the silver sample only at P-band with the NC radio telescope. The latter are FRBs 20190303D, 20190812A, 20200320A and 20210323C. We list their principal observational properties in Table 4.6, along with the total exposure time spent on each source with the NC and Mc radio telescopes. Similarly with what has been done for FRB 20220912A, we searched for burst candidates using Heimdall/SPANDAK pipelines in a Δ DM = 100 pc cm⁻³ range around their reported DM (Chime/Frb Collaboration et al., 2023). We do not report any burst detection from these sources, neither at P nor at L-band. These non-detections permit us to update the previously known repetition rates at P-band in the case of NC observations, and place the first ULs on the rate at L-band.

For each source selected from the CHIME sample, we estimate its expected repetition rate for a radio telescope x, where x = NC (Northern Cross) and x = Mc (Medicina), by scaling properly the reported CHIME burst rate ($R_{\rm CH}$) (Chime/Frb Collaboration et al., 2023) for fluence distribution power law index, α , and a spectral index, β , as:

$$R_x = R_{\rm CH} \left(\frac{\nu_x}{\nu_{\rm CH}}\right)^{\beta} \left(\frac{F_x^{\rm th}}{F_{\rm CH}^{\rm th}}\right)^{\alpha} \, {\rm hr}^{-1},\tag{4.4}$$

where $\nu_{\rm NC}=0.4$ GHz, $\nu_{\rm G}=1.4$ GHz and $\nu_{\rm CH}=0.6$ GHz are the central observing frequencies for NC, Mc and CHIME radio telescopes, respectively. We considered the following fluence thresholds: $F_{\rm NC}^{\rm th}=20$ Jy ms, $F_{\rm G}^{\rm th}=12.8$ Jy ms and $F_{\rm CH}^{\rm th}=5$ Jy ms (CHIME/FRB Collaboration

ULs on the repetition rate and the ULs at 95% C.L. to the energy distribution power law index α obtained from equation 4.4. Table 4.6: Properties of the monitored FRBs selected from Chime/Frb Collaboration et al. (2023). Columns list: source names following the Transient Name Server (TNS) convention, DMs, total exposure times spent on source with the NC and Mc (underscore Mc), the associated 95% C.L. (Gehrels, 1986)

Source name	$DM (pc cm^{-3})$	$T_{ m NC}~({ m hr})$	T_{Mc} (hr)	$DM (pc cm^{-3}) T_{NC} (hr) T_{Mc} (hr) R_{NC} (> 20 Jy ms, hr^{-1}) R_{NC}$	$R_{\rm Mc}~(>12.8~{\rm Jy~ms,~hr^{-1}})$	$lpha_{ m NC}$	$lpha_{ m Mc}$
20201130A(g)	287.984(7)	28.1	44	< 0.11	< 0.06	< -1.3	< -0.35
20190915D(g)	488.69(2)	50.7	51	< 0.07	< 0.05	< -0.8	< 0.5
20200929C(g)	479.602(9)	10.5	31.6	< 0.28	< 0.09 - < 1.75	1	< 1.75
20190303D(s)	714.552(8)	96.8	ı	< 0.03	ı	1	ı
20200320A(s)	593.524(2)	27.6	ı	< 0.11	ı	1	ı
20190812A(s)	252.889(2)	87.4	I	< 0.01	ı	1	ı
20210323C(s)	288.6(3)	39.7	ı	< 0.08	ı	1	ı

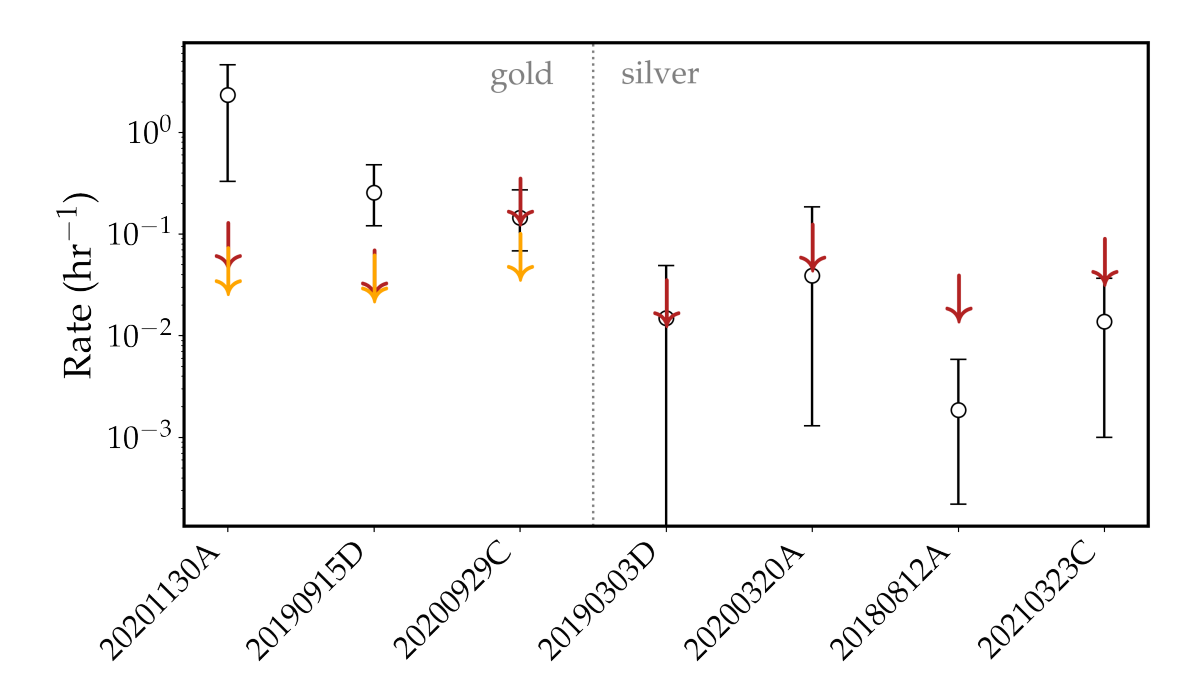


Figure 4.6: Burst rates for 7 repeating FRB sources. White circles represent the burst rates as reported in Chime/Frb Collaboration et al. (2023), with error bars representing the 1σ uncertainties. Downward red (yellow) arrows represent the ULs for each source as obtained from our NC (Mc) monitoring.

et al., 2021; Chime/Frb Collaboration et al., 2023). These repetition rates depend strongly on β , the spectral index, which is highly unknown and can vary from source to source (see Section 4.4.1). We assume a fiducial $\beta = -1.6$ as measured for 23 FRBs with the Australian Square Kilometer Array Pathfinder (ASKAP) (Macquart et al., 2020a). All the ULs obtained from our monitoring at P and L bands are shown in Fig. 4.6 and are listed in Table 4.6.

Regarding NC observations, we obtained tighter constraints than CHIME for the two most active gold-sample repeaters, i.e. FRBs 20201130A and 20190915D. In particular, we obtain ~ 20 and ~ 4 times deeper constraints than Chime/Frb Collaboration et al. (2023) on the repetition rate of FRB 20201130A and FRB 20190915D, respectively. The same holds for Mc radio telescope observations, for which we obtained comparable constraints for the gold sample FRBs.

These constraints permit us to place ULs on the slope of the fluence distribution α using equation 4.4, and using the rates in Chime/Frb Collaboration et al. (2023). The most stringent constraint we derive is for FRB 20201130A, the most active FRB source within the gold sample, for which we obtain $\alpha < -1.3$ from our NC monitoring on this source. This indicates that, in order to explain the non-detections at 408 MHz, the fluence distribution of this source must be steeper than this value for α or that the activity level of the source changed by a factor of ~ 20 since its detection. All the relevant lower limits on α that we derived from our monitoring are listed in Table 4.6. Our findings indicate that, in general, repeating FRB sources can exhibit very low repetition rates, making them appear similar to one-off events. This could be due to periods of inactivity or generally low activity levels in these sources. Consequently, this suggests that, at least observationally, the distinction between repeating and one-off FRBs may not be as clear-cut. In fact, some one-off events might eventually repeat if observed for a sufficiently long time, as already pointed out (see, e.g. James, 2023).

Chapter 5

The impact of calibration errors on the FRB localisation using VLBI observations

5.1 Introduction

FRB searches were, for a long time, carried out with single dish telescopes, which offered limited localisation capabilities. Radio interferometric arrays were not suited for FRB observations for a variety of reasons: their standard correlator mode operations do not provide sufficient time resolution to observe ms-long transients; their field of view is often small and, therefore, not suited for blind transient searches; they are often oversubscribed.

The discovery of repeating FRBs and the increase in computing infrastructure for the newest generation of radio interferometers, enabled interferometric observations of FRBs. The position of the first repeating FRBs were measured with a precision of ~ 5 mas (e.g. Marcote et al., 2017), a factor of $\sim 10^5$ improvement on the single dish observations, compared to FAST observing at 1.4 GHz as a reference example.

Accurate localisations of FRBs have become more frequent when interferometers with large instantaneous field of view have become operational: single telescope voltages are captured at high time resolution and combined together in either an incoherent or a coherent mode, searching for FRBs over a large fraction of the field of view. In the case of a detection in this so-called tied-array beam mode, voltages from the individual telescopes are cross-correlated in order to take advantage of the interferometric angular resolution in the localisation of the event (e.g., Michilli et al., 2021; Bezuidenhout et al., 2023; Shannon et al., 2024).

Amongst the localisation techniques, the PRECISE project (Marcote et al., 2022) holds a special place as it uses a sub-set of the EVN array to observe repeating FRBs and pinpoint their position with accuracies ranging between 1 and 6 milliarcseconds (Kirsten et al., 2022a; Nimmo et al., 2022a; Bhandari et al., 2023; Hewitt et al., 2024). At the redshift values of the known repeaters, they correspond to linear distances between 3 and 20 pc (see, e.g. Bhandari et al., 2023).

Some important results prior to PRECISE played a key role in its development, particularly in the localisation of FRBs within their host galaxies, i.e. to a more specific local environment. The association between R1 and a star forming region provided further association between FRBs and magnetars born via the CCSN mechanism (Marcote et al., 2020). Moreover, the same source was associated to a PRS, which resulted unresolved at milli-arcsecond scales from VLBI observations (Marcote et al., 2020). The localisation of R3 at the edge of a star forming region permitted important constraints on the age of the source and its possible formation scenarios (Marcote et al., 2017; Tendulkar et al., 2021). However, the association between FRB 20200120E and a GC in M81 was largely unexpected and provided evidence for an alternative mechanism of magnetar (or FRB) formation (Kirsten et al., 2022a).

The accuracy of localisations obtained via PRECISE (or PRECISE-like) observations is crucial to the association with the local environment (e.g., a star forming region or a GC) and the uncertainties on such measurements have been sufficiently small not to hinder such associations (Marcote et al., 2020; Kirsten et al., 2022a). So far, no assessment of the impact of calibration errors on the FRB localisation has been made. In this chapter we investigate this topic, simulating the impact that calibration errors may have on PRECISE-like observations, in particular if they jeopardize the association within the host galaxy environment. The Chapter is divided as follows. In section 5.2 I provide and overview of VLBI observations and their calibration; the analysis and calibration of an actual observation of the active repeater R1 is presented in Section 5.3. Simulations of PRECISE-like observations of FRBs are presented in Section 5.4, together with the simulation of their calibration errors. Conclusions are offered in Section 5.5.

5.2 Elements of interferometry and VLBI

The angular resolution θ_b of a single dish observation is defined by the known diffraction pattern:

$$\theta_{\rm b} \simeq \frac{\lambda}{D},$$
 (5.1)

where λ is the observing wavelength and D is the telescope diameter. The historical quest for higher and higher angular resolution could not be met by larger and larger telescopes, due to practical and cost limitations in building telescopes with diameter larger than a few hundreds meters.

Radio interferometers historically overcame these limitations by cross correlating the outputs of several individual telescopes in order to "synthesize" a single dish of equivalent aperture diameter corresponding to the maximum separation between the telescopes D'.

The most basic radio interferometer is a simple 2-element interferometer, where the signals between two antennas are cross correlated to produce the complex-valued visibility function V:

$$V(u,v) = V_0 e^{-i\phi} \propto \int_{\Omega} B(\ell,m) e^{2\pi i (u\ell + vm)} d\ell dm, \qquad (5.2)$$

where (u, v) are the coordinates in the so-called (u, v) plane, B is the sky brightness distribution, (ℓ, m) are the sky directions expressed in the so-called "direction cosines" (see, e.g., Thompson et al., 2017a). The geometric relationships between the (u, v) and the (l, m) coordinates is illustrated in Figure 5.1. Equation 5.2 shows that an interferometer measures the two dimensional Fourier transform of the sky brightness distribution. If a sufficient number of (u, v) points area measured, then the sky brightness distribution can be reconstructed via Fourier inversion:

$$B(\ell, m) = \int V(u, v) e^{-2\pi i(u\ell + vm)} du dv.$$

$$(5.3)$$

An appropriate sampling of the uv plane is achieved in two ways: by increasing the number of antennas to be cross-correlated and by allowing their relative position to change with respect to the source as the Earth rotates (the principle called "Earth rotation synthesis"). Figure 5.2 shows an example of uv plane sampling.

Visibilities measured in actual observations, however, are always corrupted by a certain number of instrumental effects that need to be corrected in post-processing through calibration.

The standard assumption in calibration is that the observed visibilities V^{o} can be related to the intrinsic (or model) visibilities as (e.g., Hamaker et al., 1996; Smirnov, 2011):

$$\mathbf{V}_{ij}^{\mathrm{o}} = \mathbf{G}_i \, \tilde{\mathbf{V}}_{ij} \, \mathbf{G}_i^{\dagger} \tag{5.4}$$

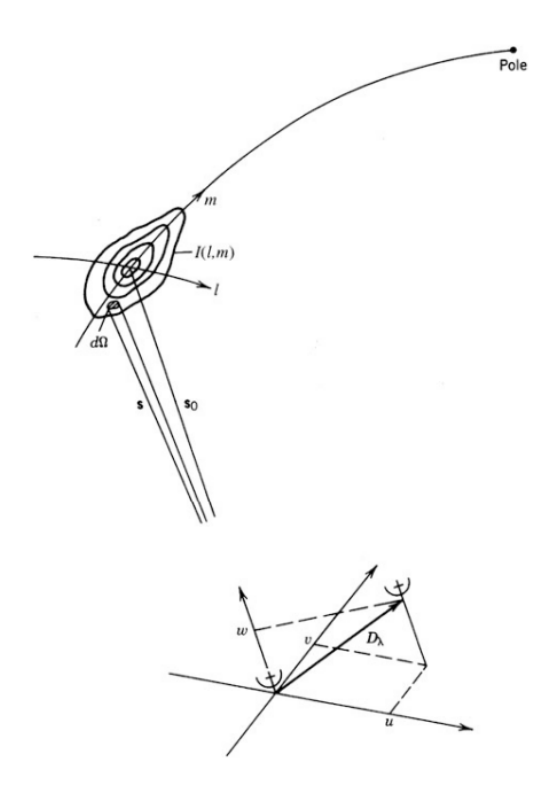


Figure 5.1: Relationship between the (u, v) and the (l, m) set of coordinates. Here the baseline between the two antennas has length D_{λ} and components (u, v, w), where w is pointing towards the source. The latter has intensity distribution I(l, m). The coordinate system (l, m) corresponds to the projection of a sphere onto a plane tangential to the center of the field target. Credits to Thompson et al. (2017b).

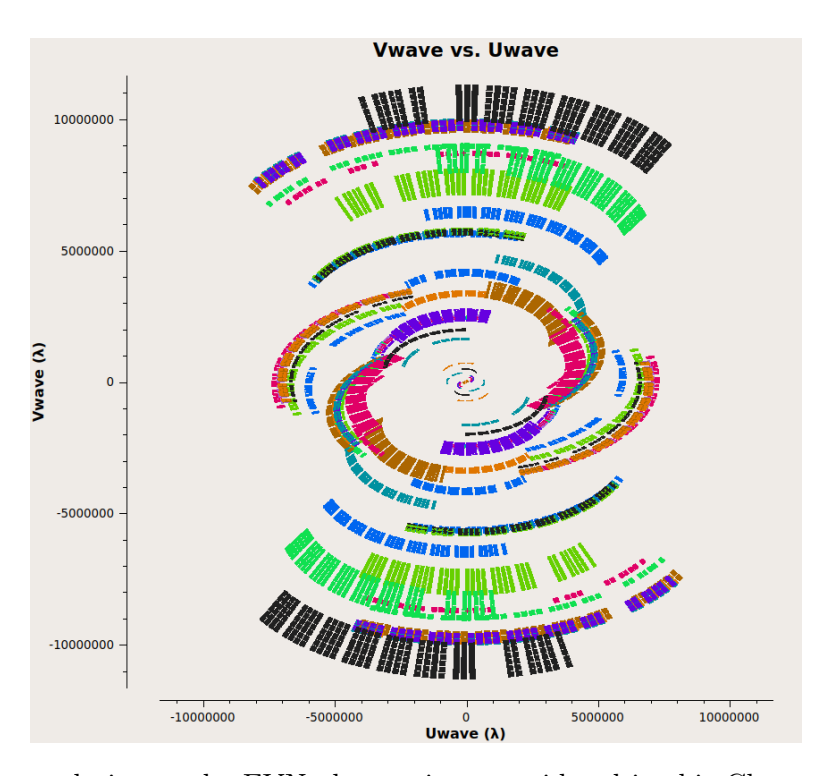


Figure 5.2: *uv*-plane relative to the EVN observations considered in this Chapter (see Section 5.3), conducted on R1 (i.e. the target of these observations). The plot is colored by baselines. The radial direction of the points in the plot represents the spectral extension of the visibilities, while the tracks in the tangential direction are due to the Earth rotation.

where G are the so called Jones matrices that describe the instrumental corruptions along the telescope receiving chains. Boldface indicates 2×2 matrix quantities, that describe the four polarization cross-products that can be measured by dual polarization receivers. The single-polarization form of equation 5.4 becomes:

$$V_{ij}^{\text{o}} = g_i \, g_j^* \, \tilde{V}_{ij}. \tag{5.5}$$

Different instrumental effects can be expressed by different Jones matrices and this approach is particularly useful when the dependence upon the physical parameters is not correlated. For example, the frequency response of an antenna (also referred to as the bandpass) depends essentially upon the receiver electronics (low noise amplifiers and filters) and is generally stable in time, therefore the associated Jones ${\bf B}$ matrix will only depend upon frequency and can be solved for just one time throughout an observation. Conversely, temperature changes in the ambient induce temporal variations in the receiving response and, therefore, the associated Jones matrix ${\bf J}$ will be time dependent. The general Jones matrix ${\bf G}$ of equation 5.4 can be factorized as:

$$\mathbf{G}_i(\nu, t) = \mathbf{B}_i(\nu) \,\mathbf{J}_i(t). \tag{5.6}$$

Calibration observations take advantage of these assumptions. For example, an observing run generally begins with a short (10-20 minutes) observation of a bright, unresolved source of known flux density and spectrum that is used to solve for the bandpass **B**. The run is also usually interspersed by observations of a secondary calibrator: a moderately bright source as close as possible to the target in order to be able to calibrate both the receiver gain variations and the time fluctuations of the atmospheric phase variations. The contribution to the temporal variation of the visibility phase indeed mostly comes from atmospheric fluctuations and are one of the prominent corruptions in very long baseline observations (e.g., Rogers et al., 1984; Asaki et al., 1996; Jung et al., 2008). Under the assumption that amplitude gains are not affected by instrumental effects or, in other words, that the corruption of visibility phases are essentially due to gain phases, equation 5.5 can be written as:

$$\tilde{v}_{ij} e^{i\phi_{ij}^0(t,\nu)} = e^{i\psi_i(t,\nu)} e^{-i\psi_j(t,\nu)} \tilde{v}_{ij} e^{i\tilde{\phi}_{ij}(t,\nu)},$$
(5.7)

$$e^{i\phi_{ij}^0(t,\nu)} = e^{i\psi_i(t,\nu)} e^{-i\psi_j(t,\nu)} e^{i\tilde{\phi}_{ij}(t,\nu)},$$
 (5.8)

which leads to:

$$\phi_{0,ij}(t,\nu) = \tilde{\phi}_{ij}(t,\nu) + \psi_i(t,\nu) - \psi_j(t,\nu), \tag{5.9}$$

where \tilde{v}_{ij} is the amplitude of the intrisinc visibilities between antenna i and j, ϕ_{ij}^0 is the phase of the observed visibility, ψ_i and ψ_j are the gain phases and $\tilde{\phi}_{ij}$ is the intrinsic phase visibility. The phase term $\psi_i(t,\nu)$ relative to antenna i can approximated as:

$$\psi_i(t,\nu) \simeq \psi_i(t_r,\nu_r) + \frac{\partial \psi_i}{\partial \nu} \Delta \nu + \frac{\partial \psi_i}{\partial t} \Delta t$$
 (5.10)

where $\Delta t = t - t_r$, $\Delta \nu = \nu - \nu_r$ are referred to a reference time t_r and a reference frequency ν_r , respectively. Following Petrov et al. (2011) we define:

$$\psi_{i,0} = \psi_i(t_r, \nu_r)
\tau_i = \frac{\partial \psi_i}{\partial \nu}(t_r, \nu_r)
\tau_i = \frac{\partial \psi_i}{\partial t}(t_r, \nu_r) .$$
(5.11)

where $\psi_{i,0}$ is also referred to as the "peculiar" phase of the antenna i, τ is a delay term and r indicates the rate at which the delays change with time. Therefore, equation (5.10) can be



Figure 5.3: The EVN. In this Chapter we analyse an observation taken with a subset of the entire EVN, comprising 12 antennas.

expressed as:

$$\tilde{\phi}_{ij}(t,\nu) = \phi_{ij}(t,\nu) + (\psi_{i,0} - \psi_{j,0}) + \Delta\nu(\tau_i - \tau_j) + \Delta t(r_i - r_j) . \tag{5.12}$$

The calibration of VLBI observations relies on finding solutions for the unknown terms of equation 5.12 for each antenna, i.e. ψ_0 , τ and ν . This is also the case for our observations. Visibility amplitudes can also be calibrated using an astronomical source, however, for some science applications, it is sufficient to apply the system temperature corrections recorded throughout the observations by the individual telescopes. Equation 5.12 is implemented in the CASA task FRINGEFIT, that we used in our observations.

5.2.1 The European VLBI Network

The EVN is a network of radio telescopes operated by the Joint Institute of VLBI ERIC (JIVE) and located primarily in Europe and Asia (Figure 5.3): Badary (32 m, Russia), Effelsberg (100 m, Germany), Hartebeesthoek (26 m, South Africa), Irbene (32 m, Latvia), Kunming (40 m, China), Lovell (76 m, England), Medicina (32 m, Italy), Metsähovi (14 m, Finland), Noto (32 m, Italy), Onsala (O8: 25 m, O6: 20 m, Sweden), Sardinia (64 m, Italy), Sheshan (25 m, China), Svetloe (32 m, Russia), Tianma (65 m, China), Torun (32 m, Poland), Urumqi (25 m, China), Westerbork (25 m, The Netherlands), Yebes (40 m, Spain), Zelenchukskaya (32 m, Russia). The frequency coverage ranges from 0.3 to 49 GHz, even though not all the antennas are available at each frequency. The maximum baseline is 9833 km (Badary-Hartebeesthoek). The synthesised beam size is between 24 mas (0.3 GHz) and 0.19 mas (43 GHz). The lack of short baselines which samples the diffuse emission can be partially solved by including the e-MERLIN in the EVN observation. Before its collapse, the Arecibo radio telescope (305 m, Puerto Rico) was part of the EVN. Even though in standard VLBI the data are recorded on disks at the stations and then shipped to the a central correlator for processing, EVN is capable of real-time correlation with the e-VLBI technique, which uses fibre optic networks to connect EVN telescopes to the JIVE data processor that correlates the data in real-time. Presently, the EVN is the most sensitive VLBI array and the only one capable of real-time observations.

5.3 Very long baseline observations of the R1 FRB

We analysed observations of R1 taken on September 22 2022, from 0^h till 6^h UT (project ID ek051e, PI: Kirsten) as part of the PRECISE project¹. During the observations a total of 13 antennas were used: Effelsberg (Ef), Toruń (Tr), Westerbork single-dish RT1 (Wb), Noto (Nt), Onsala (O8), Medicina (Mc), and single-dishes from eMERLIN, i.e. Cambridge (Cm), Darnhall (Da)², Defford (De), Knockin (Kn), Pickmere (Pi), Jodrell Bank Mark II (Jm). Observations were carried out at 1.4 GHz, with a different bandwidth for each telescope (see Table 5.1 for details). The pointing coordinates were $\alpha_{J2000} = 5^{\rm h} 31^{\rm m} 58.7^{\rm s}$ and $\delta_{J2000} = +33^{\circ} 8' 52.57''$, consistent with the VLBI localisation of R1 and its PRS (Marcote et al., 2017). The source J1829+4844 was observed as a bandpass/fringe-finder calibrator and assumed to have a 13.08 Jy flux density at 1.4 GHz with a $\alpha = -0.79$ spectral index (Perley & Butler, 2017). The source J0529+3209 was observed as a secondary calibrator, alternated to the target, for 6 minutes for each time slot. Eventually, J0541+3301 was observed as a backup source. The target source, R1, was observed for a total of 3.46 hours.

Antenna ID	$\nu_{\rm low} ({\rm GHz})$	$\nu_{\rm high}~({\rm GHz})$	$n_{\rm spw}$
Ef	1.26	1.51	8
Tr	1.26	1.51	8
O8	1.26	1.51	8
Nt	1.32	1.51	6
Wb	1.32	1.44	4
Mc	1.35	1.47	4
Cm	1.29	1.35	2
Du	1.29	1.35	2
Da	1.35	1.41	2
Kn	1.35	1.41	2
Pi	1.35	1.41	2
De	1.29	1.35	2
$_{ m Jm}$	1.35	1.41	2

Table 5.1: Spectral coverage of each EVN dish in the array we used for our PRECISE observation. The first column represents the antenna ID, the second and third columns are the lowest and highest frequencies recorded by each antenna, respectively, and the last column is the number of spectral windows recorded. Each spectral window has a bandwidth of 32 MHz apart from eMERLIN antennas which have 64 MHz bandwidths.

Visibilities were generated using the SFXC software correlator (Keimpema et al., 2015) at JIVE, with a 2 s integration time. Each 32 MHz subband was channelized into 64 channels, 500 kHz each. The Astronomical Image Processing System (AIPS Greisen, 2003) and CASA (McMullin et al., 2007) software packages were used for the data reduction. We used the FITLD task in AIPS to load the correlated visibilities in the standard FITS-IDI format. Gain curves and system temperature measurements collected at each station during the observation were applied to the visibilities for a first-order amplitude calibration, followed by RFI flagging.

Visibilities were exported to UVFITS and then converted to measurement set (MS) format using the CASA IMPORTUVFITS task and flagged using FLAGDATA task after a manual inspection. Initially, the calibration source J1829+4844 was used to solve for the peculiar phase ψ_0 and

¹https://www.ira.inaf.it/precise/Home.html

²The Da station was virtually split into two stations (Da and Du) by the correlator to account for the simultaneous recording of different sets of spectral windows (see Table 5.1). As these are physically the same antenna, we considered the total number of antennas as 12.

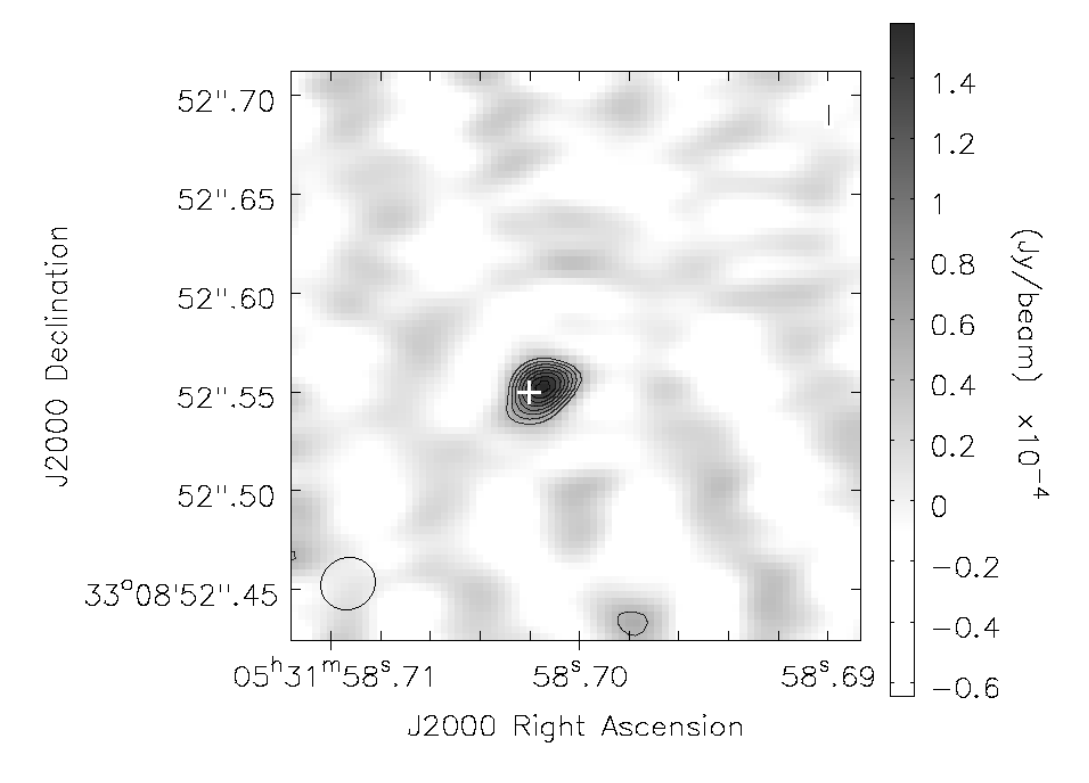


Figure 5.4: Image of the PRS associated with R1. Contours are drawn from 3 to 10 times the rms noise level $\sigma \simeq 15~\mu \mathrm{Jy~beam^{-1}}$. The white cross represents the reference position of the same PRS as obtained in Marcote et al. (2017), with the cross size approximately representing its 1σ uncertainties. The synthesized beam is $0.028'' \times 0.026''$, and is shown at the bottom left corner of the image as a black ellipse.

the delay term τ_i for each spectral windows. After this step, we also solved for the standard complex bandpass term using the CASA BANDPASS task, to calibrate phase variations of the bandpass not represented by a single delay term.

Peculiar phases, delays and bandpass were then applied to the secondary calibrator J0529+3209, which we used to solve for a delay term and a delay rate using all the spectral windows and for each time slot when the secondary was observed. Calibration was followed by flagging and the procedure was iterated over until calibration solutions converged. All calibration solutions were then applied to the target R1.

Visibilities corresponding to the R1 observations were Fourier transformed into a dirty image of $4.6'' \times 4.6''$, using the natural weighting scheme as routinely done in previous PRECISE observations (Marcote et al., 2020; Kirsten et al., 2022a; Nimmo et al., 2022a; Bhandari et al., 2023; Hewitt et al., 2024). We used the multifrequency synthesis algorithm to combine together all the spectral windows. The dirty image clearly shows a point source at the image centre and no other source across the field of view. We performed a deconvolution down to a 15 μ Jy beam⁻¹ rms noise and obtained a clear detection of the PRS associated with R1 (Figure 5.4). We fitted a two dimensional Gaussian to the source and found its position to be $\alpha_{\rm J2000} = 05^{\rm h} 31^{\rm m} 58.702^{\rm s} \pm 0.002$ s, $\delta_{\rm J2000} = +33^{\circ} 8' 52.551'' \pm 2$ mas, and found its flux density to be $180 \pm 15 \ \mu$ Jy. Both the position and flux density values are consistent with Marcote et al. (2017), i.e. $\alpha_{\rm J2000} = 5^{\rm h} 31^{\rm m} 58.70159^{\rm s} \pm 0.00006$ s, $\delta_{\rm J2000} = 33^{\circ} 8' 52.5501'' \pm 0.7$ mas

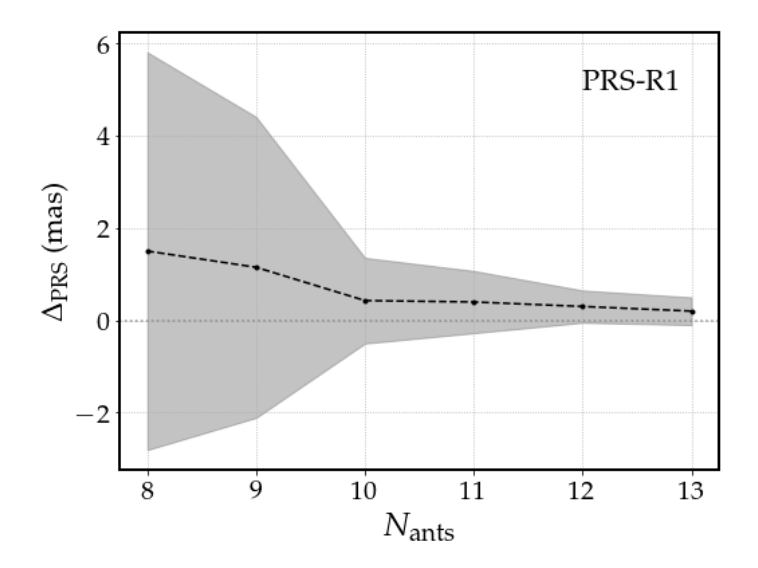


Figure 5.5: Offset between the recovered PRS coordinates and the nominal ones as a function of the number of antennas included in the observation. The shaded grey region represents the 1σ distribution of the offset, computed over the different realizations for each value of $N_{\rm ants}$. We note that the offset increases with decreasing number of antennas.

5.4 Impact of calibration errors on VLBI localisations

We used our observations of R1 as a testbed to quantify the localisation accuracy. We first considered the PRS case. Calibration errors will affect the PRS astrometry: in particular we explored the impact that a smaller number of antennas will have on calibration and imaging. The number N of antennas in an array determines the number N(N-1)/2 of visibilities, that scales as $\sim N^2$. As calibration attempts to solve for N antenna-based gains using an overdetermined system of N(N-1)/2, the larger the number of antennas and the larger the number of measurements per unknown and therefore, the more accurate the fit ought to be. Conversely, the smaller the number of antennas and the less accurate the solutions are expected to be, with the somewhat limiting case of N=3 antennas that leads to three visibilities.

A small number of antennas is expected to impact astrometry due to imaging limitations. It leads to a poorer uv coverage and, therefore, to a point spread function that has higher sidelobes and, generally, a less defined main lobe. Although earth-rotation synthesis may compensate this effect as, after all, PRS observations do not need to reveal complex source morphology, a limited uv may remain an issue in FRB observations that are, essentially, instantaneous.

In order to simulate the impact of calibration errors, we developed JOANNE, a custom pipeline that allows to corrupt visibilities and inject FRB-like sources in interferometric observations. The pipeline is described in details in the Appendix of this Chapter. We used JOANNE to repeat the calibration and imaging procedures described in Section 5.3 for $N_{\rm FRB}=5$ cases, where we removed one antenna from the array for each case. In each run of the pipeline, a subset of $N_{\rm rem}$ antennas was randomly selected and removed before restarting the entire calibration process. Furthermore, for a given number $N_{\rm rem}$ of removed antennas, we repeated the procedure multiple times, each time selecting a different set of antennas.

For each simulated case we fitted a two dimensional Gaussian to the PRS and computed the difference (offset) Δ_{PRS} between the best fit coordinates and the position determined by Marcote et al. (2017), $\alpha_{M17} = 5^{\rm h} 31^{\rm m} 58^{\rm s}.70159$ and $\delta_{M17} = 33^{\circ} 8' 52''.5501$:

$$\Delta_{\text{PRS}} = \sqrt{(\alpha_{\text{PRS}} - \alpha_{\text{M17}})^2 + (\delta_{\text{PRS}} - \delta_{\text{M17}})^2}.$$
 (5.13)

The magnitude of the offsets increases as more antennas are discarded from the array (Figure

5.5), following the qualitative expectations. It ranges from less than 1 mas for the case when all the 13 antennas are used, up to almost 6 mas when only 8 antennas are used. However, even in the most pessimistic case (i.e. for $N_{\rm ants}=8$), the best fit coordinates are consistent with the nominal values within the uncertainties, indicating that fewer antennas have a negligible impact on the calibration and imaging of the PRS.

5.4.1 The FRB case

We then explore how calibration errors may impact the observation of an actual FRB. As we do not have actual burst detections in our observations, we need to simulate how an FRB source would be seen in our observations. In the PRECISE project, FRB interferometric observations are carried out using "gated" visibilities: bursts are usually searched in single-dish observations using the most sensitive antenna and visibilities are correlated only for the duration of the detected event ("gated"). This procedure prevents from correlating a large number of visibilities that would ultimately contain no signal and allows for a much better time resolution than what is normally achieved in standard interferometric observations (see, e.g., Nimmo et al., 2022a). As the FRB DM is already known, the gated visibilities are also directly de-dispersed at the nominal DM value. This scenario simplifies greatly our FRB simulations:

- we can neglect the actual duration of a simulated burst and assume that it lasts as long as the integration time used in the PRS observation, i.e. 2 s. A 2 s-long observation generates an instantaneous *uv* coverage that is essentially identical to what one would obtain from a few ms observation of an actual "gated" burst;
- we do not need to simulate a dispersed FRB but we can essentially treat it as a standard continuum source.

In practice, the aforementioned assumptions allowed us to split a 2 s-long observation from the PRS data set and inject the visibilities corresponding to a continuum point source in it, assuming it is, effectively, an FRB (see the Appendix to this Chapter for further details). The burst was always injected at the nominal pointing direction. Actual observations of repeating FRBs, may detect tens of events with different fluences and with random times of arrival (e.g. Hewitt et al., 2024). We simulated a number of cases that span S/N = 15 and 20, respectively, and a number of bursts ranging from 5 to 50, with times of arrival randomly distributed across the duration of the PRS observations. From an operational standpoint, we randomly selected N, 2 s-long visibilities from our calibrated observations and added the visibilities corresponding to a point-like source with S/N = 15. The range of burst numbers is consistent with literature observations (e.g. Nimmo et al., 2022a; Hewitt et al., 2024). Following Marcote et al. (2017); Kirsten et al. (2022a); Nimmo et al. (2022a); Hewitt et al. (2024) the N snapshot observations were imaged jointly in order to improve the uv coverage and, therefore, the burst detectability.

In order to assess the impact of calibration errors on the burst astrometry, we follow a different procedure than the previous section. If we call $\hat{\psi}_i$ the best-fit phase of antenna i obtained from calibration (see equation 5.10 and 5.11), we perturbed it by adding a ϵ_i term:

$$\hat{\psi}_{i,0} = \psi_{i,0} + \epsilon_i. \tag{5.14}$$

We drew ϵ_i from a uniform distribution in the range $[0, \epsilon_{\psi, \text{max}}]$, with $\epsilon_{\psi, \text{max}} = 10^{\circ}, 20^{\circ}, 30^{\circ}, 40^{\circ}$ and 50° respectively. In order to quantify the impact that phase errors have on the FRB localisation, we used the same metric defined in equation 5.13, now considering the FRB coordinates and relative shift Δ_{FRB} . We found that, in general, the magnitude of the offset from the nominal FRB position increases with $\epsilon_{\psi, \text{max}}$, as expected (Figure 5.6). We found that a larger number of simulated bursts helps reducing the localization error mostly when $\epsilon_{\psi, \text{max}}$] < 20°, whereas

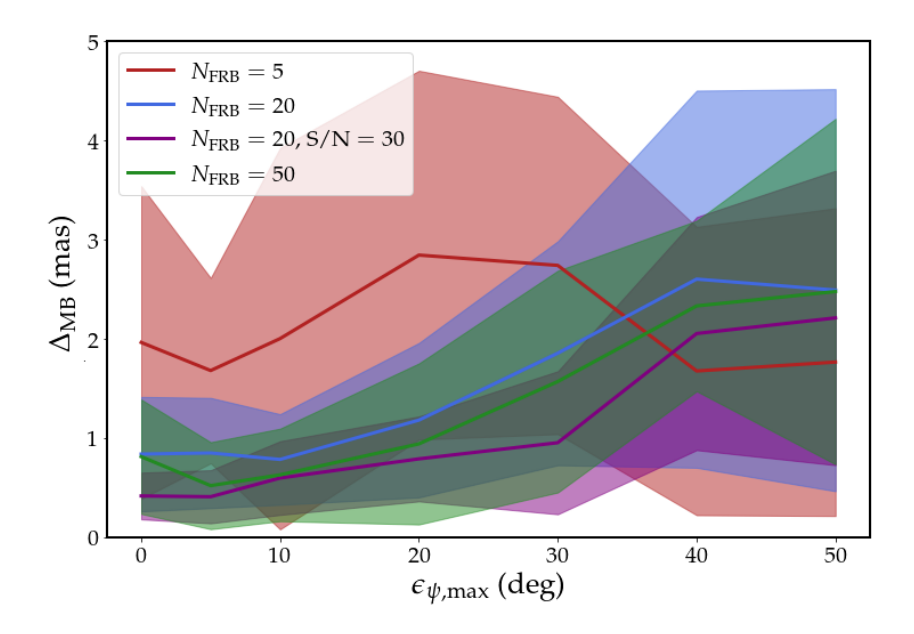


Figure 5.6: Positional offset of a simulated FRB as a function of maximum phase error (see text for details). Thick lines represent the mean offset values, whereas the coloured areas represent the 68% uncertainty confidence region. Where not specified, the individual bursts have S/N = 15.

it does not help much when the corruptions are large. The average magnitude of the offset remains smaller than 3 mas regardless of simulated the number of bursts and the magnitude of the phase corruption. Considering that phase errors in actual observations are expected to be smaller than 20°, our results indicate that localizations presented in literature observations are likely not significantly affected by calibration errors.

5.5 Conclusions

In this chapter, we have evaluated the impact of systematic errors on the localisation accuracy of FRBs in high angular resolution observations.

We used EVN observations of the R1 FRB taken as part as the PRECISE project. No burst was present in our observations, and we generated a continuum image integrated over the 3.6 h of the duration of the observation. We achieved a 15 μ Jy beam⁻¹ rms noise and detected the PRS associated to the burst with a 180 \pm 15 μ Jy flux density - consistent with literature measurements.

We tested the accuracy of the PRS localization by excluding antennas from the array and repeating the calibration. We confirm that the localization errors increase with the number of antennas excluded but they remain, in average, smaller than 2 mas even in the case where only eight antennas where used. This was already found in Nimmo et al. (2022a).

We then simulated and injected an FRB in the visibility data in order to assess its detectability and astrometry in presence of calibration errors that we simulated by perturbing the antenna phases. We used a simple recipe for introducing phase errors, drawing them from a uniform distribution between 0 and a changing maximum value up to 50° . We found that calibration-induced errors on the FRB position remain, in average, below 3 mas, consistent with the localisation uncertainties reported for several FRBs (e.g. Marcote et al., 2017; Kirsten et al., 2022a; Nimmo et al., 2022a; Hewitt et al., 2024). This implies that calibration errors are unlikely to compromise the association of FRBs with specific environments, such as globular clusters, in the case of FRB 20200120E. The magnitude of the errors would allow to associate a FRB to a globular cluster up to $z \sim 0.35$.

Appendix A. joanne: a pipeline for transient simulation into VLBI visibilities

In this work, I developed a custom pipeline called JOANNE (inJection Of fAst traNsients iNto visibilitiEs) designed to simulate the injection of FRB-like signals into radio interferometric visibility data. The primary purpose of this pipeline is to facilitate the study of systematic errors in VLBI calibration, as discussed in detail in the current Chapter, and their effects on transients localisation. The pipeline is implemented in Python 3 and can be easily run within the CASA environment, leveraging CASATOOLS and CASAVLBITOOLS to handle calibration tables and MS files.

The simulated transients are modeled as ideal point sources with a duration equivalent to the length of an integration time ($T_{\rm int}=2~{\rm s}$), slightly simplifying real interferometric observations where the FRB detection occurs. Typically, a high-sensitivity telescope within the array (e.g., Effelsberg) is used to detect the burst, after which the raw data are re-correlated at the burst's time of arrival with a short gating window to maximize the burst S/N and to achieve an higher time resolution (e.g. Nimmo et al., 2022a). Instead, JOANNE simulates the injection of transients over one integration time.

The main pipeline script begins by reading all the useful information from a configuration file, managed by the yaml package. The latter contains path settings, specifications for the transient signals to be injected (e.g. flux densities, characteristic frequencies), paths to files and parameters for the imaging of output burst visibilities. A configuration file looks like this:

```
general:
      listobs_path: /path/to/listobs/.listobs
      file_ToAs: /path/to/timeofarrivals.dat
      EXPERIMENT: test
      output_path: /path/to/output_path/
  calibration:
      uvfile: /path/to/uvfits_file/.uvfits
8
      ms: /path/to/msfile/.ms
9
      base_calib: /path/to/calib_folder/
10
      targetFLAG: /path/to/flags/FLAGtarget.flagcmd
11
      bp_cal: J1829+4844
      ph_cal: J0529+3209
13
      target: R1_D
14
      sbdtab: ek051e.sbd
15
      mbdtab: ek051e.mbd
16
      bpasstab: ek051e.bpass
17
      Kselftab: J0529+3209_self.K
18
      pselftab: J0529+3209_self.p
19
      apselftab: J0529+3209_self.ap
20
      antID: EF,TR,WB,NT,O8,CM,DA,DU,KN,PI,DE,JM,MC
21
22
23
  imaging:
      modeIM_single: DIRTY
24
      modeIM_concat: CLEAN
25
      imsize: 1280
26
      box_region: 626,626,654,654
27
      rms: 2.e-4
28
      keep_single_ms: False
29
30
 injection:
31
      nFRBs: 15
32
      fl_ch: 0.01
33
   fl_std: 0.025
```

```
alpha_fl: -2
      modeFL: equal
36
      freq: 1.4GHz
37
      BW: 0.256GHz
38
      direction: J2000 05h31m58.700s +33d08m52.568s
39
      cell: 3.6 mas
40
      t_start_inj: 2022/09/22/00:00:00
41
      t_stop_inj: 2022/09/22/05:48:39
42
      fld_inj: R1_D
43
      mode_inj: uniform
44
45
  corruption:
46
    do_corrupt: True
47
    ant_not_used: None
48
    corr_ant: All
49
    corruption: 1.0
50
    corrupt_table: ek051e_All.mbd
51
52
    corr_mode: manual
    corr_min: -20
53
    corr_max: 20
54
    corr_parameter: phase
```

Listing 5.1: Example of configuration file used in the joanne script

The script reads all the information and sets all the internal variables. Consequently, the following steps are executed³:

- 1. Import of the UVFITS file in a CASA MS (IMPORTUVFITS) and application of a mask, if provided, for RFI flagging (FLAGDATA task).
- 2. MS split in multiple 2 seconds-long chunks (SPLIT task) at the FRB ToAs. The ToAs can be determined by setting the mode_inj parameter in the configuration file. The user can read the ToAs from an external file, or can choose to distribute them following a uniform distribution given two limiting timetables. While the selection of only the target's scans for the FRB injections is done automatically choosing a uniform distribution, this has to be accurately done by the user following the format of timetable variables present in the configuration file. Nonetheless, the "from file" mode can be exploited to generate FRBs at the same time between different runs.
- 3. Calibration of the split MSs^4 (APPLYCAL task) and possibly cleaning of calibrated target visibilities (RFLAG mode of FLAGDATA task). The calibration tables needed by the APPLYCAL task have to be provided by the user.
- 4. Injection of a fake point source into each split MS. The injected source is modelled as an ideal Dirac's delta in the image plane. The user, via the configuration file, can set all the injection parameters such as, e.g., the source flux density, its coordinates in the final image and so on. Moreover, the user can opt to inject a N_{inj} number of fake point sources, and can choose the flux density distribution. The latter can be chosen such that the fake FRBs will have same flux density (equals to the fl_ch parameters in the configuration file), distributed randomly around fl_ch with a fl_std standard deviation or distributed following a power-law, with minimum flux density set by fl_ch and a given

 $^{^{3}}$ The script permits easy access to single steps rather than executing the entire pipeline each time. This can be achieved simply by setting the internal mysteps variable, directly from the CASA command line. E.g. mysteps = 2, 4 will execute only the second and the fourth steps.

⁴We prefer to apply calibration tables to split MSs instead of applying them to the whole MS to reduce the computational time of the pipeline.

power-law index alpha_fl. Each modelled point source in the image plane is then Fourier transformed and inserted into the MODEL visibilities column of each splitted MS, and finally added to the CORRECTED visibility column using the UVSUB task.

- 5. Split MS files concatenation (CONCAT task).
- 6. Imaging of the concatenated MS file (TCLEAN task) and fitting of the injected point source in the image plane (IMFIT task). Here the imaging parameters can be set in the "imaging" part of the configuration file. In particular, the user can choose to image single bursts and / or the concatenated visibilities, can set the final image size along with the edges coordinates of the box region in which the point sources are injected. This is useful for the determination of the source flux density and for the Gaussian fitting to the point source.

Perturbation of calibration solutions. The pipeline allows for the introduction of perturbations in the fringe-fitting calibration solutions⁵, to investigate the impact of systematic errors on FRB localisation accuracy, injecting an error in calibration parameters to simulate an imperfect calibration process (see Section 5.4.1 for details).

The perturbation is managed by the function corruptVIS within the pipeline, which operates by modifying the antenna-based calibration tables. The user can choose which antennas are affected and control the amplitude of phase offsets to be applied. The perturbation can be applied in several modes, such as manually specified offsets, or randomly drawn values within a predefined range. Through the corr_parameter argument, it is possible to select which calibration parameter has to be perturbed (i.e. phase, delay group or delay rate). The corruptVIS function supports two modes for applying the perturbations, i.e. the "manual" mode, in which the user manually specifies the perturbation factor, corrFACT, applied uniformly across the selected antennas, and the "external" mode, where the perturbation is applied using an array of external values, allowing for greater control over individual antenna perturbations. In particular, for the latter mode, the perturbation of a given antenna is drawn from a uniform distribution having range [corr_min, corr_max], and it is time-invariant, i.e. constant over the observation scan numbers.

The resulting perturbed calibration solutions are then stored in a new calibration table, which is subsequently applied to the data using CASA APPLYCAL task. Note that, at this stage, the data at which the perturbed calibration table is applied are pre-calibrated, so that the new APPLYCAL acts as a perturbation.

After the download of the JOANNE pipeline from the GitHub page⁶, and after the setting of the configuration file, one can run JOANNE by following few simple steps:

```
cd /path/to/joanne/
casa  # Start the CASA environment
mysteps=[0,1,2,3,4,5]
execfile("go_joanne.py")
```

⁵While this implementation currently focuses on perturbing calibration tables derived from fringe-fitting solutions, future developments will explore the perturbation of other calibration types, such as bandpass and amplitude solutions, to further expand the scope of systematic error simulations.

⁶https://github.com/davidepelliciari/joanne

Chapter 6

Conclusions

Since the discovery of the first FRB in 2007, observational efforts have grown significantly, with an increasing number of telescopes worldwide contributing to their study. The discovery of repeating FRBs has been particularly significant, allowing for a more detailed characterization of their emission properties. Long-term, multiwavelength observations are crucial to unveil the properties of repeating FRBs and expand the known sample.

Notably, the only currently observed difference between one-off FRBs and repeaters concerns their spectro-temporal properties: on average, repeaters exhibit bursts with narrower bandwidths and longer durations (Pleunis et al., 2021b). However, we still lack a complete characterisation of the FRB spectra, mainly because FRB emission - especially in repeaters - tends to be confined within a narrow frequency range.

In addition to the long-term monitoring of repeaters, interferometric observations enabled the association of FRBs with their host galaxies. This has not only confirmed their extragalactic origin—with the most distant FRB localised to a galaxy at redshift $z \sim 1$ (Ryder et al., 2023) – but also allowed the properties of their host galaxies and, in a few cases, the local environment within them. While most of the localised FRBs are found in spiral galaxies, there is no clear correlation with SFRs, and some have even been localised in early-type galaxies (e.g. Connor et al., 2023). The hyperactive repeating FRB 20200120E represents a striking as it was associated to a GC within the nearby galaxy M81 (Kirsten et al., 2022a). This discovery has challenged the traditional formation models, as a core-collapse-formed magnetar like SGR J1935+2154 is unlikely to be associated with an old stellar system such as a GC. However, under the magnetar hypothesis, alternative and exotic processes, such as AIC or MIC, could lead to the formation of FRB-emttings magnetars in GCs. Among interferometric observations, VLBI has provided the most precise associations, including PRSs (e.g. Marcote et al., 2017). Little is known about the physical properties of PRSs, as only three have been identified at the time of writing this thesis, but ensuring ever more precise localisations will be fundamental in order to extract as much information as possible regarding the origin of FRBs and their link to PRSs.

This thesis explored the FRB phenomenon via low-frequency radio observations, multiwavelength campaigns, and precision localisation techniques. I presented an extensive NC monitoring campaign to investigate the connection between FRBs and magnetars. The study, discussed in Chapter 3, targeted seven nearby star-forming galaxies, aiming to detect FRBs with energies $E \geq 10^{34}$ erg, i.e. the radio burst observed from the Galactic CCSN magnetar SGR J1935+2154. The advantage of observing star-forming galaxies lies in the fact that a greater number of magnetars can be observed simultaneously within them. We collected ~ 700 hours at 408 MHz on our targets, obtaining no detections from these sources. This upper limit constrained the magnetar burst rate $\lambda_{\rm mag}$ to be $\lambda \leq 0.4$ magnetar⁻¹ yr⁻¹. By combining our results with the ones presented in previous observations (CHIME/FRB Collaboration et al., 2020), we obtained $\lambda \leq 0.25$ magnetar⁻¹ yr⁻¹. This suggests that, while CCSN magnetars are a likely progenitor for some FRBs, they may not be the most common progenitor, supporting the idea that other sources, such as much younger and powerful magnetars may be required to explain the higher repetition rates observed in active FRB sources (Margalit et al., 2020b). Aside, we also provided the first FRB constraints from a sample of ULXs, since some of the galaxies of our sample host confirmed ULXs. As done for the magnetar FRB channel, we computed upper limits for the FRB rate coming from ULXs, obtaining $\lambda_{\rm u} \leq 13~{\rm yr}^{-1}$ per ULX.

In Chapter 4 I presented the results of a detailed study of the hyperactive repeater FRB 20220912A using a combination of radio and high-energy observations. Regarding the radio monitoring, we conducted 408 MHz observations with the NC and simultaneous 1.4 GHz observations with the Mc radio telescope. In total, 16 bursts have been detected from the source with a 95% completeness fluence of ~ 17 Jy ms at 408 MHz. No burst was detected at 1.4 GHz over 177 hours, placing an upper limit on the burst rate of 0.017 hr⁻¹ at 95% confidence, approximately four orders of magnitude lower than the activity reported during a burst storm event at similar spectral energies and radio frequency range (Zhang et al., 2023a; Feng et al., 2023; Hewitt et al., 2023; Sheikh et al., 2023). These led to a first characterisation of the broadband spectrum (between 0.4 and 1.4 GHz) of the source, placing an upper limit of $\beta \leq 2.6$ on its spectral index.

We mesured the cumulative burst rate as a function of the spectral energy, finding that the latter can be well-fitted by a single power-law function $R(>E_{\nu}) \propto E_{\nu}^{\alpha_E}$, with $\alpha_E = -1.3 \pm 0.2$ at 408 MHz. Moreover, we compared the cumulative burst rate distribution of FRB 20220912A with another hyperactive source, FRB 20201124A, finding similarities in both their spectral energy and rate ranges. These similarities suggest that the two sources, and possibly hyperactive repeaters in general, could share the same emission mechanism shaping their energy distributions.

Notably, we observed that the slope of the cumulative spectral energy rate distribution of FRB 20220912A flattens for bursts at $E_{\nu} \geq 10^{31}$ erg Hz⁻¹, where the spectral index changes from $\alpha_E = -2.15 \pm 0.01$ to $\alpha_E = -1.0 \pm 0.3$. This flattening has been reported for other two hyperactive repeaters, R1 (Hewitt et al., 2022; Jahns et al., 2023) and FRB 20201124A (Kirsten et al., 2024), and can potentially represents a link between one-off sources and repeaters, given that the cumulative energy distribution of one-off bursts has a characteristic slope of $\alpha \simeq -1$ (James et al., 2022b). Additionally, we performed three-hour continuum radio observations of the FRB 20220912A field at 1050-1450 MHz with the uGMRT, detecting a continuum point-like source with a flux density of 240 ± 40 μ Jy, spatially coincident with the FRB localisation obtained via VLBI observations (Hewitt et al., 2024). Given that, in the latter, a PRS was not found for a flux limit of 48 μ Jy, we ascribed the origin of our detected source to star-formation processes. Finally, we reported no detections from the high-energy monitoring. At γ -ray energies, we established an UL on the radio efficiency $\eta = E_{\gamma}/E_{\rm radio} < 1.5 \times 10^9$ for the fifth detected burst by the NC.

Chapter 5 is focused on the high-precision localisation of FRBs using VLBI observations. The goal was to assess the impact of systematic calibration errors on the ability to accurately pinpoint FRB sources via observations conducted with the EVN. The level of accuracy reached with such observations is crucial for associating FRBs with specific astrophysical environments, such as star-forming regions or PRSs, and for understanding the local conditions that may influence their emission. I calibrated EVN observations from the repeating FRB 20121102A, which is also co-located with a PRS. I managed to detect the PRS and measure its flux density to be 180 \pm 15 μ Jy, consistently with previous literature measurements.

We tested the accuracy of the PRS localization by excluding antennas from the array and repeating the calibration. We found that the localization errors increase with the number of antennas excluded but they remain, in average, smaller than 2 mas even in the case where only eight antennas where used. We also assessed the impact of calibration errors in FRB astrometryr by simulatinb and injecting an FRB in the visibility data. Calibration errors were simulated by

perturbing the antenna phases. We used a simple recipe for introducing phase errors, drawing them from a uniform distribution between 0 and a changing maximum value up to 50°. We found that calibration-induced errors on the FRB position remain, in average, below 3 mas, consistent with the localisation uncertainties reported for several FRBs (e.g. Marcote et al., 2017; Kirsten et al., 2022a; Nimmo et al., 2022a; Hewitt et al., 2024). This implies that calibration errors are unlikely to compromise the association of FRBs with specific environments, such as globular clusters, in the case of FRB 20200120E.

6.1 Future prospects

In the context of the projects developed during this thesis, several possible advancements can be foreseen. Regarding the study of the FRB–magnetar connection, we are already conducting a monitoring project with the NC radio telescope on a sample of eight Galactic magnetars. These observations are performed using a receiving system of 16 cylinders, offering twice the sensitivity compared to the setup used in Chapter 3. Expanding the monitoring outlined in Chapter 3 could be beneficial by either increasing the sample of galaxies under observation or focusing on a different demographic study, such as observing more massive star-forming galaxies (see, e.g., Sharma et al., 2024) or conducting observations of galaxy clusters, from which an increase in FRB burst rate is expected (Agarwal et al., 2019), or galaxy hosting a large number of globular clusters.

Also projects focused on the multi-wavelength monitoring of highly active repeating FRBs will also benefit from the capabilities of the NC. Its ability to provide continuous low-frequency monitoring makes it ideal for following up on new repeaters announced by, e.g. CHIME or FAST. For instance, other than FRB 20220912A, our low-frequency follow-up of the hyper-active repeater FRB 20240114A (see the Appendix of Chapter 4) has revealed crucial details about the time evolution of its high-frequency emission. This type of chromatic behaviour could be a common feature among repeaters, warranting further study through extended multi-frequency monitoring. Regarding the latter, we have recently detected FRB with the Noto radio telescope, similarly to what has been done for the Mc radio telescope. With the Noto radio telescope, it will be possible, then, to conduct simultaneous observations at four separate frequency bands, exploiting the sinergy between all the Italian radio facilities, i.e. NC, Mc, Noto and Sardinia radio telescopes.

Finally, we recently started an observational campaign with the uGMRT at 1.4 GHz to search for PRSs associated to 19 well localised FRBs, approximately half of which are repeaters and half one-off events. These observations will represent a systematic attempt to characterize the radio properties of a sample of PRSs.

Chapter 7

Acknowledgements

This is one of those moments I have imagined so intensely and for so long, so many times: the moment when I would sit in front of my computer and begin writing the acknowledgments for my PhD thesis. And here I am, exactly at that moment, now. This means that I made it, I reached the end—what a feeling. These have been three tumultuous, intense years, marked by changes, uncertainties, and difficulties, but also by many beautiful moments, wonderful experiences that I will not easily forget—in fact, I hope never to forget them. Most of all, I enjoyed the wonderful people I met during these three years, both known thanks to the Ph. D. and external to it.

I sincerely thank Gianni and Maura, true mentors throughout these three years, as well as my supervisors. I will always carry in my memory and in my heart the long conversations and discussions, both scientific and otherwise, shared with Gianni in the office, through which, step by step, I grew as a scientist and as a person. We also had misunderstandings, of course, but that is part of the game and of a relationship that, in my opinion, aims to remain healthy. Thank you. The same goes for Maura, always available to help and guide me. I wish I had spent more time with Maura, but those days in Pescara for the Marcel Grossmann Meeting and in Alghero for the Congresso Nazionale Oggetti Compatti were invaluable. There, I realized Maura's energy—overwhelming. Thank you.

I thank Franz, who guided me through the most delicate three months of my entire PhD, those spent between Onsala and Gothenburg (which, by the way, is pronounced 'Yoteborie'—what a discovery). Those were months of complete transition, of self-awareness, and, in some ways, of letting go. In him, I saw experience, a desire to discover and learn. Despite his established expertise in the FRB field, I never once felt inferior, and every time he explained a new concept to me, or re-explained it, he always did so as an equal. I wish you a good life. Thank you.

I thank Stefano, with whom I shared everything, every little detail of this experience. I have appreciated every aspect of our relationship: the hours spent talking about science, discussing complex and wonderful concepts, the hours spent talking about how we never feel like doing anything, how so many Mondays actually felt like Fridays, the endless laughter, the countless muffled voice notes—Hoeft! With Stefano, I shared what is, without a doubt, the best experience of my PhD (and I believe his too!): the PhD School on transients in Cargèse in 2023. Only two madmen like us could think of taking a car, leaving from Bologna, and reaching the other side of Corsica by crossing mountains and endless forests—but what an adventure and what laughter! Thank you, my friend.

I thank Cristina, with her gentle ways, for being so close to me, especially in the delicate final year of my PhD. I loved our long coffee breaks—without coffee—spent talking about everything that concerns us. I adored the complexity but also the lightness we managed to create. Thank you for not stopping at the surface, for digging deeper into my world. Moreover, without you, I wouldn't have known how to handle nearly any of the conferences I attended. With you,

everything becomes more semplice, so to speak. Thank you.

I thank Luca Bruno, my worthy office mate before and after this PhD. With you, I shared my weaknesses, important conversations, and above all, we supported each other countless times. Thank you.

I thank Emanuele, whose energy struck me immediately, and in whom I found an endless number of similarities, starting with our obsession with Trio, and more broadly, with Italian comedy and impressions, leading ultimately to music. I thank you for introducing me to new music—what music!—that truly made me feel reborn. Without Pezzi della Sera, I wouldn't have written so many things I now hold dear. I also loved the way we shared this music; it was truly fantastic. Additionally, I thank you for supporting me, listening to me, and standing by me without ever asking for anything in return. I only regret that we couldn't share a trip, like a school, but maybe that was for the best? Thank you.

I thank Leonardo, in whom I immediately found a sincere friend. From our trip to Spain, between Granada and the *Sierra Nevada*, I discovered a fun, pleasant person with whom I could travel anywhere without ever getting tired of it. With you, I shared endless laughter—perhaps the loudest ones, when I think about it. It's a shame we only shared one year of the PhD, but surely it was an incredibly intense one. I thank you for listening to me in difficult moments, while I tried to untangle my thoughts. Thank you.

I thank Cristiana, who taught me the basics of interferometric calibration, but not only that. She showed me what positivity at work means, what initiative is, and I tried in every way to absorb her energy. You were the first person (besides my supervisors) I spoke to during my PhD, and I immediately recognized the wonderful person you are. Thank you.

I thank the wonderful people who populate the IRA every day: Davide, Luca, Jort, Emilio, Alessio, Matteo, Lorenzo, Rachele, Francesca, Koushika. Even though I didn't have the time to build close relationships with most of you, I love the group that is forming and the kind of people you are. Despite the short time, I have already collected some beautiful memories and great laughter. Thank you. No, I haven't forgotten my President. I thank Ettore—you are a wonderful person, and you have incredible strength and energy. Thank you.

I thank ChatGPT and those who created it. Thank you.

I thank *Camilla* for being by my side for most of my PhD, for holding my hand and listening to me in my darkest moments. Sometimes I miss you, and I truly hope you find happiness in life. Thank you.

I thank my cavalieri, Simone, Nicolas, Riccardo, and Paolo, with whom I have shared important experiences—many even during these past three years. I would have liked to thank each of you individually, but I realize I would use the exact same words for all of you. I wish you an incredible career—you are all strong, capable, interesting, and extraordinary. You will always find a friend in me, ready to listen, laugh, and share everything. I'm sorry if I wasn't at my best—you mean the world to me, and I can't wait to share another thousand adventures with you, hoping we truly find each other again. Thank you.

I thank Renato, as we are slowly sharing many special moments, mostly filled with music. Thank you.

I thank Orlando, with whom I shared, even from a distance, the most delicate moments of the most delicate period of this PhD–again, Sweden. With a small guitar bought cheaply in a store in Kungsbacka, I had written something, and by sharing it with you, I found the strength, the desire, and the courage to move forward. And the beautiful thing is that you started doing the same with me, and I felt lucky. I have very few people around me with whom I truly share music, and you are definitely the one who understands me the most in this sense. Never stop. Thank you.

I thank Luca Bi, and writing these acknowledgments is truly difficult. Thank you for believing in me once again, after eight years, after an ocean of silence and distance. With you, I

shared the purest essence of who I am and what I love to do. Those hours in the studio were invaluable, pure gold. Creating with you is something I struggle to describe. Watching you work is a constant source of inspiration and learning. I truly hope to keep creating and having fun with you because our synergy is undeniable, and from synergy, the best results come (see Pelliciari et al., 2023a, ahah). Thank you.

I thank Lisa for supporting and pushing me, pushing me, pushing me to overcome my fears, for the kind words about the songs, about *Galassie*. In you, I have found a precious new friend. Thank you.

I thank Francesco, with whom I have built a wonderful friendship, a sense of complicity, and, once again, synergy. Your humor and comedic timing are devastating. You are incredibly talented, and I have deeply enjoyed working with you, but also discovering how similar we are in many ways. I hope—and, deep down, I believe—that we will create beautiful things together. Thank you.

I thank the friends from the Arezzo trip: Enzo, Lucia, Luca, Lorenza, Alice, Davide, and Diletta. You welcomed me as one of you, and you cannot imagine how much that moved me. I am happy to have met you and to have shared such wonderful moments together. Let's do it again! Thank you.

I thank my family: my mother, Giulia, my father, Maurizio, and my sister, Chiara. You are important, essential, even if very often-perhaps too often-I fail to show it. Thank you for always allowing me to follow the path I wanted, for making it possible for me to reach this point-a damn PhD in astrophysics. To my mother, I wish for serenity and the chance to travel, travel, reaching the places she has always dreamed of seeing. To my father, I wish the same, above all serenity, and to be surrounded by people who make him feel loved, heard, and valued. To my sister, I wish that she finds her place, her dimension, wherever in the world that may be. I love you. Thank you.

Finally, at the risk of sounding a bit cliché, I thank myself. Davide, you never stopped believing in your passions, and look where you have arrived. Whatever you may want, you can achieve—if you truly set your mind to it. And that is what, to me, the quote from Luca at the beginning of this thesis means: "PERCHÈ MI FISSO A FARE COSE CHE NON SO, SENZA SAPERE NEANCHE DOVE COMINCIARE? DI CERTO RIUSCIRÒ.". You are made of a thousand souls, a thousand worlds, and each one is waiting to be explored. You are good.

7.1 Ringraziamenti

Questo è uno di quei momenti che ho immaginato così intensamente, e così a lungo molto spesso: il momento in cui mi sarei seduto davanti al pc e avrei cominciato a scrivere i ringraziamenti della mia tesi di dottorato. Ed eccomi qua, esattamente in quel momento, ora. Questo significa che ce l'ho fatta, sono arrivato alla fine, che spettacolo. Sono stati tre anni travagliati, intensi, caratterizzati da cambiamenti, insicurezze, difficoltà ma anche da tanti bellissimi momenti, esperienze meravigliose che non scorderò facilmente, anzi, che spero di non scordare mai. Più di tutto, questo Ph. D. mi ha regalato rapporti veri, genuini e meravigliosi con tante belle persone.

Ringrazio di cuore Gianni e Maura, veri mentori in questi tre anni, nonchè miei supervisors. Mi porterò per sempre nella memoria e nel cuore le lunghe chiacchierate e discussioni, sia scientifiche che non, condivise con Gianni in ufficio, grazie alle quali, passo passo, crescevo come scienziato e come persona. Abbiamo avuto anche incomprensioni, certo, ma questo fa parte del gioco e fa parte di un rapporto che, a mio parere, vuole mantenersi sano. Grazie. Lo stesso posso dire di Maura, sempre disponibile ad aiutarmi e seguirmi. Con Maura vorrei averci passato più tempo, ma quei giorni a Pescara per il Marcel Grossmann Meeting e ad Alghero per

il Congresso Nazionale Oggetti Compatti sono stati preziosi. Lì mi sono reso conto dell'energia di Maura, fenomenale. Grazie.

Ringrazio Franz, che mi ha seguito nei tre mesi più delicati di tutto il dottorato, quelli passati tra Onsala e Göteborg (tra l'altro, si legge ioteborie, che storia). Erano mesi di transizione totale, di presa di coscienza, e di abbandono, sotto certi aspetti. In lui ho visto esperienza, voglia di scoprire, conoscere. Per quanto poi lui sia affermato nel campo FRB, in nessun modo mi sono mai sentito inferiore e ogni volta che mi spiegava un concetto nuovo, o che me lo rispiegava, era sempre alla pari. Ti auguro una buona vita. Grazie.

Ringrazio Stefano con cui ho condiviso tutto quanto, ogni più piccolo particolare, di questa esperienza. Ho apprezzato tutto del nostro rapporto: le ore a parlare di scienza, a discutere di concetti complessi e meravigliosi, le ore a parlare di quanto non abbiamo mai voglia, di come moltissimi Lunedì sembravano in realtà Venerdì, le infinite risate, gli infiniti audio ovattati, Hoeft! Con Stefano ho condiviso quella che senza ombra di dubbio è l'esperienza più bella del mio dottorato (e credo anche del suo!), ovvero la Scuola di Ph. D. sui transienti a Cargèse del 2023. Solo due pazzi come noi potevano pensare di prendere la macchina, partire da Bologna e arrivare dall'altra parte della Corsica scavalcando montagne e oltrepassando infiniti boschi, ma che meraviglia e che risate! Grazie caro.

Ringrazio Cristina, dai modi così gentili, per essermi stata così vicina soprattutto nell'ultimo delicato anno di questo dottorato. Ho adorato le nostre IRAconv spese a parlare di tutto ciò che ci riguarda, ho adorato la complessità ma anche la leggerezza che riusciamo a creare. Ti ringrazio per non esserti fermata alla superficialità, per essere andata più a fondo nelle mie cose. Oltretutto, senza di te non avrei saputo affrontare quasi nessuna delle conferenze a cui ho partecipato. Con te diventa tutto più semplice, se vogliamo. Grazie.

Ringrazio Luca Bruno, degno compagno di ufficio prima e dopo questo dottorato. Con te ho condiviso mie debolezze, chiacchiere importanti, e soprattutto ci siamo dati manforte a vicenda innumerevoli volte. Grazie.

Ringrazio Emanuele, la cui energia mi ha colpito da subito e nel quale ho ritrovato uno sterminato numero di somiglianze, a partire dall'ossessione per il Trio, più in generale per la comicità italiana, le imitazioni, arrivando, infine, alla musica. Ti ringrazio per avermi fatto scoprire nuova musica, e che musica, che mi ha fatto rinascere nel vero senso della parola. Senza Pezzi della Sera non avrei scritto tante cose di cui sono ora affezionato. Ho poi amato il modo in cui abbiamo condiviso questa musica, è stato veramente fantastico. Inoltre, ti ringrazio per avermi supportato, ascoltato e sostenuto senza mai chiedere nulla in cambio. Mi dispiace solo non aver potuto condividere un viaggio, come ad esempio una scuola, ma forse è stato meglio così? Giro lungo, Grazie.

Ringrazio in primis Leonardo, in cui ho trovato un amico sincero sin da subito, i cui meme, tuttavia, non mi fanno ridere. Ahah. Apparte gli scherzi.. A partire dal nostro viaggio in Spagna, tra Granada e la Sierra Nevada, ho scoperto una persona divertente, piacevole, e con cui andrei in viaggio credo ovunque e non mi stancherei. Anche con te ho condiviso risate interminabili. Peccato aver condiviso solo un anno di dottorato, ma è stato veramente intenso. Ti ringrazio, poi, per avermi ascoltato nei momenti difficili, mentre cercavo di sbrogliare i pensieri. Grazie.

Ringrazio Cristiana che mi ha insegnato le basi della calibrazione interferometrica, ma non solo. Mi ha mostrato cosa significa la positività sul lavoro, l'intraprendenza e ho cercato in tutti i modi di coglierne l'energia. Sei stata la prima persona (oltre i miei supervisors) con cui ho parlato nel mio dottorato, e da subito ho capito la bella persona che sei. Grazie.

Ringrazio poi le belle persone che popolano l'IRA tutti i giorni, Davide, Luca, Jort, Emilio, Alessio, Matteo, Lorenzo, Rachele, Francesca, Koushika. Anche se con la maggiorparte di voi non c'è stato tempo di creare un rapporto stretto, adoro il gruppo che si sta creando e il tipo di persone che siete. Anche se c'è stato poco tempo, ho già collezionato qualche bel ricordo e qualche bella risata. Grazie. No, non mi sto dimenticando del mio Presidente. Ringrazio Ettore,

sei una bella persona e hai una forza ed energia strabilianti. Grazie.

Ringrazio ChatGPT e chi l'ha creato. Grazie.

Ringrazio *Camilla* per essermi stata vicino per la maggiorparte del mio dottorato, avermi tenuto la mano e avermi ascoltato nei momenti più bui in assoluto. A volte mi manchi e spero tu riuscirai a trovare felicità nella vita, davvero lo spero. Grazie.

Ringrazio i miei cavalieri, Simone, Nicolas, Riccardo e Paolo, con cui ancora ho condiviso esperienze importanti, molte anche durante questi tre anni. Avrei voluto ringraziarvi singolarmente ma mi rendo conto che userei le stesse identiche parole per tutti. Vi auguro una carriera incredibile, siete tutti forti, capaci, interessanti, formidabili. In me troverete sempre un amico, pronto ad ascoltarvi, ridere e condividere ogni cosa. Mi dispiace se non sono stato il massimo, vi voglio un infinito mondo di bene e non vedo l'ora di fare altre mille esperienze delle nostre, con la speranza di ritrovarci davvero. Grazie.

Ringrazio Renato, che piano piano stiamo condividendo tanti momenti speciali, fatti soprattutto di musica. Grazie.

Ringrazio Orlando con cui ho condiviso, anche se a distanza, i momenti più delicati del periodo più delicato di questo dottorato, sempre la Svezia. Con una chitarrina comprata a poco in un negozio di Kungsbacka, avevo scritto qualcosa e, condividendolo con te, ho trovato la forza, la voglia, e il coraggio di andare avanti. Grazie alla tua vicinanza (anche se a distanza di centinaia di km, sono nate *Flat White, Should I?* e *H.I.R.O.W.S.*. La cosa bellissima è che tu hai iniziato a fare lo stesso con me, e mi sono sentito fortunato. Ho pochissime persone intorno con cui condivido veramente la musica, e tu sei sicuramente la persona che più mi capisce in questo senso. Non fermarti mai. Grazie.

Ringrazio Luca Bi. Grazie per aver creduto ancora una volta, a distanza di 8 anni, dopo un oceano di silenzio e distanza, in quello che voglio fare, in quello che faccio. Con te ho condiviso l'essenza più pura di ciò che sono, di ciò che amo fare. Le ore in studio sono state di inestimabile valore, oro puro. Creare con te è una cosa che davvero faccio fatica a descrivere. Osservarti lavorare è ispirazione e insegnamento continuo. Spero davvero di continuare a creare e divertirmi con te, perchè la sinergia è innegabile e dalla sinergia si ottengono i risultati migliori (vedi Pelliciari et al., 2023a, ahah). Grazie.

Ringrazio Lisa per avermi supportato e spinto spinto spinto per farmi superare le mie paure, per le belle parole sulle canzoni, su *galassie*. Anche in te ho trovato una nuova amica preziosa. Grazie.

Ringrazio Francesco, con cui si è instaurato un bel rapporto di amicizia, complicità e, di nuovo, sinergia. Il tuo umorismo e i tuoi tempi comici sono devastanti. Sei pieno di talento e ho apprezzato enormemente lavorare con te, ma anche trovarci così simili per tanti aspetti. Spero e, in fondo, credo, creeremo cose belle. Grazie.

Ringrazio i ragazzi e le ragazze della vacanza ad Arezzo, cioè Enzo, Lucia, Luca, Lorenza, Alice, Davide e Diletta. Mi avete accolto come uno di voi in un periodo per me molto delicato, di cambiamenti forti. Sono contento di avervi conosciuto e di aver condiviso momenti belli con voi. Grazie. Rifacciamolo!

Ringrazio la mia famiglia, mia madre, Giulia, mio padre, Maurizio, e mia sorella Chiara. Siete importanti, fondamentali, anche se molto spesso, forse troppo, non riesco a dimostrarlo. Grazie per avermi sempre dato la possibilità di seguire la strada che volevo, avermi permesso di arrivare fino a questo punto, un cavolo di dottorato in astrofisica. A mia madre auguro di trovare serenità e di viaggiare viaggiare viaggiare, raggiungendo i posti che ha sempre sognato di vedere. A mio padre auguro lo stesso, la serenità in primis, e di circondarsi di persone che lo facciano sentire amato, ascoltato e desiderato. A mia sorella auguro di trovare la sua dimensione, il suo posto, che sia ovunque nel mondo va bene. Vi amo. Grazie.

Infine, a costo di sembrare un po' banale dall'esterno, ringrazio me stesso. Davide, non hai mai smesso di credere nelle tue passioni, anche quando di te rimanevano solo frammenti, e

guarda dove sei arrivato. Qualunque cosa tu possa volere puoi raggiungerla, se davvero vorrai farlo. Ed è questo che, per me, significa la citazione di *Luca* riportata a inizio Tesi: PERCHÈ MI FISSO A FARE COSE CHE NON SO, SENZA SAPERE NEANCHE DOVE COMINCIARE? DI CERTO RIUSCIRÒ. Sei composto da mille anime, mille mondi, e ognuno è da esplorare. Bravo.

Bibliography

Bhandari S., et al., 2023, ApJ, 958, L19

Bhardwaj M., et al., 2021a, ApJ, 910, L18

Bhardwaj M., et al., 2021b, ApJ, 919, L24

Abdalla E., et al., 2022, Journal of High Energy Astrophysics, 34, 49 Ablimit I., Li X.-D., 2015, ApJ, 800, 98 Agarwal D., et al., 2019, MNRAS, 490, 1 Agarwal D., Aggarwal K., Burke-Spolaor S., Lorimer D. R., Garver-Daniels N., 2020, MNRAS, 497, 1661 Akahori T., Ryu D., Gaensler B. M., 2016, ApJ, 824, 105 Alexander R., Fedorova V., 2020, The Astronomer's Telegram, 14186, 1 Amiri M., et al., 2017, ApJ, 844, 161 Anand G. S., Rizzi L., Tully R. B., 2018, AJ, 156, 105 Anna-Thomas R., et al., 2023, Science, 380, 599 Asaki Y., Saito M., Kawabe R., Morita K.-I., Sasao T., 1996, Radio Science, 31, 1615 Bailes M., et al., 2021, MNRAS, 503, 5367 Bannister K. W., et al., 2019, Science, 365, 565 Barsdell B. R., Bailes M., Barnes D. G., Fluke C. J., 2012, MNRAS, 422, 379 Bassa C. G., et al., 2017, ApJ, 843, L8 Beloborodov A. M., 2017, ApJ, 843, L26 Beloborodov A. M., 2020, ApJ, 896, 142 Beniamini P., Wadiasingh Z., Metzger B. D., 2020, MNRAS, 496, 3390 Beniamini P., Kumar P., Ma X., Quataert E., 2021, MNRAS, 502, 5134 Bethapudi S., Spitler L. G., Main R. A., Li D. Z., Wharton R. S., 2023, MNRAS, 524, 3303 Bezuidenhout M. C., et al., 2023, RAS Techniques and Instruments, 2, 114 Bhandari S., et al., 2022, AJ, 163, 69

Bhat N. D. R., Cordes J. M., Camilo F., Nice D. J., Lorimer D. R., 2004, ApJ, 605, 759

Blanchard P. K., Berger E., Fong W.-f., 2016, ApJ, 817, 144

Bochenek C. D., Ravi V., Belov K. V., Hallinan G., Kocz J., Kulkarni S. R., McKenna D. L., 2020, Nature, 587, 59

Bolli P., Perini F., Montebugnoli S., Pelosi G., Poppi S., 2008, IEEE Antennas and Propagation Magazine, 50, 58

Bonetti L., Ellis J., Mavromatos N. E., Sakharov A. S., Sarkisyan-Grinbaum E. K., Spallicci A. D. A. M., 2016, Physics Letters B, 757, 548

Bridle S. L., Eke V. R., Lahav O., Lasenby A. N., Hobson M. P., Cole S., Frenk C. S., Henry J. P., 1999, MNRAS, 310, 565

Bulgarelli A., Chen A. W., Tavani M., Gianotti F., Trifoglio M., Contessi T., 2012, A&A, 540, A79

Burgay M., et al., 2020, The Astronomer's Telegram, 13783, 1

Burrows D. N., et al., 2005, Space Sci. Rev., 120, 165

CHIME Collaboration et al., 2022, ApJS, 261, 29

CHIME/FRB Collaboration et al., 2019, ApJ, 885, L24

CHIME/FRB Collaboration et al., 2020, Nature, 587, 54

CHIME/FRB Collaboration et al., 2021, ApJS, 257, 59

Camilo F., Reynolds J., Johnston S., Halpern J. P., Ransom S. M., 2008, ApJ, 679, 681

Chatterjee S., et al., 2017, Nature, 541, 58

Chawla P., et al., 2020, ApJ, 896, L41

Chawla P., et al., 2022, ApJ, 927, 35

Chen G., Ravi V., Hallinan G. W., 2023, ApJ, 958, 185

Chevallier M., Polarski D., 2001, International Journal of Modern Physics D, 10, 213

Chime/Frb Collaboration et al., 2020, Nature, 582, 351

Chime/Frb Collaboration Andersen B. C., et al., 2022, Nature, 607, 256

Chime/Frb Collaboration et al., 2023, ApJ, 947, 83

Colla G., et al., 1970, A&AS, 1, 281

Colla G., et al., 1972, A&AS, 7, 1

Colla G., et al., 1973, A&AS, 11, 291

Connor L., et al., 2023, ApJ, 949, L26

Cordes J. M., Chatterjee S., 2019, ARA&A, 57, 417

Cordes J. M., Lazio T. J. W., 2002, arXiv e-prints, pp astro-ph/0207156

Cordes J. M., Lazio T. J. W., 2003, arXiv e-prints, pp astro-ph/0301598

Cordes J. M., McLaughlin M. A., 2003, ApJ, 596, 1142

Cordes J. M., Wasserman I., 2016, MNRAS, 457, 232

Cordes J. M., Wharton R. S., Spitler L. G., Chatterjee S., Wasserman I., 2016, arXiv e-prints, p. arXiv:1605.05890

Cordes J. M., Wasserman I., Hessels J. W. T., Lazio T. J. W., Chatterjee S., Wharton R. S., 2017, ApJ, 842, 35

Cruces M., et al., 2021, MNRAS, 500, 448

Cummings J. R., 2014, GRB Coordinates Network, 16530, 1

D'Amico N., et al., 1996, ApJS, 106, 611

Dai S., et al., 2019, ApJ, 874, L14

Dalcanton J. J., et al., 2009, ApJS, 183, 67

Dark Energy Survey Collaboration 2018, Phys. Rev. D, 98, 043526

Deng W., Zhang B., 2014, ApJ, 783, L35

Deng C.-M., Zhong S.-Q., Dai Z.-G., 2021, ApJ, 922, 98

Dolag K., Gaensler B. M., Beck A. M., Beck M. C., 2015, MNRAS, 451, 4277

Dong F. A., Chime/Frb Collaboration 2022, The Astronomer's Telegram, 15681, 1

Dong Y., et al., 2024, arXiv e-prints, p. arXiv:2405.00784

Draine B. T., 2011, Physics of the Interstellar and Intergalactic Medium

Duncan R. C., Thompson C., 1992, ApJ, 392, L9

Esposito P., et al., 2020, ApJ, 896, L30

Fabbiano G., 1989, ARA&A, 27, 87

Fabbiano G., Trinchieri G., 1987, ApJ, 315, 46

Fanti C., Fanti R., Ficarra A., Padrielli L., 1974, A&AS, 18, 147

Feng Y., et al., 2023, arXiv e-prints, p. arXiv:2304.14671

Ficarra A., Grueff G., Tomassetti G., 1985, A&AS, 59, 255

Flewelling H. A., et al., 2020, ApJS, 251, 7

Förster Schreiber N. M., Genzel R., Lutz D., Sternberg A., 2003, ApJ, 599, 193

Gajjar V., et al., 2018, ApJ, 863, 2

Gajjar V., et al., 2021, AJ, 162, 33

Gajjar V., et al., 2022, ApJ, 932, 81

Gao Y., Solomon P. M., 2004, ApJ, 606, 271

Gao H., Li Z., Zhang B., 2014, ApJ, 788, 189

Gardenier D. W., Connor L., van Leeuwen J., Oostrum L. C., Petroff E., 2021, A&A, 647, A30

Gawiser E., Silk J., 1998, Science, 280, 1405

Gehrels N., 1986, ApJ, 303, 336

Gehrels N., Chipman E., Kniffen D., 1994, ApJS, 92, 351

Gehrels N., et al., 2004, ApJ, 611, 1005

Ghisellini G., Locatelli N., 2018, A&A, 613, A61

Giacomazzo B., Perna R., 2013, ApJ, 771, L26

Ginzburg V. L., 1973, Nature, 246, 415

Gold T., 1968, Nature, 218, 731

Good D., CHIME/FRB Collaboration 2020, The Astronomer's Telegram, 14074, 1

Good D., Chime/Frb Collaboration 2020, The Astronomer's Telegram, 14074, 1

Gordon A. C., et al., 2023a, arXiv e-prints, p. arXiv:2311.10815

Gordon A. C., et al., 2023b, ApJ, 954, 80

Gourdji K., Michilli D., Spitler L. G., Hessels J. W. T., Seymour A., Cordes J. M., Chatterjee S., 2019, ApJ, 877, L19

Göğüş E., Woods P. M., Kouveliotou C., van Paradijs J., Briggs M. S., Duncan R. C., Thompson C., 2000, ApJ, 532, L121

Greisen E. W., 2003, in Heck A., ed., Astrophysics and Space Science Library Vol. 285, Information Handling in Astronomy - Historical Vistas. p. 109, doi:10.1007/0-306-48080-8 7

HI4PI Collaboration et al., 2016, A&A, 594, A116

Hagstotz S., Reischke R., Lilow R., 2022, MNRAS, 511, 662

Hamaker J. P., Bregman J. D., Sault R. J., 1996, A&AS, 117, 137

Hankins T. H., Eilek J. A., 2007, ApJ, 670, 693

Hassall T. E., et al., 2012, A&A, 543, A66

Heimersheim S., Sartorio N. S., Fialkov A., Lorimer D. R., 2022, ApJ, 933, 57

Heintz K. E., et al., 2020, ApJ, 903, 152

Hessels J. W. T., et al., 2019, ApJ, 876, L23

Hewish A., Bell S. J., Pilkington J. D. H., Scott P. F., Collins R. A., 1968, Nature, 217, 709

Hewitt D. M., et al., 2022, MNRAS, 515, 3577

Hewitt D. M., et al., 2023, arXiv e-prints, p. arXiv:2308.12118

Hewitt D. M., et al., 2024, MNRAS, 529, 1814

Houben L. J. M., Spitler L. G., ter Veen S., Rachen J. P., Falcke H., Kramer M., 2019, A&A, 623, A42

Hoyt T. J., et al., 2019, ApJ, 882, 150

Huang Y. X., et al., 2022, The Astronomer's Telegram, 15707, 1

Huguenin G. R., Moore E. L., 1974, ApJ, 187, L57

Inoue S., 2004, MNRAS, 348, 999

Ioka K., 2003, ApJ, 598, L79

Israel G. L., et al., 2016, MNRAS, 457, 3448

Israel G. L., et al., 2021, ApJ, 907, 7

Jahns J. N., et al., 2023, MNRAS, 519, 666

James C. W., 2023, PASA, 40, e057

James C. W., et al., 2020, ApJ, 895, L22

James C. W., Prochaska J. X., Macquart J. P., North-Hickey F. O., Bannister K. W., Dunning A., 2022a, MNRAS, 510, L18

James C. W., et al., 2022b, MNRAS, 516, 4862

Jessner A., et al., 2010, A&A, 524, A60

Johnston S., Romani R. W., 2004, in Camilo F., Gaensler B. M., eds, Vol. 218, Young Neutron Stars and Their Environments. p. 315

Jung T., Sohn B. W., Kobayashi H., Sasao T., Hirota T., Kameya O., Choi Y. K., Chung H. S., 2008, in The role of VLBI in the Golden Age for Radio Astronomy. p. 2, doi:10.22323/1.072.0002

Kaaret P., Feng H., Roberts T. P., 2017, ARA&A, 55, 303

Karachentsev I. D., Karachentseva V. E., Huchtmeier W. K., Makarov D. I., 2004, AJ, 127, 2031

Karuppusamy R., Stappers B. W., van Straten W., 2010, A&A, 515, A36

Kaspi V. M., Beloborodov A. M., 2017, ARA&A, 55, 261

Katz J. I., 2017, MNRAS, 471, L92

Katz J. I., 2020, MNRAS, 494, L64

Keane E. F., Kramer M., Lyne A. G., Stappers B. W., McLaughlin M. A., 2011, MNRAS, 415, 3065

Keimpema A., et al., 2015, Experimental Astronomy, 39, 259

Kellermann K. I., Pauliny-Toth I. I. K., 1969, ApJ, 155, L71

Kennicutt Robert C. J., Lee J. C., Funes J. G., J. S., Sakai S., Akiyama S., 2008, ApJS, 178, 247

Kilpatrick C. D., Fong W., Prochaska J. X., Tejos N., Bhandari S., Day C. K., 2021, The Astronomer's Telegram, 14516, 1

Kirsten F., Jenkins M., Snelders M., Nimmo K., Hessels J., Gawronski M., Yang J., 2020, The Astronomer's Telegram, 13735, 1

Kirsten F., Snelders M. P., Jenkins M., Nimmo K., van den Eijnden J., Hessels J. W. T., Gawroński M. P., Yang J., 2021, Nature Astronomy, 5, 414

Kirsten F., et al., 2022a, Nature, 602, 585

Kirsten F., et al., 2022b, The Astronomer's Telegram, 15727, 1

Kirsten F., et al., 2024, Nature Astronomy, 8, 337

Komatsu E., et al., 2011, ApJS, 192, 18

Kovlakas K., Zezas A., Andrews J. J., Basu-Zych A., Fragos T., Hornschemeier A., Lehmer B., Ptak A., 2020, MNRAS, 498, 4790

Kozlova A. V., et al., 2016, MNRAS, 460, 2008

Kramer M., Liu K., Desvignes G., Karuppusamy R., Stappers B. W., 2024, Nature Astronomy, 8, 230

Kremer K., Piro A. L., Li D., 2021, ApJ, 917, L11

Kremer K., Li D., Lu W., Piro A. L., Zhang B., 2023, ApJ, 944, 6

Kumar P., Bošnjak Ž., 2020, MNRAS, 494, 2385

Kumar P., Lu W., Bhattacharya M., 2017, MNRAS, 468, 2726

Kumar P., et al., 2021, MNRAS, 500, 2525

Kumar A., Maan Y., Bhusare Y., 2024a, arXiv e-prints, p. arXiv:2406.12804

Kumar P., Qu Y., Zhang B., 2024b, ApJ, 974, 160

Kuzmin A. D., 2007, Ap&SS, 308, 563

Lanman A. E., et al., 2022, ApJ, 927, 59

Law C. J., et al., 2017, ApJ, 850, 76

Law C. J., Connor L., Aggarwal K., 2022, ApJ, 927, 55

Lazaridis K., Jessner A., Kramer M., Stappers B. W., Lyne A. G., Jordan C. A., Serylak M., Zensus J. A., 2008, MNRAS, 390, 839

Lemos T., Gonçalves R. S., Carvalho J. C., Alcaniz J. S., 2023, European Physical Journal C, 83, 138

Levin Y., Beloborodov A. M., Bransgrove A., 2020, ApJ, 895, L30

Li Y., Zhang B., Nagamine K., Shi J., 2019, ApJ, 884, L26

Li C. K., et al., 2021a, Nature Astronomy, 5, 378

Li D., et al., 2021b, Nature, 598, 267

Li Q.-C., Yang Y.-P., Wang F. Y., Xu K., Shao Y., Liu Z.-N., Dai Z.-G., 2021c, ApJ, 918, L5

Li J., Gao Y., Li D., Wu K., 2024, arXiv e-prints, p. arXiv:2404.16669

Licquia T. C., Newman J. A., 2015, ApJ, 806, 96

Lien A. Y., et al., 2014, GRB Coordinates Network, 16522, 1

Lin H.-N., Tang L., Zou R., 2023, MNRAS, 520, 1324

Linscott I. R., Erkes J. W., 1980, ApJ, 236, L109

Liu J.-F., Bregman J. N., Bai Y., Justham S., Crowther P., 2013, Nature, 503, 500

Locatelli N. T., et al., 2020, MNRAS, 494, 1229

Lorimer D. R., 2011, SIGPROC: Pulsar Signal Processing Programs, Astrophysics Source Code Library, record ascl:1107.016

Lorimer D. R., Kramer M., 2004, Handbook of Pulsar Astronomy. Vol. 4

Lorimer D. R., Bailes M., McLaughlin M. A., Narkevic D. J., Crawford F., 2007, Science, 318, 777

Lower M. E., Shannon R. M., Kumar P., 2022, The Astronomer's Telegram, 15172, 1

Lu W., Kumar P., 2018, MNRAS, 477, 2470

Lu W., Beniamini P., Kumar P., 2022, MNRAS, 510, 1867

Luo R., Men Y., Lee K., Wang W., Lorimer D. R., Zhang B., 2020, MNRAS, 494, 665

Luo J.-W., Zhu-Ge J.-M., Zhang B., 2023, MNRAS, 518, 1629

Lyubarsky Y., 2014, MNRAS, 442, L9

Lyubarsky Y., 2020, ApJ, 897, 1

Lyubarsky Y., 2021, Universe, 7, 56

Lyutikov M., 2002, ApJ, 580, L65

Lyutikov M., Burzawa L., Popov S. B., 2016, MNRAS, 462, 941

Lyutikov M., Barkov M. V., Giannios D., 2020, ApJ, 893, L39

Maan Y., Leeuwen J. v., Straal S., Pastor-Marazuela I., 2022, The Astronomer's Telegram, 15697, 1

Macquart J. P., Ekers R., 2018a, MNRAS, 480, 4211

Macquart J. P., Ekers R., 2018b, MNRAS, 480, 4211

Macquart J.-P., Koay J. Y., 2013, ApJ, 776, 125

Macquart J. P., et al., 2020a, Nature, 581, 391

Macquart J. P., et al., 2020b, Nature, 581, 391

Majid W. A., et al., 2021, ApJ, 919, L6

Manchester R. N., Hobbs G. B., Teoh A., Hobbs M., 2005, AJ, 129, 1993

Mannings A. G., et al., 2021, ApJ, 917, 75

Marani G. F., Nemiroff R. S., 1996, in Trimble V., Reisenegger A., eds, Astronomical Society of the Pacific Conference Series Vol. 88, Clusters, Lensing, and the Future of the Universe. p. 107

Marcote B., et al., 2017, ApJ, 834, L8

Marcote B., et al., 2020, Nature, 577, 190

Marcote B., Kirsten F., Hessels J., Nimmo K., Paragi Z., Project P., 2022, in European VLBI Network Mini-Symposium and Users' Meeting 2021. p. 35 (arXiv:2202.11644), doi:10.22323/1.399.0035

Margalit B., Metzger B. D., 2018, ApJ, 868, L4

Margalit B., Berger E., Metzger B. D., 2019, ApJ, 886, 110

Margalit B., Metzger B. D., Sironi L., 2020a, MNRAS, 494, 4627

Margalit B., Beniamini P., Sridhar N., Metzger B. D., 2020b, ApJ, 899, L27

Marthi V. R., et al., 2022, MNRAS, 509, 2209

Masui K., et al., 2015, Nature, 528, 523

McConnachie A. W., Irwin M. J., Ferguson A. M. N., Ibata R. A., Lewis G. F., Tanvir N., 2005, MNRAS, 356, 979

McCulloch P. M., Ellis G. R. A., Gowland G. A., Roberts J. A., 1981, ApJ, 245, L99

McKinven R., Chime/Frb Collaboration 2022, The Astronomer's Telegram, 15679, 1

McLaughlin M. A., et al., 2006, Nature, 439, 817

McMullin J. P., Waters B., Schiebel D., Young W., Golap K., 2007, in Shaw R. A., Hill F., Bell D. J., eds, Astronomical Society of the Pacific Conference Series Vol. 376, Astronomical Data Analysis Software and Systems XVI. p. 127

Mereghetti S., et al., 2020, ApJ, 898, L29

Metzger B. D., Berger E., Margalit B., 2017, ApJ, 841, 14

Metzger B. D., Margalit B., Sironi L., 2019, MNRAS, 485, 4091

Michilli D., et al., 2018, Nature, 553, 182

Michilli D., et al., 2021, ApJ, 910, 147

Newman J. A., Ferrarese L., Stetson P. B., Maoz E., Zepf S. E., Davis M., Freedman W. L., Madore B. F., 2001, ApJ, 553, 562

Nicholl M., Williams P. K. G., Berger E., Villar V. A., Alexander K. D., Eftekhari T., Metzger B. D., 2017, ApJ, 843, 84

Niino Y., 2020, arXiv e-prints, p. arXiv:2005.12891

Nimmo K., et al., 2022a, arXiv e-prints, p. arXiv:2206.03759

Nimmo K., et al., 2022b, Nature Astronomy, 6, 393

Nimmo K., et al., 2022c, ApJ, 927, L3

Niu C. H., et al., 2022, Nature, 606, 873

Olausen S. A., Kaspi V. M., 2014, ApJS, 212, 6

Ould-Boukattine O. S., et al., 2024, The Astronomer's Telegram, 16565, 1

Padovani P., et al., 2017, A&A Rev., 25, 2

Pagano L., Delouis J. M., Mottet S., Puget J. L., Vibert L., 2020, A&A, 635, A99

Pastor-Marazuela I., et al., 2021, Nature, 596, 505

Pastor-Marazuela I., et al., 2023, A&A, 678, A149

Pearlman A. B., Chime/Frb Collaboration 2022, The Astronomer's Telegram, 15792, 1

Pearlman A. B., et al., 2023, arXiv e-prints, p. arXiv:2308.10930

Pelliciari D., et al., 2022, The Astronomer's Telegram, 15696, 1

Pelliciari D., Contarini S., Marulli F., Moscardini L., Giocoli C., Lesci G. F., Dolag K., 2023a, MNRAS, 522, 152

Pelliciari D., et al., 2023b, A&A, 674, A223

Pelliciari D., et al., 2024a, A&A, 690, A219

Pelliciari D., Geminardi A., Bernardi G., Pilia M., Esposito P., Naldi G., 2024b, The Astronomer's Telegram, 16434, 1

Pelliciari D., Geminardi A., Bernardi G., Pilia M., Esposito P., Naldi G., 2024c, The Astronomer's Telegram, 16547, 1

Pen U.-L., Connor L., 2015, ApJ, 807, 179

Penzias A. A., Wilson R. W., 1965, ApJ, 142, 419

Perini F., 2009, in Wide Field Astronomy & Technology for the Square Kilometre Array. p. 61, doi:10.22323/1.132.0061

Perley R. A., Butler B. J., 2013, ApJS, 204, 19

Perley R. A., Butler B. J., 2017, ApJS, 230, 7

Petroff E., et al., 2015, MNRAS, 451, 3933

Petroff E., Hessels J. W. T., Lorimer D. R., 2019, A&A Rev., 27, 4

Petroff E., Hessels J. W. T., Lorimer D. R., 2022, A&A Rev., 30, 2

Petrov L., Kovalev Y. Y., Fomalont E. B., Gordon D., 2011, AJ, 142, 35

Phinney S., Taylor J. H., 1979, Nature, 277, 117

Pilia M., 2021, Universe, 8, 9

Pilia M., et al., 2020, ApJ, 896, L40

Pintore F., et al., 2020, ApJ, 890, 166

Piro A. L., Gaensler B. M., 2018, ApJ, 861, 150

Piro L., et al., 2021, A&A, 656, L15

Planck Collaboration et al., 2016, A&A, 594, A13

Platts E., Weltman A., Walters A., Tendulkar S. P., Gordin J. E. B., Kandhai S., 2019, Phys. Rep., 821, 1

Plavin A., Paragi Z., Marcote B., Keimpema A., Hessels J. W. T., Nimmo K., Vedantham H. K., Spitler L. G., 2022, MNRAS, 511, 6033

Pleunis Z., et al., 2021a, ApJ, 911, L3

Pleunis Z., et al., 2021b, ApJ, 923, 1

Price D. C., Flynn C., Deller A., 2021, PASA, 38, e038

Prochaska J. X., et al., 2019, Science, 366, 231

Ptak A., Griffiths R., 1999, ApJ, 517, L85

Qiu H., et al., 2020, MNRAS, 497, 1382

Qu Y., Zhang B., 2023, MNRAS, 522, 2448

Rahmani S., Lianou S., Barmby P., 2016, MNRAS, 456, 4128

Rajwade K. M., van Leeuwen J., 2024, Universe, 10, 158

Rajwade K. M., et al., 2020, MNRAS, 495, 3551

Ran J.-Y., Wang B., Wei J.-J., 2024, Chinese Physics Letters, 41, 059501

Rana V., et al., 2015, ApJ, 799, 121

Ransom S. M., Eikenberry S. S., Middleditch J., 2002, AJ, 124, 1788

Ravi V., 2019, Nature Astronomy, 3, 928

Ravi V., et al., 2019, Nature, 572, 352

Ravi V., et al., 2023, ApJ, 949, L3

Rea N., Esposito P., 2011, in High-Energy Emission from Pulsars and their Systems. p. 247 (arXiv:1101.4472), doi:10.1007/978-3-642-17251-9 21

Rees M. J., 1977, Nature, 266, 333

Resmi L., Vink J., Ishwara-Chandra C. H., 2021, A&A, 655, A102

Rhodes L., Caleb M., Stappers B. W., Andersson A., Bezuidenhout M. C., Driessen L. N., Heywood I., 2023, MNRAS, 525, 3626

Ridnaia A., et al., 2020, GRB Coordinates Network, 27554, 1

Roberts T. P., Colbert E. J. M., 2003, MNRAS, 341, L49

Rodrigues L. F. S., Chamandy L., Shukurov A., Baugh C. M., Taylor A. R., 2019, MNRAS, 483, 2424

Rogers A. E. E., Moffet A. T., Backer D. C., Moran J. M., 1984, Radio Science, 19, 1552

Rybicki G. B., Lightman A. P., 1979, Radiative processes in astrophysics

Ryder S. D., et al., 2023, Science, 382, 294

Sand K. R., et al., 2023, arXiv e-prints, p. arXiv:2307.05839

Scheuer P. A. G., 1968, Nature, 218, 920

Schwab J., Quataert E., Kasen D., 2016, MNRAS, 463, 3461

Shannon R. M., et al., 2024, arXiv e-prints, p. arXiv:2408.02083

Shappee B. J., Stanek K. Z., 2011, ApJ, 733, 124

Sharma K., et al., 2023, ApJ, 950, 175

Sharma K., et al., 2024, arXiv e-prints, p. arXiv:2409.16964

Sheikh S. Z., et al., 2023, arXiv e-prints, p. arXiv:2312.07756

Shin K., CHIME/FRB Collaboration 2024, The Astronomer's Telegram, 16420, 1

Shin K., et al., 2023, ApJ, 944, 105

Shull J. M., Smith B. D., Danforth C. W., 2012, ApJ, 759, 23

Smirnov O. M., 2011, A&A, 527, A107

Snelders M. P., et al., 2023, Nature Astronomy, 7, 1486

Spitler L. G., et al., 2014, ApJ, 790, 101

Spitler L. G., et al., 2016, Nature, 531, 202

Spitler L. G., et al., 2018, ApJ, 863, 150

Springel V., 2010, MNRAS, 401, 791

Sridhar N., Metzger B. D., Beniamini P., Margalit B., Renzo M., Sironi L., Kovlakas K., 2021, ApJ, 917, 13

Sridhar N., Metzger B. D., Fang K., 2024, ApJ, 960, 74

Staelin D. H., Reifenstein Edward C. I., 1968, Science, 162, 1481

Stamatikos M., Malesani D., Page K. L., Sakamoto T., 2014, GRB Coordinates Network, 16520,

Stetson P. B., et al., 1998, ApJ, 508, 491

Suresh A., Chatterjee S., Cordes J. M., Crawford F., 2021, ApJ, 920, 16

Tauris T. M., Sanyal D., Yoon S. C., Langer N., 2013, A&A, 558, A39

Tavani M., et al., 2009, A&A, 502, 995

Tavani M., et al., 2020, ApJ, 893, L42

Tavani M., et al., 2021, Nature Astronomy, 5, 401

Taylor J. H., Backus P. R., Damashek M., 1981, ApJ, 244, L65

Tendulkar S. P., et al., 2017, ApJ, 834, L7

Tendulkar S. P., et al., 2021, ApJ, 908, L12

Thompson C., Duncan R. C., 1995, MNRAS, 275, 255

Thompson A. R., Moran J. M., Swenson George W. J., 2017a, Interferometry and Synthesis in Radio Astronomy, 3rd Edition, doi:10.1007/978-3-319-44431-4.

Thompson A. R., Moran J. M., Swenson Jr. G. W., 2017b, Interferometry and Synthesis in Radio Astronomy, 3rd Edition, doi:10.1007/978-3-319-44431-4.

Thornton D., et al., 2013, Science, 341, 53

Tingay S. J., Kaplan D. L., 2016, ApJ, 820, L31

Trudu M., et al., 2022, MNRAS, 513, 1858

Trudu M., et al., 2023, A&A, 676, A17

Tuccari G., 2003, in Minh Y. C., ed., Astronomical Society of the Pacific Conference Series Vol. 306, New technologies in VLBI. p. 177

Turolla R., Zane S., Watts A. L., 2015, Reports on Progress in Physics, 78, 116901

Ursi A., et al., 2022a, ApJ, 924, 80

Ursi A., et al., 2022b, ApJ, 924, 80

Uttarkar P. A., Kumar P., Lower M. E., Shannon R. M., 2024, The Astronomer's Telegram, 16430, 1

Vanderlinde K., et al., 2019, in Canadian Long Range Plan for Astronomy and Astrophysics White Papers. p. 28 (arXiv:1911.01777), doi:10.5281/zenodo.3765414

Vazza F., Brüggen M., Hinz P. M., Wittor D., Locatelli N., Gheller C., 2018, MNRAS, 480, 3907

Vohl D., Vedantham H. K., Hessels J. W. T., Bassa C. G., Cook D. O., Kaplan D. L., Shimwell T. W., Zhang C., 2023, A&A, 680, A98

Walters A., Weltman A., Gaensler B. M., Ma Y.-Z., Witzemann A., 2018, ApJ, 856, 65

Wang B., Liu D., 2020, Research in Astronomy and Astrophysics, 20, 135

Wang F. Y., Yu H., 2017, J. Cosmology Astropart. Phys., 2017, 023

Wang F. Y., Wang Y. Y., Yang Y.-P., Yu Y. W., Zuo Z. Y., Dai Z. G., 2020, ApJ, 891, 72

Waxman E., 2017, ApJ, 842, 34

Webster M., Bridle S. L., Hobson M. P., Lasenby A. N., Lahav O., Rocha G., 1998, arXiv e-prints, pp astro-ph/9802109

Wei J.-J., Gao H., Wu X.-F., Mészáros P., 2015, Phys. Rev. Lett., 115, 261101

Whitney A., Kettenis M., Phillips C., Sekido M., 2010, in Navarro R., Rogstad S., Goodhart C. E., Sigman E., Soriano M., Wang D., White L. A., Jacobs C. S., eds, Sixth International VLBI Service for Geodesy and Astronomy. Proceedings from the 2010 General Meeting. pp 192–196

Xiao D., Dai Z.-G., Wu X.-F., 2024, ApJ, 962, 35

Xing N., Gao H., Wei J.-J., Li Z., Wang W., Zhang B., Wu X.-F., Mészáros P., 2019, ApJ, 882, L13

Xu J., Han J. L., 2015, Research in Astronomy and Astrophysics, 15, 1629

Xu H., et al., 2022, Nature, 609, 685

Xu J., et al., 2023, Universe, 9, 330

Yamasaki S., Totani T., 2020, ApJ, 888, 105

Yang Y.-P., 2023, ApJ, 956, 67

Yang Y.-P., Zhang B., 2018, ApJ, 868, 31

Yang Y.-P., Xu S., Zhang B., 2023, MNRAS, 520, 2039

Yao J. M., Manchester R. N., Wang N., 2017, ApJ, 835, 29

Ye C. S., Kremer K., Chatterjee S., Rodriguez C. L., Rasio F. A., 2019, ApJ, 877, 122

Younes G., et al., 2017, ApJ, 847, 85

Zanazzi J. J., Lai D., 2020, ApJ, 892, L15

Zhang S.-N., 2016, arXiv e-prints, p. arXiv:1601.04558

Zhang B., 2022, arXiv e-prints, p. arXiv:2212.03972

Zhang C. F., et al., 2020, The Astronomer's Telegram, 13699, 1

Zhang G. Q., Wang P., Wu Q., Wang F. Y., Li D., Dai Z. G., Zhang B., 2021, ApJ, 920, L23

Zhang Y.-K., et al., 2022, Research in Astronomy and Astrophysics, 22, 124002

Zhang Y.-K., et al., 2023a, arXiv e-prints, p. arXiv:2304.14665

Zhang J.-G., Zhao Z.-W., Li Y., Zhang J.-F., Li D., Zhang X., 2023b, Science China Physics, Mechanics, and Astronomy, 66, 120412

Zhang X., et al., 2023c, ApJ, 959, 89

Zhang J., et al., 2024, The Astronomer's Telegram, 16505, 1

Zhong S.-Q., Dai Z.-G., 2020, ApJ, 893, 9

Zhou B., Li X., Wang T., Fan Y.-Z., Wei D.-M., 2014, Phys. Rev. D, 89, 107303

Zhou D. J., et al., 2022, Research in Astronomy and Astrophysics, 22, 124001

Zhu W., et al., 2023, Science Advances, 9, eadf6198

de Graaff A., Cai Y.-C., Heymans C., Peacock J. A., 2019, A&A, 624, A48